Doctoral Dissertation

Study on Charge Transfer Dynamics of a Photocatalyst Material by Time-resolved Terahertz Spectroscopy

時間分解テラヘルツ分光法を用いた光触媒物質の
電荷輸送ダイナミクスの研究

Nguyen Ngoc Phuong

December 2018

Department of Physics, Graduate School of Science
Osaka University

Abstract

Human beings are facing the depletion of energy sources and the high concentration of CO_2 in the atmosphere. Photocatalysis based on artificial photosynthesis is a solution to those problems. Among various types of the photocatalyst, rhenium carbonyl diimine complexes are the promising candidates for reduction of CO_2 with high quantum yield and benefit in storing energy as chemical energy which is easier in storing and transferring than electronic current (solar cells). Moreover, these Re complexes play both roles of a photosensitizer and a catalyst and completely absent formation of product(s) as hydrogen and acid formic.

In the photocatalytic reaction, the intermolecular interaction between solvent and solute molecules appeared in THz region plays a crucial role. Therefore, to understand their interaction on the excited state and during the electron transfer process on Re complexes, we investigated the relaxation dynamics as well as the electron transfer process of a photocatalytic $[Re(CO)_2(bpy)\{P(OEt)_3\}_2](PF_6)$ (Re complex) in 2,2',2'' Nitrilotriethanol (TEOA) solvent as an electron donor by the excitation of 400-nm pulses using time-resolved attenuated total reflection terahertz spectroscopy (TR-ATR).

To determine the origin of the vibrational modes of Re complex in TEOA solvent, we used the combination of THz time-domain spectroscopy (THz-TDS) and THz time-domain attenuated total reflection spectroscopy (THz-ATR) to measure the absorption spectra of Re complex in powder form and in the solution. The absorption spectrum of Re complex in TEOA solvent shows three peaks at 1, 1.35, and 1.75 THz, meanwhile that of in the solid form shows four peaks at 0.5, 1, 1.7, and 2.2 THz. By comparing two absorption spectra, we assign the 1-THz peak as the intramolecular vibrational mode of bpy ligand, the 1.35-THz peak as intermolecular vibrational mode between the cation $[Re(CO)_2(bpy)\{P(OEt)_3\}_2]^+$ and TEOA molecules. The 0.5-, 1.7-, and 2.2-THz peaks can be assigned the intermolecular vibrations between cation $[Re(CO)_2(bpy)\{P(OEt)_3\}_2]^+$ and anion $(PF_6)^-$.

The observed temporal structure by TR-ATR shows the spectral change in position, intensity and shape. These spectral changes suggest that the dynamic of the intermolecular vibration, which undergoes three-step transitions in picosecond, as shown in Fig.1.

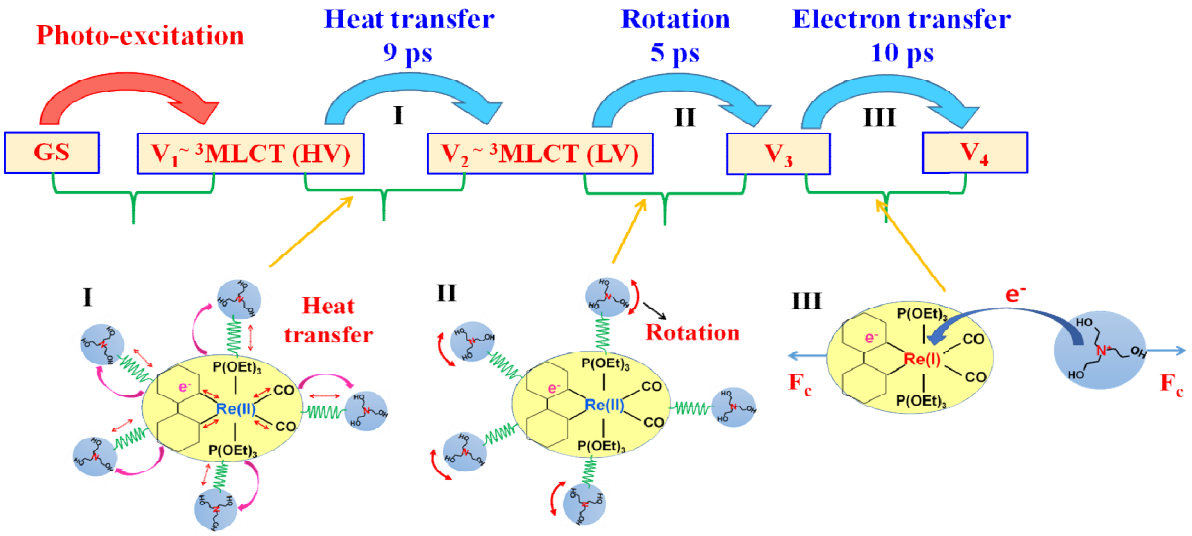

Figure 1: Schematic diagram and molecular forms after photexcitation. The top diagram shows the three-step dynamic from the highest excited state V_1 through the lowest excited state V_4 of $[Re(CO)_2(bpy)\{P(OEt)_3\}_2](PF_6)$ in TEOA solvent in the range of 0.3-2.5 THz. The bottom diagram illustrates the interaction between Re complex and TEOA molecules corresponding to each dynamical step I-III.

The spectrum changes after photoexcitation, which is shifted to the lower frequency side in 1 ps and returns slowly back to the initial position in 9 ps. Firstly, the gradually relax to the initial position of the 1-THz and 1.35-THz peaks in 9 ps is the vibrational cooling of the triplet metal-to-ligand charge transfer (^{3}MLCT) excite state. Secondly, the sudden shift of the 1.35-THz peak to 1.7 THz indicates the distance between Re and TEOA is reduced by the rotation of TEOA molecules due to dipole-dipole interaction accelerated by heat transfer. Finally, the steeply reduction of all peak areas after 14 ps is explained by the electron transfer from TEOA donor to Re atom. Figure 1(b) illustrates the response of TEOA molecules related to each transitional step.

Observing the dynamic of the intermolecular vibrational modes help to have a deep insight into the interaction between the catalysts and the solvent molecules in photocatalysts phenomena.

Table of Contents

List of Abbreviation

bpy: 2,2'- bipyridine ($C_{10}H_8N_2$)

ET: electron transfer

ES: excited state

IL: intraligand

ISC: intersystem crossing

^{1}MLCT: singlet metal-to-legand charge transfer excited state

^{3}MLCT: triplet metal-to-legand charge transfer excited state

S/N: signal/noise

TEOA: triethanolamine

THF: tetrahydrofuran

DMF: N, N-dimethylformamide

THz: Terahertz

THz-ATR: THz time domain attenuated total reflection spectroscopy

THz-TDS: Terahertz time domain spectroscopy

TRTS: Time-resolved Terahertz spectroscopy

TR-ATR: Time-resolved Attenuated total reflection spectroscopy

Chapter I

Introduction

1.1 Introduction to rhenium tricarbonyl diimine complexes

The development of heavy industry has been causing human being facing with energy crisis - depletion of fossil fuel such as coal, gas, and oil, and greenhouse effect[1,2] caused by high concentration CO_2. The idea of converting CO_2 gas from the atmosphere to the renewable energy source is the possible solution for such mentioned problems. Hence, the utilization of photocatalysts[3-10] for reducing CO_2 to energy-rich carbon compounds using solar radiation as an energy source has been attracted a lot of attention.

The process of converting CO_2 efficiently to a useful compound using solar light and water (a reductant) is observed in natural plant life, in which CO_2 transformation is performed via the photosynthetic system. By simulating such a natural system, a novel photocatalytic system developed as an artificial photosynthesis is likely the optimal solution[11,12] for resolving the energy crisis and greenhouse effect. Figure 1.1 shows the nature and the artificial photosynthetic processes for converting harmful substance to the useful compounds by solar light. The word photocatalyst is combined with two parts “photo” and “catalyst”. The catalyst is a substance which accelerates the rate of reaction by decreasing the activation energy. Generally speaking, the photocatalyst is a substance, which activates the chemical reaction using light irradiation.

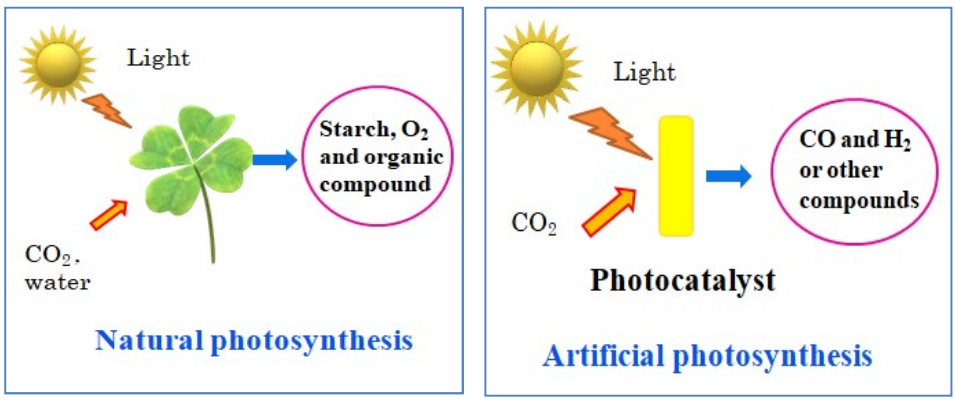

Figure 1.1: Natural and artificial photosynthesis.

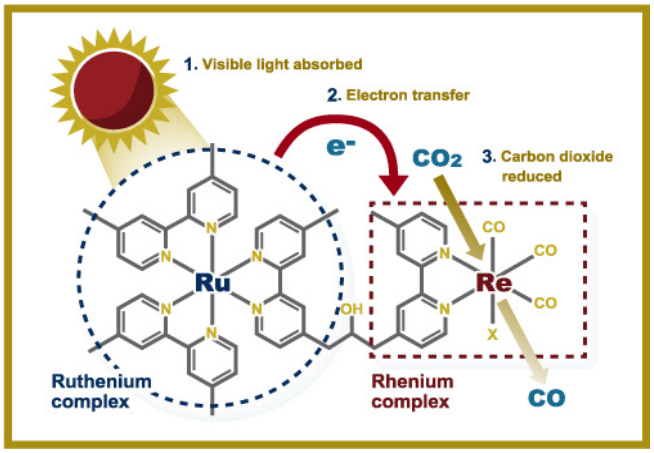

Figure 1.2: An artificial photosynthesis[13] (Rhenium-ruthenium photocatalyst).

The first development of TiO_2 photocatalysts for the artificial photosynthesis was reported by the pioneering works of Fujishima and Honda in 1970. Following that, photocatalysts have been explored by various means, including utilizing metal electrodes, electrocatalytic semiconductors such as TiO_2, ZnS, CdS,…[14,15], and organometallic complexes of Co, Ni, Mn, and Fe (porphyrin complexes)[16,17]. These classically require a high applied current, which is not easy to handle. In 1983, Lehn and his coworkers reported the very selective reduction of CO_2 to CO using $[Re(L)(CO)_3(N,N)]$ as a photocatalyst.

Among these photocatalysts for CO_2 reduction, Re(I) tricarbonyl complexes have been noticed as the most superior in efficiency in CO_2 reduction[18-27] and selection of formed products. Figure 1.2 shows the reduction of CO_2 to CO of rhenium-ruthenium photocatalyst by absorbing visible lights. Ru complex plays the role of a photosensitizer that absorbs visible light to create excited electrons, while Re complex is a catalyst that receives one electron from a Ru complex to start the photocatalytic cycle. According to comparing photosynthetic and photovoltaic efficiencies by Robert E. Blankenship et. al.[28], generating energy with photosynthetic process brings advantages in energy storage and transportation in comparison with photovoltaic cells. In fact, the photosynthetic process creates chemical energy that is stored in the chemical bonds of its molecular products. The energy can be used immediately or withdraw later when needed. Unlike photosynthesis, harvested solar energy from photovoltaic cells is turned directly into electrical currents. If the current is not used right away, it will discharge and disappear, the only way to store electricity is with an external device, such as batteries.

In the photocatalytic reaction, Re complexes[29] play both roles of the photosensitizer and catalyst. In addition, the formed products are completely absent from hydrogen and

formic acid. Ru complex can be either the photosensitizer or catalyst. For example, Ru complexes itself acts as the photosensitizer and needs to be incorporated with another complex as the catalyst. Thus, Re complexes are getting more attraction than Ru complexes. They can also be incorporated with other complexes to form supramolecular systems[29,30], which are showing the remarkably efficient CO_2 reduction by visible light.

Sum of all reasons mentioned above, photocatalysts based on Re(I) are the promising candidates for CO_2 reduction to produce of CO selectively with high quantum yields.

Figure 1.3 shows the overall photocatalytic processes roughly including five main steps, in which the Re complex absorbs photons to generate the excited state in the first step and proceeds the rest steps such as the relaxation of excited electrons, the electron transfer process, the multi-electron transfer, the photo-substitution of a ligand by CO_2 molecule, and the reduction of CO_2 to CO. The relaxation of excited electrons and the electron transfer process are crucial steps in the photocatalytic process because these steps trigger chemical reactions of the catalyst. Therefore, in the interest of these steps, the relaxation of excited electrons generated by photoexcitation and electron transfer process are studied.

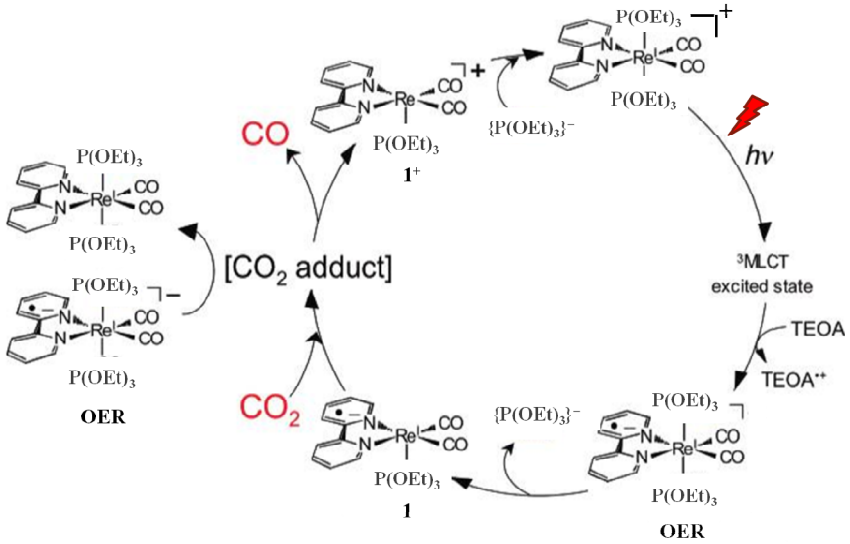

Figure 1.3: Schematic diagram of reduction of CO_2 process by photocatalyst $[Re(CO)_2(bpy)\{P(OEt)_3\}_2]$

To utilize photocatalysts is necessary to understand the photophysical and photochemical processes of these complexes. Photophysical properties of these complexes play a crucial role in the photocatalytic process because it supplies important information that occurs after the catalyst absorbs photon energy such as excited state structure of these

complexes, structural changes, vibrational energy distribution, and electron or energy transfer reaction, and so on.

Photophysical properties of rhenium complexes have been deeply studied by the support of various spectroscopies from the X-ray to mid-infrared regions[32–34]. Indeed, the lowest absorption bands of $[Re(L)(CO)_3(N,N)]^n$ are generated by the excitation in the near-UV region. These absorptions majorly correspond to singlet metal-to-ligand charge transfer ^{1}(MLCT) excited state and have been studied some depth. Photoexcitation of 400 nm wavelength populates the lowest singlet excited state of $[Re(L)(CO)_3(N,N)]^n$ in the femtosecond timescale. Relaxation processes of these complexes persists into the picosecond time scale. The ^{1}MLCT undergoing intersystem crossing generates hot triplet states and relaxes into the thermally equilibrated lowest ^{3}MLCT excited state (^{3}MLCT(LV)) in a few picoseconds. Following that, phosphorescent emitted with the time scale from the picosecond to nanosecond and has been well-interpreted[32]. The overall relaxation of Re complexes is shown in Fig. 1.4.

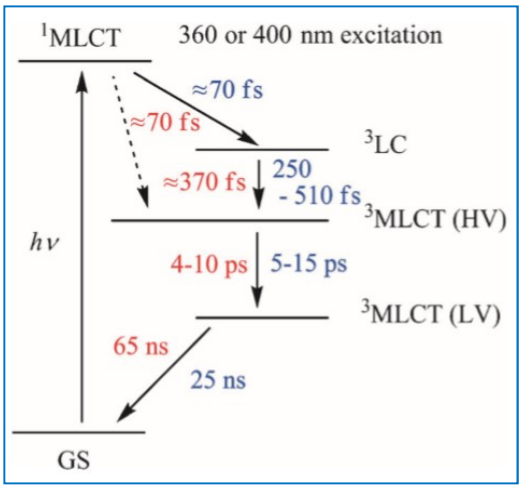

Figure 1.4: Photophysical processes[34] of fac-$[Re(bpy)(CO)_3Cl]$ following excitation at ≥360 nm in tetrahydrofuran (THF) (lifetimes in red) and acetonenitrile (MeCN) (lifetimes in blue).

Those reported studies principally relate to probing the dynamic processes of high-frequency intramolecular vibrations on the complex. The photophysical process of fac-$[Re(bpy)(CO)_3Cl]$ following excitation at ≥360 nm in THF (lifetimes in red) and MeCN (lifetimes in blue) is shown in Fig. 1.4. The detail of previous studies of Re complex by luminescence and UV/vis absorption spectroscopy will be presented next chapter. Here, we will discuss the υ(CO) stretching modes studied by time-resolved THz spectroscopy (TRIR).

Figure 1.4 shows the relaxation- vibrational cooling of the ^{3}MLCT band with the lifetime of 4-10 ps determined by CO stretching modes in the mid-IR region.

After photoexcitation, one electron on the valence band of Re atom transfers to the excited state of bpy ligand, this transfer weakens the π bonding of (Re-CO) and strengthen σ bonding of (Re-CO). These changes have been probed by intramolecular vibrations in high-frequency (υ(CO) and υ(bpy)). Stretching modes υ(CO) are sensitive to the electronic density of Re complexes. Thus, it is not only used to probe electronic structure change on Re complexes but also observe the response of solvent molecules upon the excited state. However, the response of the neighboring solvent molecules would be better understood if an intermolecular interaction is probed. It is worth to investigate the factors, which affect photochemical and photophysical properties of the photocatalysts by the intermolecular interaction. Moreover, the intermolecular interaction is crucial to clarify the electron transfer process.

The electron transfer (ET) process from electron donors to the catalyst is the important primary step in photocatalysis because it initiates the reduction of CO_2. Depending on complexes and the medium (solvent and concentration of electron donor), ET can occur from milliseconds to picoseconds timescales. To obtain the electron transfer, from ^{3}MLCT(LV), phosphorescence can be quenched by the presence of effectively sacrificial electron donor such as triethanolamine (TEOA) or triethylamine (TEA).

It is noticeable that the lifetime of ^{3}MLCT(HV) in a few ten picoseconds[33,34] and the intermolecular vibrations lying in the THz region, thus THz spectroscopy is suggested to investigate the intermolecular dynamic of Re complexes in low frequency.

1.2 Introduction to THz spectroscopy

With the emerging of THz technology, THz spectroscopy allows us to observe low-frequency intramolecular and intermolecular vibrations because the frequency of these vibrations lies in the THz region. Intense and broadband THz radiation now can be generated and detected with the support of Ti-sapphire lasers. Time-resolved spectroscopy is a powerful tool supporting us to study the response of materials following the photo-excitation. Especially, time-resolved attenuated total reflection spectroscopy (TR-ATR) is a suitable technique that allows us to map out excited state dynamics of the sample solution with high absorption in the THz region. TR-ATR and THz-ATR are meaningful in studies of molecular interactions in high absorbing THz medium because these interactions usually occur in the

THz region. Besides TR-ATR, THz time-domain spectroscopy (THz-TDS) plays a crucial role in proving the information about the ground state structure of materials in the solid form. All detail of TR-ATR, THz-TDS and THz-ATR will be discussed in the next chapter.

1.3 Purpose and Motivation

The ET process is one of the most crucial steps in the photocatalytic activity. During ET process, the intermolecular interaction of catalyst- electron donor molecules manifested by intermolecular vibration is anticipated to provide critical information such as the relative position between catalyst- electron donor molecules. Thus, the attempt of understanding the ET process between solute and solvent molecules, we investigate the intermolecular interaction of catalyst - electron donor molecules upon the excited state generating by the photoexcitation of 400 nm wavelength. The mutual intermolecular interaction of molecules appears in THz region and the relaxation of the excited electrons as well as the ET process on Re complexes in the solvent are also supposed to occur in picoseconds. Therefore, THz spectroscopies such as THz-TDS (transmittance spectroscopy), THz-ATR, and TR-ATR are constructed in the purpose of studying absorption spectra of the photocatalyst materials in solid form, solution and the relaxation of photo-excited electrons as well as the ET process via low-frequency intramolecular vibrational modes and intermolecular vibrations, respectively.

TR-ATR and THz-ATR are used to examine the experiment because of the high absorbing of TEOA solvent that time-resolved THz spectroscopy (TRTS) and THz-TDS cannot be applied. We use TR-ATR to investigate dynamic of intermolecular vibration of TEOA-Re complex molecules. Furthermore, to distinguish and determine the origin of vibrations such as low-frequency intramolecular vibrations or intermolecular vibrations of Re complex in TEOA in the solid form, we adopt the combination of THz-ATR and THz-TDS.

To study the relaxation dynamics of Re(I) tricarbonyl complexes in the THz region, $[Re(CO)_2(bpy)\{P(OEt)_3\}_2](PF_6)$ is chosen to represent for its family ($[Re^I(N,N)(CO)_3(X)]$ (N,N= bpy ligand, X= halogen), since it is one of the most efficient photocatalysts for CO_2 reduction to selectively produce CO, with high quantum yield ($\Phi = \sim 0.38$)[26]. Moreover, this complex is fairly stable in solution at room temperature due to the strong electron-withdraw property of $P(OEt)_3$ ligands. TEOA[35] is well-known as the best sacrificial electron donor, which can boost the turnover number and the selectivity of CO formation. In addition, the ET time scale of pure TEOA solvent in tens of picoseconds[36], which is suitable for our study.

Chapter II

Background

Chapter II is an introduction to many subjects that are discussed in this thesis. Firstly, in order to understand how THz radiation is generated and detected, generation and detection methods for THz radiation are explained. Additionally, the history and introduction of THz time domain spectroscopy (THz-TDS), THz time domain attenuated total reflection spectroscopy (THz-ATR) and time-resolved attenuated total reflection spectroscopy (TR-ATR) are introduced. Secondly, the structure, characterization of $Re(bpy)(CO)_2\{P(OEt)_3\}](PF_6)$ is briefly explained. Finally, to study photophysical process of $Re(bpy)(CO)_2\{P(OEt)_3\}](PF_6)$ complex, the importance of optical excitation and relaxation dynamics of Rhenium complexes is explained.

2.1 Terahertz spectroscopy

2.1.1 Terahertz radiation

THz radiation, which is also called T-rays or T-waves, is electromagnetic waves with frequency from 300 GHz (λ= 1 mm) to 10 THz (λ = 30 μm). THz waves lie in between microwave and infrared regions, and known as THz gap, shown in Fig. 2.1. THz radiation has long wavelengths and low energy; thus it can penetrate a wide variety of non-conducting materials such as clothing, paper, wood, plastic and ceramics,… Thus, THz radiation is expected for many applications such as the security[37] in the airport and detection of the drugs[37].

The energy scale of THz radiation is much lower than electronic state transition of atoms or molecules so THz photons cannot excite electrons to the excited states directly, its frequency corresponds to intermolecular and low-frequency intramolecular vibrational modes. The intermolecular and intramolecular vibrational modes play an important role in many complexes. Therefore, THz radiation supplies important techniques to study vibrational modes of various materials from biology to chemistry. In addition, the THz radiation with the frequency between 0.2 and 3 THz is ideal for probing free carriers in

semiconductors[38] since this frequency range closely matches carrier scattering rates[37-39] of 10^{12} to 10^{14} s^{-1}.

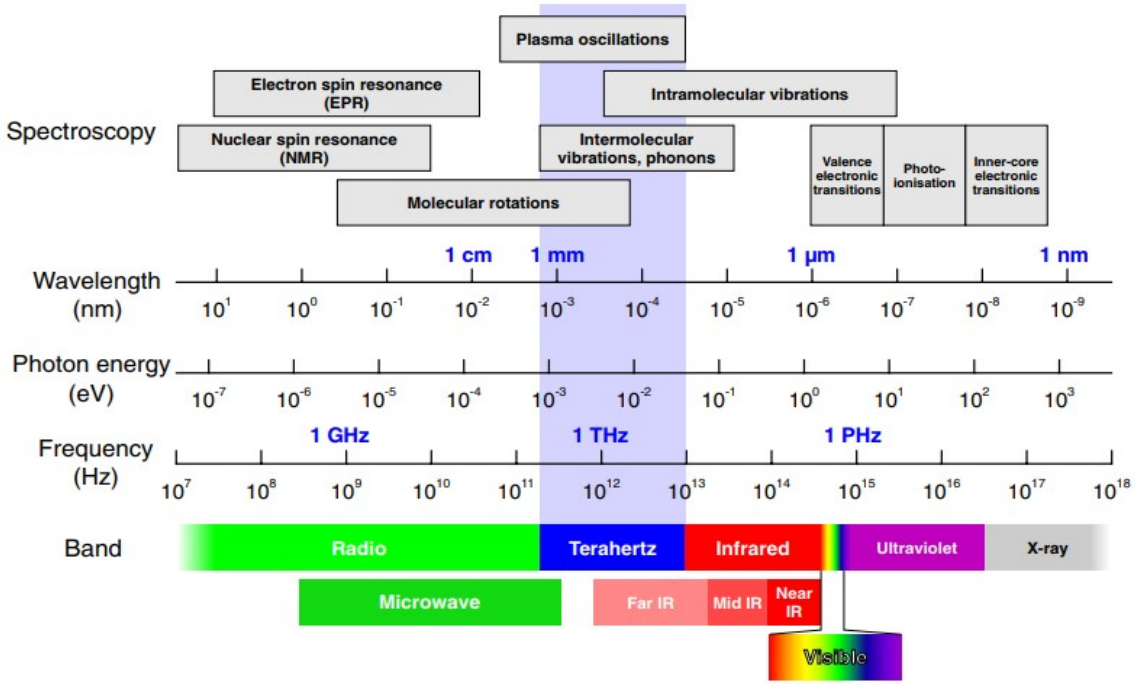

Figure 2.1: Electromagnetic spectrum from radio to x-ray. region[40].

Water and the earth's atmosphere (water vapor) strongly absorb THz radiation, resulting to THz radiation from nature is limited. With remarkable applications of THz technology, a broadband and intense THz sources have been noticed for decades. The THz radiation with the bandwidth achieved a few hundred THz has been generated and detected successfully by laser-based methods. The details of generation and detection freely propagating THz pulse are presented in the next section.

THz radiation provides a great deal of information in medical imaging[41,42] due to its low photon energy and non-ionizing that do not cause damage to tissue and DNA of living species. THz radiation allows safety, non-invasion, and painlessness of effective detection of cancer with an imaging system. It is capable to penetrate dielectrics and many materials have unique spectral "fingerprints" in the THz region. Those advantages give rise the use of THz radiation in security system and safety. With the frequency from 0.1 to 10 THz, not only offer detection threats under clothing, but also the possibility of identifying them from their own spectra[37].

2.1.2 Generation and detection of THz radiation

THz radiation generated and detected by various methods has been reported in detail over a few decades. In the interest of this section, the common techniques to generate THz radiation - optical rectification and detection THz by nonlinear crystal are presented.

2.1.2.1 THz generation by optical rectification in nonlinear crystal

Optical rectification (OR) is widely used to generate broad bandwidth and intense THz pulse, which becomes one of the most efficient approaches. In comparison with photoconductive antennas technique, OR provides a simple and stable method for generating THz by using femtosecond laser pulses because of no need to supply external high voltage power.

OR is a second-order nonlinear optical process with difference frequency close to 0, takes place in non-centrosymmetric media. Generally, OR bases on the development of quasi-DC polarization when intense laser beams propagate through a nonlinear medium (electro-optical (EO) crystals). Femtosecond laser pulses containing many frequency components induce a change in the time-dependence nonlinear polarization in the nonlinear crystal, which gives rise to the emission of electromagnetic waves in the THz region, shown in Fig. 2.2 a).

The electric polarization P induced in the nonlinear medium can be expanded into a power series of the electric field E

$$\begin{aligned}\mathbf{P}(\mathbf{r},t) = {} & \chi^{(1)}(\mathbf{r},t)\,\mathbf{E}(\mathbf{r},t) + \chi^{(2)}(\mathbf{r},t):\mathbf{E}(\mathbf{r},t)\,\mathbf{E}(\mathbf{r},t) \\ & + \chi^{(3)}(\mathbf{r},t):\mathbf{E}(\mathbf{r},t)\,\mathbf{E}(\mathbf{r},t)\,\mathbf{E}(\mathbf{r},t) + \ldots\end{aligned}, \tag{2.1}$$

Here, $\chi^{(n)}$ is the nth-order susceptibility tensor of the material.

THz generation by OR comes from the second order susceptibility of the equation (1.1), given by:

$$\begin{aligned}\mathbf{P}_{\mathrm{OR}}^{(2)}(t) &= 2\chi^{(2)}: \int_0^\infty \int_0^\infty \mathbf{E}(\omega_1)\,\mathbf{E}^*(\omega_2) \exp\left[-i(\omega_1 - \omega_2)\,t\right] \mathrm{d}\omega_1 \mathrm{d}\omega_2 \\ &= 2\chi^{(2)}: \int_0^\infty \int_0^\infty \mathbf{E}(\omega + \Omega)\,\mathbf{E}^*(\omega) \exp\left[-i\Omega t\right] \mathrm{d}\Omega\, \mathrm{d}\omega,\end{aligned} \tag{2.2}$$

The incident light is considered as the plane wave, then electric field E can be expressed as

$$\mathbf{E}(t) = \int_0^{+\infty} E(\omega) \exp(-i\omega t)\, \mathrm{d}\omega + \text{c.c.} \tag{2.3}$$

Where Ω is the frequency difference of two optical frequency components ω_1 and ω_2.

In the far field, the temporal THz field is proportional to the second derivative of $P^{(2)}_{OR}(t)$ with respect to the time t,

$$\mathbf{E}_r(t) \propto \frac{\partial^2}{\partial^2 t} \mathbf{P}^{(2)}_{\mathrm{OR}}(t) \tag{2.4}$$

The susceptibility tensor $\chi^{(2)}$ depends on the structure of the nonlinear crystal. In the ideal theory, the spectral bandwidth of temporal THz radiation is only affected by the frequency components of the excited laser beam. However, many factors, such as material structure, crystal orientation, absorption, diffraction, saturator and phase matching condition influence on the generated efficiency, waveform and frequency distribution. Therefore, in order to generate the intense THz pulse with high efficiency, those mentioned conditions above need to be satisfied. Among those, phase matching condition between the THz phase velocity and the optical group velocity is the most crucial condition for the nonlinear process.

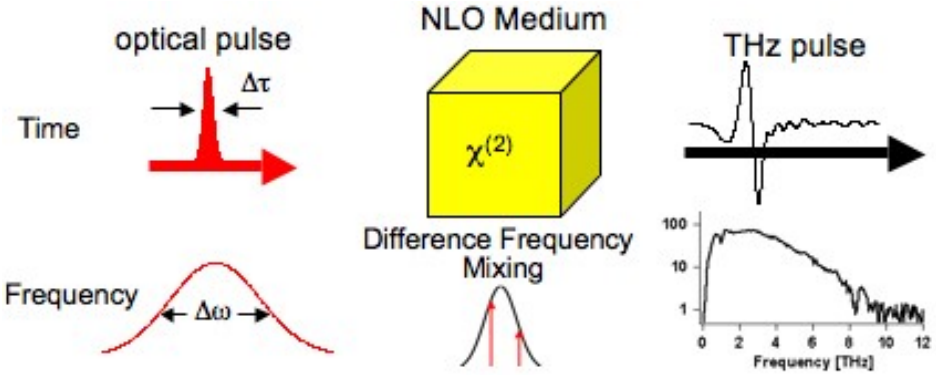

Figure 2.2: Schematic diagram illustrates the THz pulse generated by OR in nonlinear crystals[43].

Phase matching condition requires conservation of momentum and energy in OR process, given by:

$$\begin{aligned} \omega_{01} - \omega_{02} &= \Omega_{\mathrm{THz}} \\ \mathrm{k}_{01} - \mathrm{k}_{02} &= \mathrm{k}_{\mathrm{THz}} \end{aligned} \tag{2.5}$$

Here, ω_{01}, ω_{02} and k_{01}, k_{02} are frequencies and wave vectors of optical pulses involved in THz pulse generation, respectively. Ω_{THz} and k_{THz} are the frequency and the wave vector of generated THz pulse.

When the phase matching condition fulfills, all three waves participating can keep in phase, as the result, the output reaches the maximum efficiency. Phase mismatch leads to a phase walk-off while propagating. The coherent length is defined by the interaction length when the phase change reaches π.

$$\delta k L_C = \pi \tag{2.6}$$

Here, $\delta k = k_{01}-k_{02}-k_{THz}$, L_C is the coherent length.

Based on Eq. (2.6), the nonlinear crystals with long Lc suit for THz generation via OR. In addition, to generate effective THz pulses, the thickness of nonlinear crystals cannot be longer than the coherence length, due to avoiding the phase mismatch.

Now for a more straightforward way, Eq. (2.5) will be written in another form to understand the phase matching condition. We take the division of the first equation in Eq. (2.5) by the second one.

$$\frac{\partial \omega_O}{\partial k_O} = \frac{\Omega_{\mathrm{THz}}}{k_{\mathrm{THz}}} \tag{2.7}$$

Equation (2.7) can be written as (following the electromagnetic principle):

$$v_{G,O} = v_{\mathrm{Ph,Thz}} \tag{2.8}$$

Equation (2.8) means that the phase matching condition is fulfilled when the group velocity of the optical waves is equal to the phase velocity of the THz pulses, the optical beam and the THz beam will collinearly propagate through the nonlinear crystal. This phase matching type can produce high yield of THz radiation with excellent beam quality.

Among many nonlinear crystal, ZnTe crystal is the most popularly used for generating THz by femtosecond laser pulse (especially with Ti:sapphire mode-locked laser with 800 nm central wavelength). ZnTe crystal meets the phase matching condition relatively well between 800 nm, the group velocity of the optical pulses generated by femtosecond lasers is equal to the phase velocity of THz pulses created inside the crystal.

2.1.2.2 THz generation by air plasma

THz radiation generated by OR in a second-order nonlinear crystal shows high performance of THz generation and impressive pulse energy with very good beam quality. However, this technique still has drawback due to damage threshold of nonlinear crystal at

high optical flux, leading to a limit on maximum THz emission. Moreover, the bandwidth of THz emission is also limited by absorption of nonlinear crystal and phase matching requirements. To overcome these limitations, THz emission from photo-induced gas plasmas is a promising alternative way to generate intense THz pulses with broad spectral bandwidth. With this method, laser intensity that has much higher than the damage threshold of nonlinear crystal or photoconductive antennas (PCAs) is able to use without any concern about breaking the THz emitter devices.

This technique was first demonstrated by Hamster et al[44,45], by focusing femtosecond laser pulses with energy greater than the threshold of ionization of gas molecules (~50 mJ) to form the plasma in air. With this technique, there is no damage threshold for such an emitter. The THz generation mechanism in Hamster's experiment was involved to accelerate the ionized electrons created by the ponderomotive force inside the plasma, giving rise a concial THz emission making an angle to the propagation direction.

After Hamster's work, several plasma-based THz generation ways have been reported, which show higher efficiency of THz emission than basing on the mechanism of ponderomotive force, due to THz emission propagates along the direction of the propagation.

In 2000, Cook et al.[46] demonstrated another method to generate higher THz radiation by combining the fundamental (800 nm) and its second harmonic pulses (400 nm) to excite air plasma. The mechanism of this method is explained by four waves mixing (FWM) nonlinear optical process. Four wave mixing process can be treated in term of a third-order nonlinear susceptibility. From the equation (2.1) the third-order nonlinear response of an isotropic medium is given by:

$$P_i^{(3)} = \epsilon_0 \sum_{j,k,l=x,y,z} \chi_{ijkl}^{(3)} \mathcal{E}_j \mathcal{E}_k \mathcal{E}_l \qquad (2.9)$$

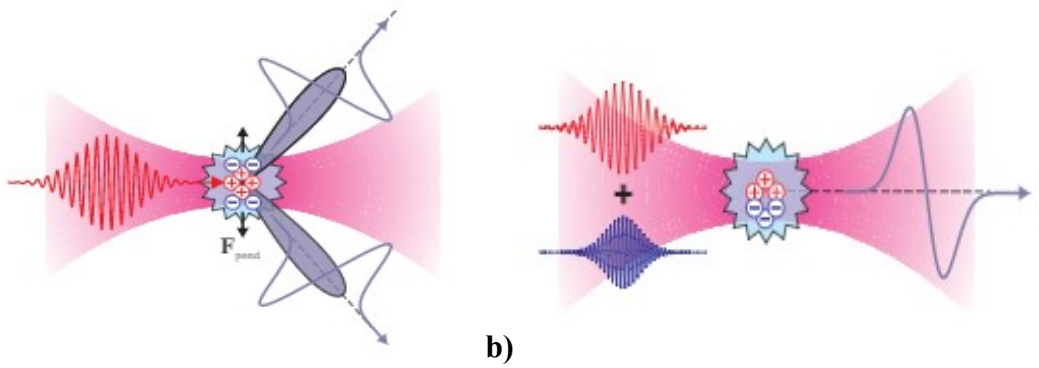

a) **b)**

Figure: 2.3: THz radiation is generated by: a) ponderomotive force, b) by four waves mixing process[47].

Where $\chi^{(3)}_{ijkl}$ is the third-order nonlinear susceptibility tensor, four-rank tensor with 81 elements, and i, j, k are one of the x, y, z Cartesian coordinates. However, the symmetry acquires that many elements of the rank tensor are the same or zero, resulting the number of the components is narrow down to 30 elements.

In the isotropic media, the second-order rank tensor is 0 due to the inversion symmetry. Hence, the third-order susceptibility tensor dominates and is the lowest order nonlinear susceptibility contributing to THz generation.

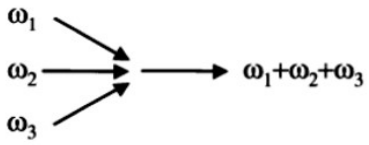

Figure 2.4: Four-wave mixing generation.

The THz generated by polarization-induced by four wave mixing process depend on the relative phase of the fundamental and its second harmonic pulses. The third-order susceptibility tensor is assumed to be instantaneous since occurring from the neutral or field-ionized media, resulting in the third-order polarization:

$$P_i^{(3)}(t) = \gamma_{ijkl} E_j^{2\omega_0}(t) E_k^{\omega_0}(t) E_l^{\omega_0}(t) \tag{2.10}$$

Substitution E_k and E_l with 800nm pulse (ω_0), Ej with 400nm pulse ($2\omega_0$) leads to:

$$E_k(t) = E_l(t) = 1/2\mathcal{E}_{800}(t)\exp(i\omega_0 t) + \text{c.c.} \tag{2.11}$$

$$E_j = 1/2\mathcal{E}_{400}(t)\exp[i(2\omega_0 t + \varphi)] + \text{c.c.} \tag{2.12}$$

Here, φ is the phase difference between the two pulses.

The produce of E_k and E_j results in a $4\omega_0$ term, a $2\omega_0$ term, and a rectified term. 400 nm pulse is a second harmonic of 800 nm pulse so,

$$\bar{\mathcal{E}_{400}(t)} \propto \mathcal{E}^2_{800}(t) \tag{2.13}$$

And

$$P_i^{(3)}(t) \propto \mathcal{E}^4_{800}(t)\cos\varphi \tag{2.14}$$

For the far field, Maxwell's equation dictates that:

$$E_{\text{THz}}(t) \propto \ddot{P}(t). \tag{2.15}$$

The electric field of the THz radiation is proportional to the second derivative of the third-order polarization.

2.1.2.3 Detection THz field by electro-optical (EO) sampling

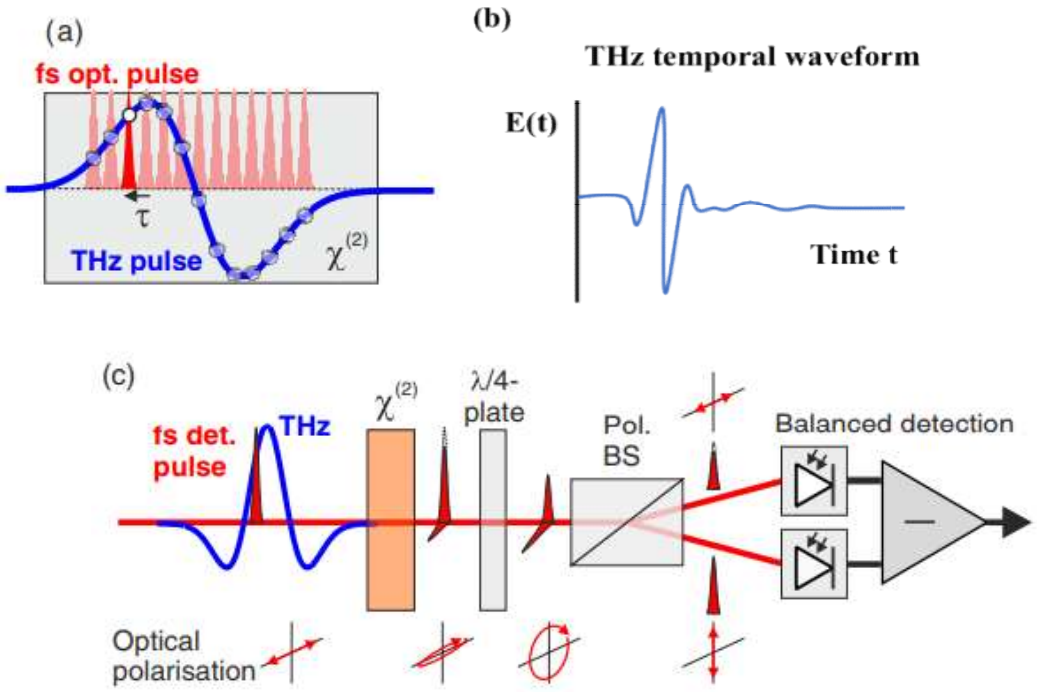

Figure 2.5: (a) Time-domain sampling of a THz pulse using fs-optical gate pulses as a function of pulse delay τ. (b) Example of the time-domain THz electric field E(t). (c) Schematic diagrams illustrating THz wave detected by optical rectification in nonlinear crystal[40].

Electro-optical sampling is employed to probe THz radiation by following the linear Pockels effect in EO crystal. EO sampling can be estimated as a reverse process of OR. The electric field of the THz induces birefringence in the nonlinear crystal, that leads to changing the polarization of the probe beam. By measuring the change, the THz electric field can be determined. Moreover, the phase of linearly polarized probe beam co-propagating inside the EO crystal is modulated by the refractive index of the crystal change causing by the electric field of the THz. Hence, EO sampling can detect both the phase and intensity of the THz pulses.

With this technique, balanced measurement is commonly used. Fig. 2.5 illustrates THz pulses detected by OR in the nonlinear crystal.

The linearly polarized probe beam propagates inside the crystal without the THz pulse, passing through the EO crystal without undergoing birefringence, and then becoming circular polarization after going out of the quarter plate. A polarizer (can be Wollaston prism) is used to separate the circularly polarized probe beam into s and p polarizations, which then are detected by a pair of balanced detectors. The detector is connected to a lock-in amplifier, collecting the different value $S= I_y - I_x$ from two photodiodes of the balanced detector.

The ellipsoid of the refractive index of EO crystal (for a zincblende crystal such a ZnTe) is:

$$\frac{x^2+y^2+z^2}{n_0^2} + 2\gamma_{41}E_x yz + 2\gamma_{41}E_y zx + 2\gamma_{41}E_z xy = 1 \quad (2.16)$$

Here, x, y, z are coordinate units of the ellipsoid in Cartesian coordinates. E_x, E_y, E_z are the applied electric field along the relative axis. n_0 is the refractive index of the crystal without the electric field. γ_{41} is EO coefficient of the crystal. Γ, which is the phase delay between two polarized components, is calculated by the change of the refractive index.

$$\Gamma = \frac{2\pi d}{\lambda}\Delta n \quad (2.17)$$

where Δn is the difference between long and short axes of the ellipsoid, d is the thickness of the EO crystal.

2.1.3 THz time domain spectroscopy

Properties of materials in far infrared have been studied for more than one century since the pioneering work of J. Bose et al.[48]. Until the 1980s, the Fourier Transform Infrared (FTIR) spectrometer was emerged and became the most powerful tool to access far-infrared properties of materials. During the 1970s, the emergence of the mode-lock laser has allowed scientists to generate short electrical pulses by means of nonlinear crystals[49] or in the fast response of semiconductor photowitches[50]. Generated short electrical pulses also led to emit short electromagnetic pulses propagating in free space.

In 1982, the first femtosecond mode-locked laser was introduced and the generated spectrum spread from 0.1 THz to several THz. The first use of THz pulses studied materials or gases were reported in the late 1980s. The experimental method then started to express as THz time-domain spectroscopy (THz-TDS).

THz-TDS is one of the most powerful tools to investigate the response of materials in the far infrared region. THz-TDS allows us to identify the amplitude and the phase of THz pulses that are transmitted, reflected or scattered by the sample, with or without loss of coherence. The absorption coefficient and refractive index of the sample are calculated from the obtained amplitude and phase of the THz signal. Therefore, one can calculate the complex permittivity of the sample without using Kramers-Kronig transformation. That makes THz-TDS becoming the convenient method to determine the complex permittivity. In addition, one can extract the sample thickness, as well as diffraction and scattering parameters.

In recent years, THz-TDS has been reported as an impressive tool to carry out the interplay of intermolecular and intramolecular vibration[51, 52].

2.1.4 THz time domain attenuated total reflection spectroscopy and time-resolved attenuated total reflection spectroscopy

Attenuated total reflection (ATR) spectroscopy based on the phenomenon of total internal reflection which has been known and discussed by Newton, as shown in Fig. 2.6. In 1959-1960, ATR spectroscopy was contemporaneously built by Harrick[53] and Fahrenfort[54]. Harrick approached ATR from multiple reflection sides while Fahrenfort approached that from a single reflection side.

ATR spectrometer was first commercialized by Wilks Scientific (company). Multiple internal reflection ATR then became available in a number of standard sizes. In the early 1990s, the first use of ATR spectroscopy technique was in infrared spectroscopy. Later, the single reflection ATR spectroscopy became dominant spectroscopy technique in an IR spectroscopy.

THz time domain ATR spectroscopy (THz-ATR) was used to overcome[55,58] the drawbacks of THz-TDS in investigating samples dissolved in polar liquids (particular water)[59]. Highly absorbed solution studied by transmission spectroscopy encounters strong absorption from the liquid that causes the difficulty in observing important information from materials. The standard transmission THz-TDS was no longer suitable for carrying out highly absorptive samples. Therefore, THz-ATR spectroscopy was suggested the alternative approach for polar medium studies. THz-ATR spectrometer is one of the most efficient methods for investigating biomolecular studies[60] as well as intermolecular vibrational modes

of supramolecular. It also suits for measuring powder samples as well as for studying water, heavy water, and intermolecular stretching.

Time-resolved ATR THz spectroscopy (TR-ATR) has been reported in a few years. Its setup basically bases on THz-ATR spectroscopy's setup in which the third pulse is added as pump pulse to excite the sample. TR-ATR provides information about the sample solution on the excited state. Meanwhile, THz-ATR provides the static information of the sample.

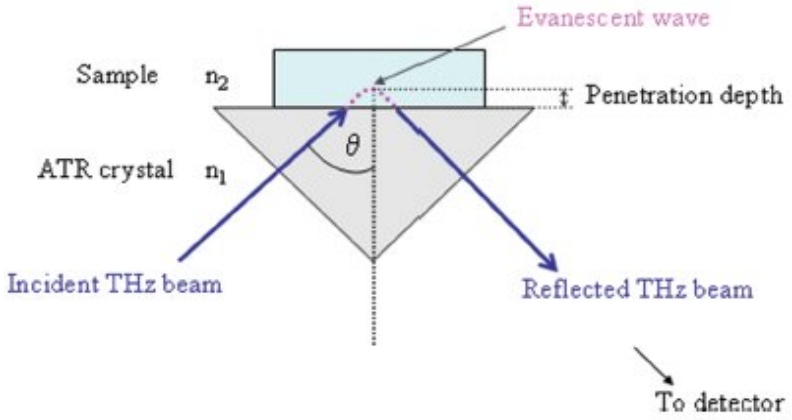

Figure 2.6: Schematic diagram of ATR spectroscopy.

Noncovalent interaction between molecules is very weak, the vibrational frequency of these interaction lies in the THz region, typically around 100 cm^{-1}, sometimes even lower than 50 cm^{-1} [61]. Interplaying between molecules themselves or molecules with other molecules have been attracted the great attention because these interactions are very crucial in living cells, catalysts and biochemistry materials. Hence, THz spectroscopy opens the new chapter of modern science.

2.2 Rhenium carbonyl diimine complexes

Rhenium carbonyl diimine complexes (Re complexes) were first discovered in the mid-1970s by Wrighton et al[62]. and the vast of following investigations have been reported so far. Rhenium (I) complexes have been used in various research applications due to its enormous richness in the photophysical and photochemical behavior of the excited states. They suit for phosphorescent labels and probing of biomolecules[63-67]. These complexes can be incorporated into supramolecular system, polymers or biomolecules because its excited states are tuned by structural variations and the medium[68,69]. Photostability together with intense photoluminescence and long-lived excited states make rhenium tricarbonyl diimine applicable for photosensitizer[70], sensors[71,72] or organic light-emitting device emitters[73].

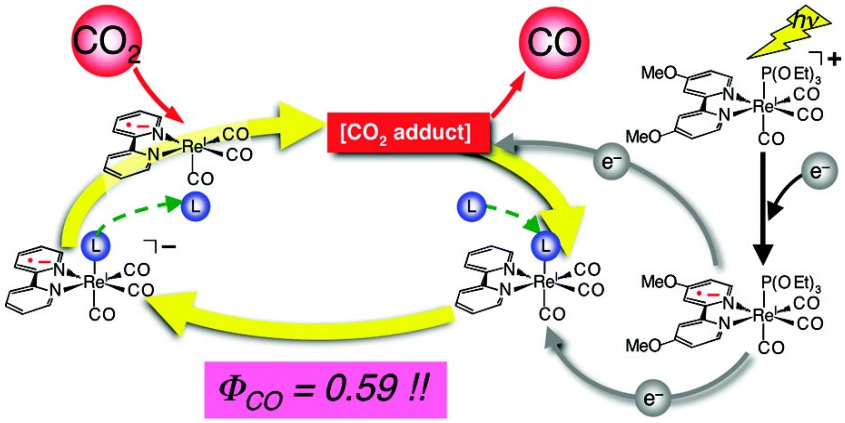

Figure 2.7: Schematic diagram of reduction of CO_2 process by photocatalyst [Re(4,4'-Me_2bpy) $CO)_3${$P(OEt)_3$}][31].

Importantly, Re complexes are well-known as the promising photocatalyst for CO_2 reduction[17-26] to selectively produce CO efficiently with high quantum yield. The remarkable feature of CO_2 reduction system is that one single photocatalyst utilizes one single electron transfers in the multielectron reduction of CO_2. Possessing one-electron reduced species and excited states which are reproduced by light absorption makes it becomes the best candidate for reducing CO_2. Indeed, global warming caused by the increasing of CO_2 concentration in the atmosphere and the depletion of fossil fuels are the two main problems that we have to deal with in the future. Is it possible to have a material that can harvest solar energy - an endless source to reduce CO_2 and reproduce CO, which is a new energy source? Re complexes are the materials that can meet the need.

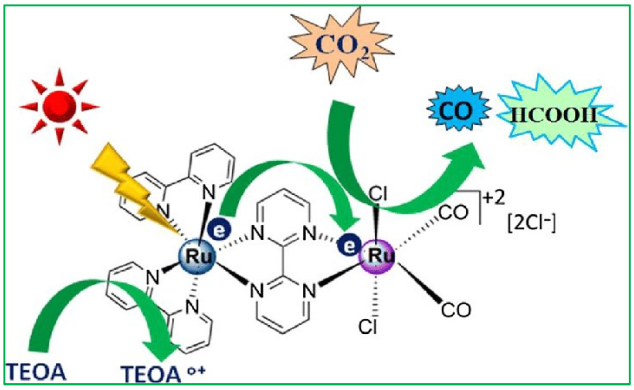

Figure 2.8: Schematic diagram of reduction of CO_2 process by Ru photocatalyst[74]

The reaction mechanism of the reduction CO_2 using the photocatalyst [Re(4,4'-Me_2bpy)$(CO)_3${$P(OEt)_3$}] is shown in Fig. 2.7[31]. The schematic shows the reductive quenching of the ^{3}MLCT state of this complex by TEOA and generates one-electron reduced species of [$Re^I(Me_2bpy^-)(CO)_3${$P(OEt)_3$}]$^-$. This process is more straightforward than that of

Ru photocatalyst and completely absent the formation of hydrogen and acid formic. Generally, in the photocatalytic cycle, $P(OEt)_3$ is removed and form the open site on Re center, then one CO_2 molecule coordinate to the Re center. Next, the CO adduct is replaced by $P(OEt)_3$ to give back [Re(4,4'-Me_2bpy) $CO)_3${$P(OEt)_3$}].

For example, in the case of $[Ru(bpy)_3]^{2+}$ as a typical example of redox photosensitizer[25] is mixed with the catalyst $[Ru(bpy)_2(CO)_2]^{2+}$ in the presence of the reductant, as shown in Fig. 2.8. Photochemical electron transfer can be generated by one electron transfer, and then the catalyst can convert photochemical one electron transfer to the multi-electron reduction of CO_2. One electron reduced species $[Ru^{II}(bpy^{-})(bpy)_2]^{+}$ is giving by sequential processes of exciting $[Ru(bpy)_3]^{2+}$ and quenching of its lowest excited state (^{3}MLCT) by the reductant. Reduction of CO_2 process is proceeded via electron capture by the catalyst $[Ru(bpy)_2(CO)_2]^{2+}$. A CO_2 molecule coordinates to an open site on the Ru center, which is produced by dissociation of one of CO ligands by reduction of $[Ru(bpy)_2(CO)_2]^{2+}$. After that, the process undergoes a complex reaction to the solution to reproduce $[Ru(bpy)_2(CO)_2]^{2+}$. The pH of the solution decides the reaction product of CO_2 such as HCOOH or CO.

It is necessary to understand some general aspects of Re complexes' electronic structure before discussing the spectroscopic and photophysical properties of these complexes.

2.2.1 Electronic structure of the Re complexes

Re is a metal transition of group 7 in the periodic table. Figure 2.9 shows a basic ligand field model for a transition metal octahedral complex. This simplified diagram illustrates the transitions possible for the electronic absorption spectra the complexes.

In octahedral complexes, the 5d orbitals of the metal are split into three t_{2g} (nonbonding) and two e_g^* (antibonding) molecular orbitals.

In the ground state configuration of the complex, the σ_L and π_L molecular orbitals are filled. The π_M molecular orbitals are either partially or totally filled depending on the number of d electrons in the transition metal ion. The higher orbitals σ_M^* and π_L^* are generally empty. There are many different allowed transitions between different molecular orbitals. These transitions are responsible for the various bands, which appear in absorption spectra.

Here:

σ_L ligand-centered orbitals: strong bonding

π_L ligand-centered orbitals

Non-bonding π_M (t_{2g}), metal-centered d orbitals

Anti-bonding σ_M*(e_g), metal-centered d orbitals

Ligand-centered, antibonding π_L* orbitals

σ_M* metal-centered orbitals: strong anti-bonding

MC: Metal-centered, MLCT: metal-to-ligand charge transfer, LMCT: ligand-to-metal charge transfer, LC: Ligand-centered

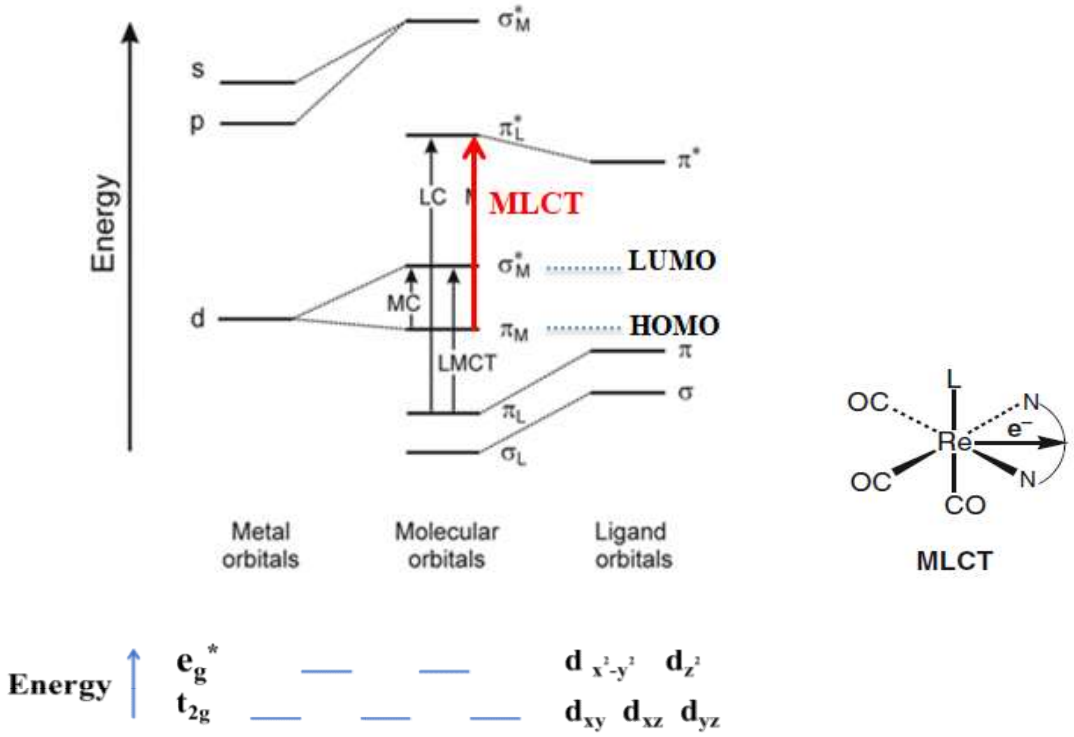

Figure 2.9. Molecular orbital diagram of an octahedral transition metal complex. The different types of electronic transitions are shown.

2.2.2 Photophysical properties of rhenium carbonyl diimine complexes

To understand Re complexes, structural and dynamics properties in the excited state of these complexes are necessary to review. Thus, this section will focus on discussing the relaxation processes of Re complexes studied by various spectroscopies.

2.2.2.1 Optical excitation

The lowest absorption bands of these complexes $[Re(L)(CO)_3(N,N)]^n$ are in near UV regions, corresponding to MLCT or MLLCT (metal-ligand-to-ligand charge transfer, herein $Re(L)(CO)_3 \rightarrow N,N$) and intraligand IL(N,N)[75-80]. In most cases, charge transfer (CT) bands lie at slightly longer wavelengths (330 - 400 nm) than the more intense IL (N,N) band. Most dynamics studies are operated with 400 nm laser excitation pulse that is directed to the lowest CT absorption band which is a singlet excited state.

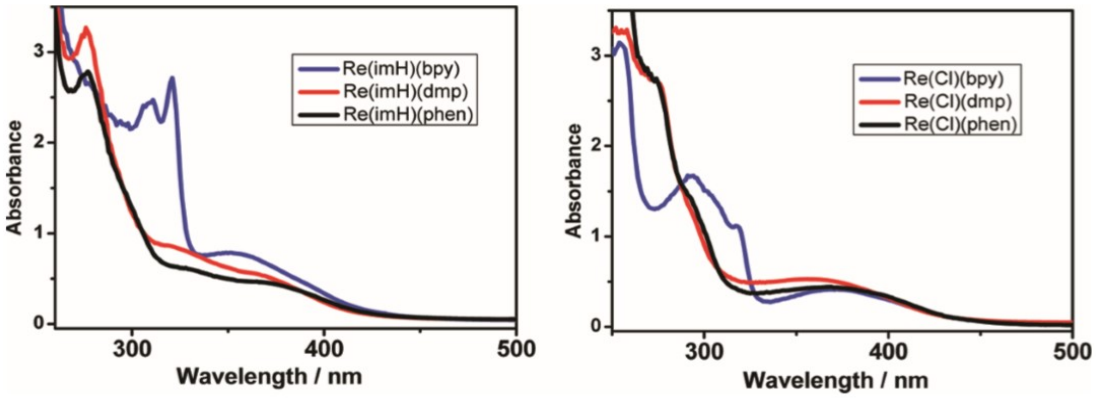

Figure 2.10: Absorption spectra of $[Re(imH)(CO)_3(N,N)]^+$ (left) and $[Re(Cl)(CO)_3(N,N)]$ (right) in DMF[81].

The absorption spectra[81] of $[Re(imH)(CO)_3(N,N)]^+$ (left) and $[Re(Cl)(CO)_3(N,N)]$ (right) in DMF display a few different absorption bands, as shown in Fig. 2.10. The spectra show the strong absorption band occurs in the near-UV region, this band corresponds to bipyridyl based (π-π^*) transition[82-84], and broadband observed of 350-420 nm absorption is assigned to $Re(L)(CO)_3 \rightarrow N,N$[85] CT transition.

2.2.2.2 Dynamics of singlet excited state and intersystem crossing

From the singlet excited state of $[Re(X)(CO)_3(bpy)]$ (X=Cl, Br), fluorescent is emitted with very broad band peak at ~530 nm[86]. The energy dissipation and ultrafast population of many vibrational bands are evidenced by the large fluorescent Stokes shift and broadness. The fluorescent converts to long-lived phosphorescence occurring at ~580 – 610 nm, depending on the ligand. The fluorescent decays with the lifetime (80-140 fs)[87], while the phosphorescence rises with lifetime τ_1 and τ_2, the latter in the range 300-1200 fs, [87], as shown in Fig. 2.11.

The mechanism in Fig. 2.11 shows that the singlet state b^1A' undergoes two parallel intersystem crossing (ISC) processes, populating simultaneously b^3A'' (^{3}IL) and a^3A''

(^{3}MLCT lowest state). The lifetime τ_2 then contributes to internal conversion between b^3A" and a^3A".

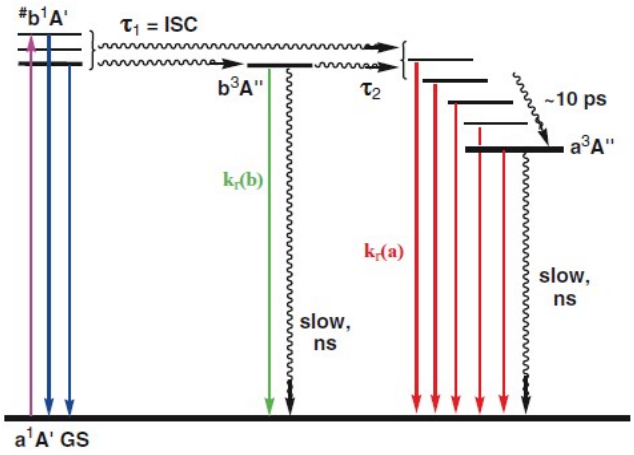

Figure 2.11: Diagram of excited-state dynamics[87] of $[Re(CO)_3(L)(bpy)]^n$, L= Br, Cl, Etpy. Light absorption to b^1A' in violet, fluorescent in blue, b^3A" phosphorescence in green, a^3A" phosphorescence in red. Hash denotes vibrational excitation. These states a^1A', b^1A', b^3A", a^3A" correspond to the ground state, singlet excites state, triplet excited state, triplet ground state, respectively.

2.2.2.3 Excited state dynamics studied by fluorescence up-conversion

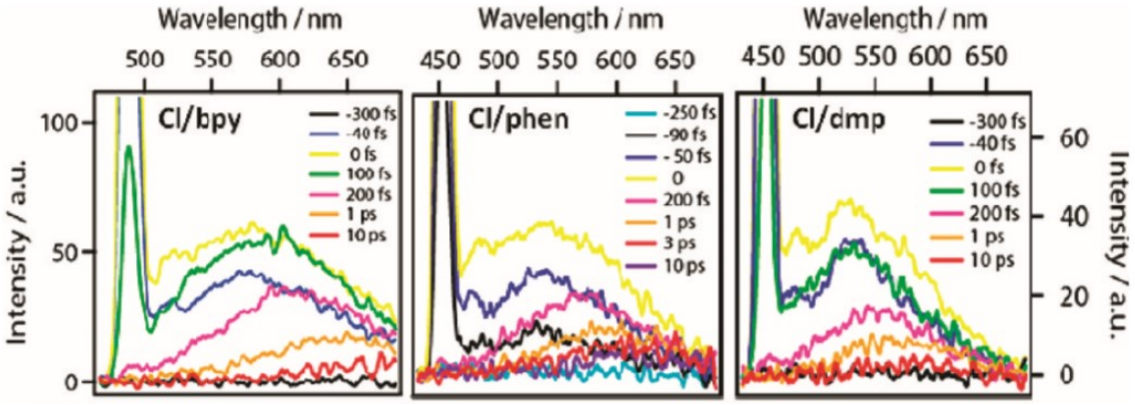

Figure 2.12: Luminescence spectra[30] of $[Re(L)(CO)_3(N,N)]^n$ in DMF measured at selected time delays after 400 nm, 100 fs excitation. The peak at 453 nm is the DMF Raman line.

Fig. 2.12 shows luminescence spectra of $[Re(L)(CO)_3(N,N)]^n$ in DMF at selected time delays after 400 nm. The broad intense fluorescence spreading from 530-540 nm emerges with the photoexcitation. It is assigned[30,87] to the optically populated singlet excited state(s) of a $Re(L)(CO)_3 \rightarrow N,N$ CT origin. The fluorescence rapidly evolves into weak long-lived phosphorescence at slightly longer wavelengths. For $[Re(L)(CO)_3(N,N)]^n$, the

fluorescence decays with two kinetic components τ_1: 97, 108, and 110 fs and τ_2: 1.1, 2.4, and 2.7 ps for bpy, phen, and dmb, respectively.

2.2.2.4 Excited state dynamics studied by time-resolved infrared spectroscopy

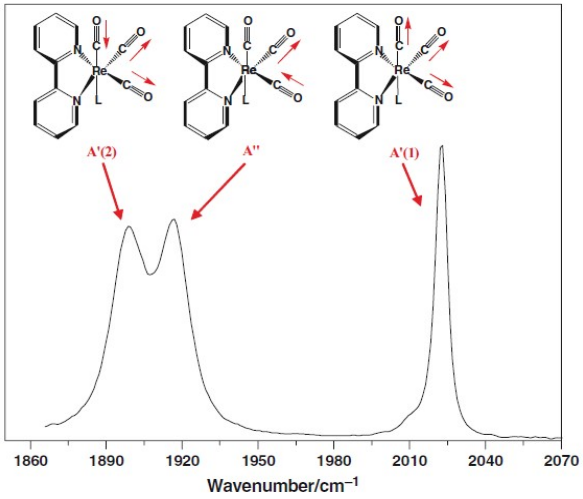

Figure 2.13: FTIR spectrum[86] of $[Re(Cl)(CO)_3(bpy)]$ in MeCN and the corresponding υ(CO) vibrations.

Ground-state IR spectra[87] of $[Re(L)(CO)_3(N,N)]^n$ show three IR bands due to C≡O stretching vibrations, υ(CO) in the range of ~1900 - 2040 cm^{-1}, which are schematically shown in Fig. 2.13. The highest band corresponds to a totally symmetric in-phase υ(CO) vibration, denoted A'(1). The two lower bands belong to the out-of-phase totally symmetric A'(2) vibration and the asymmetric vibration of the equatorial CO ligands, A". These two vibrations occur at similar energies and the separation of the corresponding bands depends on the axial ligand L. Two well-developed bands are observed in complexes with halide-, O- or P-coordinated ligands. On the other hand, the A'(2) and A" bands are merged into one broad band if L is N-coordinated, e.g., pyridine, imidazole or NCS−. They can become slightly separated (by 10–15 cm^{-1}) upon changing the solvent or embedding the Re unit into a supramolecular environment.

Excited Re complexes with 400 nm excitation into the red edge of their lowest absorption MLCT band (~7000 cm^{-1} above the lowest triplet state), the kinetic of the system experiences two parallel intersystem crossing (ISC) process, which populating simultaneously triplet excited states. Triplet states are initially formed "hot", that is no equilibrated both in the molecule structure and the medium.

The relaxation of triplet excited state is interpreted through intramolecular vibrational energy distribution into low-frequency modes and vibrational energy relaxation by dynamic up-shift of the A'(1) υ(CO) band in IR region and UV-Vis spectra indicating structure changes within chromophore. Dynamic IR shift during solvent relaxation can be explained by electrons transfer from $Re(L)(CO)_3$ and anharmonic coupling of IL-CT bands.

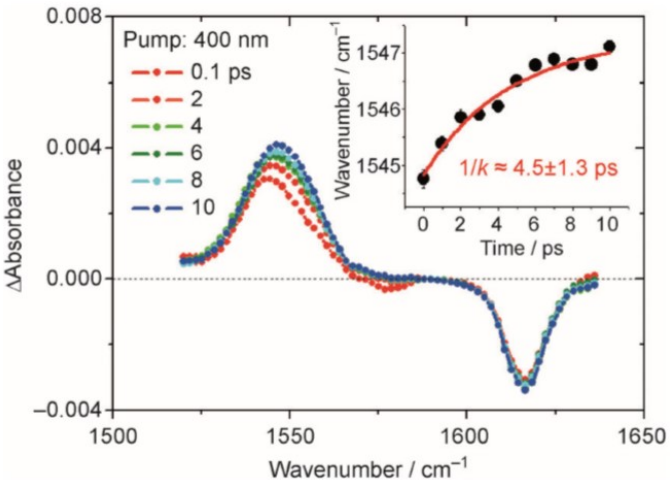

Figure 2.14: TR-IR spectra[34] of a solution fac-$[Re(bpy)(CO)_3Cl]$ in THF using an excitation wavelength of 400 nm. The inset shows the center wavenumber of the absorption peak as a function of the delay time.

Time-resolved spectroscopy such as time-resolved infrared (TR-IR) spectroscopy is used to investigate and interpret the excited state of Re complexes.

Figure 2.14 shows new absorption peak at 1545 cm^{-1} and a negative peak at 1616 cm^{-1} were observed just after photoexcitation. These are attributable to vibrational stretching bands of the bpy ligand. The negative peak does not change within 10 ps, the positive peak was blue-shifted up to 1547 cm^{-1} with 1/k = (4.5±1.3) ps.

Two positive absorptions, the very broad absorption peak between 1830 and 1870 cm^{-1} and the absorption at 1950 cm^{-1} were observed along with two negative peaks at 1893 and 1917 cm^{-1}, as shown in Fig. 2.15. These absorptions were attributed to the decrease of CO stretching bands in the ground state.

The peak at 1950 cm^{-1}, contributable to the ^{3}MLCT excited state of fac-$[Re(bpy)(CO)_3Cl]$, sharpened and split into two peaks at 1955 and 1991 cm^{-1}, which are related to two of three CO stretching bands of ^{3}MLCT(LV) with lifetime (5.9±0.3) ps. These behaviors likely result from the relaxation of ^{3}MLCT(HV) to ^{3}MLCT(LV).

The photophysical processes of fac-[Re(bpy)$(CO)_3$Cl] in THF following by 400 nm excitation can be summarized in Fig 2.16.

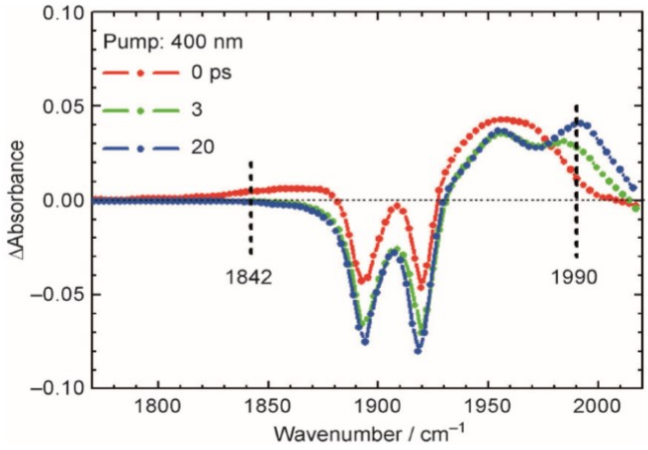

Figure 2.15: TR-IR spectra of a solution of fac-[Re(bpy)$(CO)_3$Cl] in THF at 0, 3, and 20 ps using a 400 nm laser pulse for excitation[34].

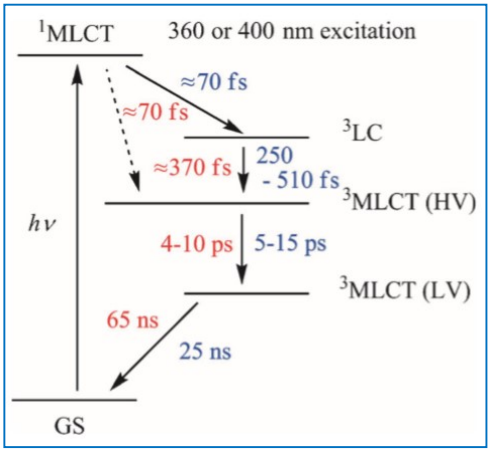

Figure 2.16: Photophysical processes of fac-[Re(bpy)$(CO)_3$Cl] following excitation at ≥ 360 nm in THF (lifetimes in red) and MeCN (lifetimes in blue) [34].

2.2.3 [Re(bpy)$(CO)_2${P$(OEt)_3$}$_2$](PF_6) complex

We are interested in the photocatalyst [Re(bpy)$(CO)_2${P$(OEt)_3$}$_2$](PF_6) and use it in study the interaction of the intermolecular interaction of solute-solvent molecules because it can act as both electrocatalyst and photocatalyst for the reduction CO_2[88-91] Furthermore,, [Re(bpy)$(CO)_3${P$(OEt)_3$}](PF_6) (bpy= 2,2'- bipyridine ($C_{10}H_8N_2$)) sort of a unique complex due to its unique photocatalyst abilities, which can work without supporting of another complex like photosensitizer or catalyst[26]. The Fig. 2.17 shows the higher quantum yield

(Φ=0.38) of the reduction of CO_2 by the similar photocatalyst $[Re(bpy)(CO)_3\{P(OEt)_3\}]^+$ complex in DMF-TEOA.

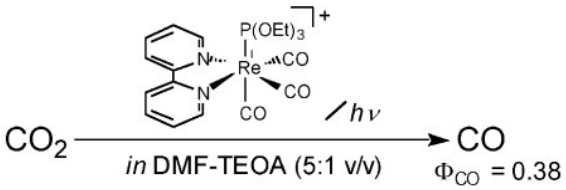

Figure 2.17: The reduction of CO_2 by $[Re(bpy)(CO)_3\{P(OEt)_3\}]^+$ in DMF-TEOA solvent with quantum yield is 0.38.

Comparing to other complexes in the same family, $[Re(bpy)(CO)_2\{P(OEt)_3\}_2](PF_6)$ provides the highest quantum yield of CO formation (Φ= 0.38 by excitation with 356 nm). Moreover, this complex has long-lived excited state (~250ns) and is fairly stable in solution at room temperature due to the strong electron-withdraw property of $P(OEt)_3$ ligands.

a) 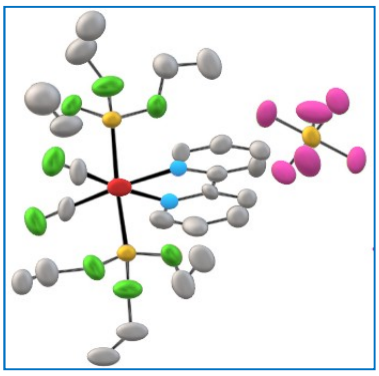 b) 

Figure 2.18: a) The 3D structure of $[Re(bpy)(CO)_2\{P(OEt)_3\}](PF_6)$complex. Color denotes: Rhenium- red, Oxygen- green, Carbon- grey, Phosphate- orange, Oxygen- red, Nitrogen-blue, Flo-pink. b) $[Re(bpy)(CO)_2\{P(OEt)_3\}](PF_6)$ complex powder.

Fig. 2.18a) displays the 3D molecular structure of $[Re(bpy)(CO)_2\{P(OEt)_3\}](PF_6)$. The $[Re(bpy)(CO)_2\{P(OEt)_3\}](PF_6)$ powder have yellow color as shown in Fig. 2.18 b). The structure of bpy and $P(OEt)_3$ ligands are shown in Fig. 2.19. Each kind of atom is denoted by a different color.

a) 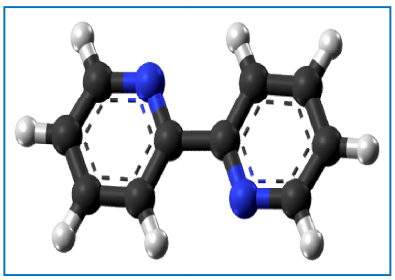 b) 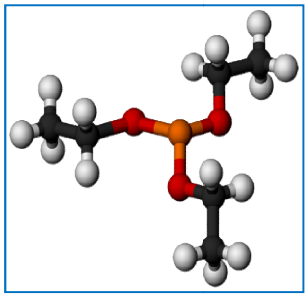

Figure 2.19: a) The structure of 2,2'-bipyridine ($C_{10}H_8N_2$). Color denotes: Carbon-black, Hydrogen-white, Nitrogen-blue. b) 4,4'-dimethyl-2,2'-bipyridine ($C_{12}H_{12}N_2$). Color denotes: Carbon-grey, Hydrogen-white, Nitrogen-blue. c) Triethyl phosphite $P(OEt)_3$ $(C_2H_5O)_3P$. Carbon: black- Hydrogen: white, Oxygen: red, Orange: phosphate.

Chapter III

Experimental methods

In this chapter, the experimental setup of THz-TDS and time-resolved attenuated total reflection THz spectroscopy (TR-ATR) are described. THz radiation generated and detected by nonlinear crystals and air plasma as well as the experimental data obtained from our spectrometers are presented. Data collection and extraction optical constant from the experimental measurement are discussed in this section. Furthermore, the spot size of THz and pump beams measured by the edge-cut method is introduced.

Ti-sapphire laser with the center wavelength of 800 nm, the repetition rate of 1 kHz, the pulse width (FHWM) of ~ 70 fs and the power of 1 W is used to generate THz radiation due to highly suitable phase matching with ZnTe crystals.

In this study, we constructed time-resolved THz spectroscopy (TRTS) because it can change into TR-ATR and THz-ATR by inserting a silicon prism at the focal point of the THz beam. Moreover, TRTS easily changes to THz-TDS by switching off the pump excitation. With that benefit of such a setup, one can measure both ground state structure and excited state dynamics of materials.

TR-ATR using the Si prism is the brand-new spectroscopy so far. The conventional THz-ATR has been using for a long time to measure highly absorbing medium, which cannot measure by transmission spectroscopy. For polar liquid and strongly absorbing materials, TR-ATR allows use to access dynamics of the excited state in the THz region.

3.1 THz time domain spectroscopy

3.1.1 THz generated and detected by nonlinear crystals

In the TRTS setup, ZnTe crystals (thickness: 1mm) are used in both generating and detecting of THz radiation in the range of 0.3 - 2.5 THz.

Figure 3.1 shows the detailed schematic of the typical TRTS. Ti-sapphire laser beam splits into three arms: the THz generation beam, the THz detection (probe beam) and the pump beam. Two third of laser power is used for the pump beam, while the rest generates

and detects THz pulses. In this setup, the power of the THz generation beam is from 45 mW to 50 mW to achieve the best signal to noise (S/N) ratio and also to avoid breaking the generator crystal.

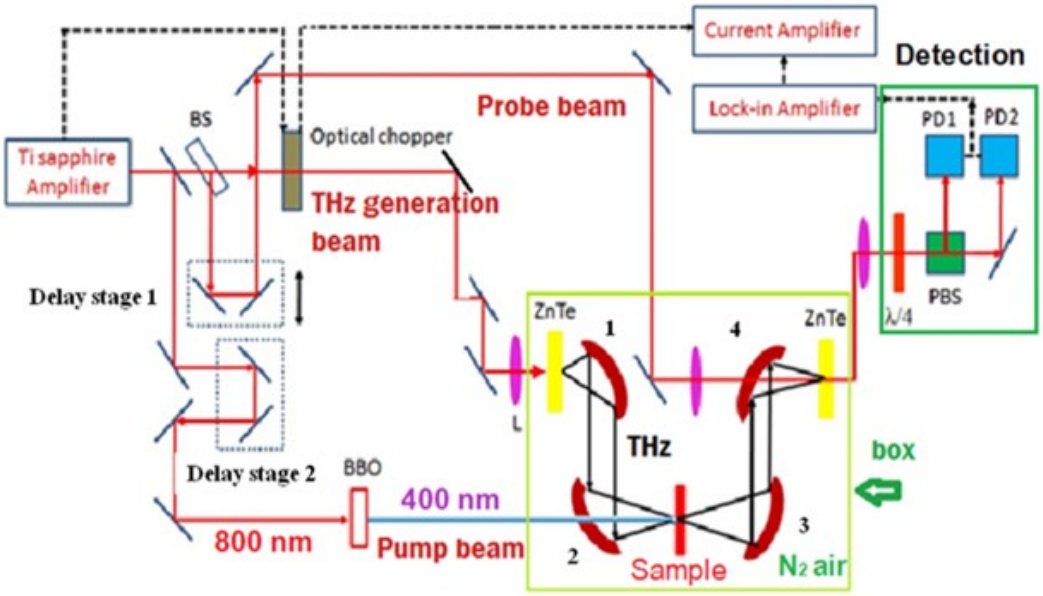

Figure 3.1: Schematic diagram of TRTS generated and detected by the nonlinear crystal. BS: beam splitter, PD1, PD2: photodiode. Number 1,2,3,4 are represented the position of parabolic mirrors. The set of four off-axis parabolic mirrors is put in the box which is purged by N_2 air.

The THz generation beam is focused by the lens with the focal length of 5 cm before propagating through a ZnTe (110) crystal to generate the THz beam. Next, the THz beam is propagating to the set of four parabolic mirrors and the residual of 800 nm beam is cut by the filter (the paper). In which, the first parabolic mirror collimates the THz beam and the second parabolic mirror focuses it into the sample. Finally, the THz beam is recollimated and re-focused by the third and the fourth parabolic mirrors to ZnTe detector crystal.

The delay stage 1 varies the time between the THz probe and generation beams to map out THz waveform, as discussed in section 2.1.2.2 of chapter II. The THz probe beam is focused by the lens and passes through the hole in the fourth parabolic mirror, from where it overlaps with the THz generation beam spatially and temporally on the ZnTe detector crystal. Finally, it is sent to the λ/4 wave plate which can change the elliptically polarized probe beam to a circularly polarized beam. This beam is sent to the detection part that connects to a lock-in amplifier.

An optical chopper is placed in the THz generation beam to reduce the frequency of the THz generation beam. The chopper is connected to Lock-in Amplifier that is set at a given frequency to remove noise frequency from other sources. The optical pump beam (400 nm) is generated by focusing 800 nm beam into a BBO (barium borate) crystal. To remove water vapor, THz generation and detection areas are put into a box that is purged by N_2 gas.

The pump beam propagates through the hole on the second parabolic mirror to excite the sample in the same direction with the THz beam. With this setup, the pump beam and THz beam have the best overlap spatially and temporally on the sample and also give the best time resolution. The delay stage 2 varies time delay between the pump and the THz beams to study dynamics processes inside materials in excited states.

The highest power of 400 nm pump beam can reach 6 μJ. The spot size of the pump and THz beam are ~1.7 mm, which were measured by knife cut-edge method, will be presented in the next section. Noted that, the pump beam size can be varied by changing or moving the lens.

Fig. 3.2 shows the THz waveform measured by THz-TDS, in which the spectrum emitted in the frequency region from 0.3 to 2.5 THz obtained by the fast Fourier transform (FFT) technique. The bandwidth is limited at the maximum of 2.5 THz due to phonon absorption of ZnTe. For our setup, the S/N of THz amplitude is approximately 7 order of magnitude, is fairly qualified. The bandwidth of the THz spectrum is also affected by the thickness of ZnTe crystals, the bandwidth expands when the thickness is thinner[106]. In Fig. 3.2b), the weak absorption owing to water vapor still remains as a small peak around 1.5 THz.

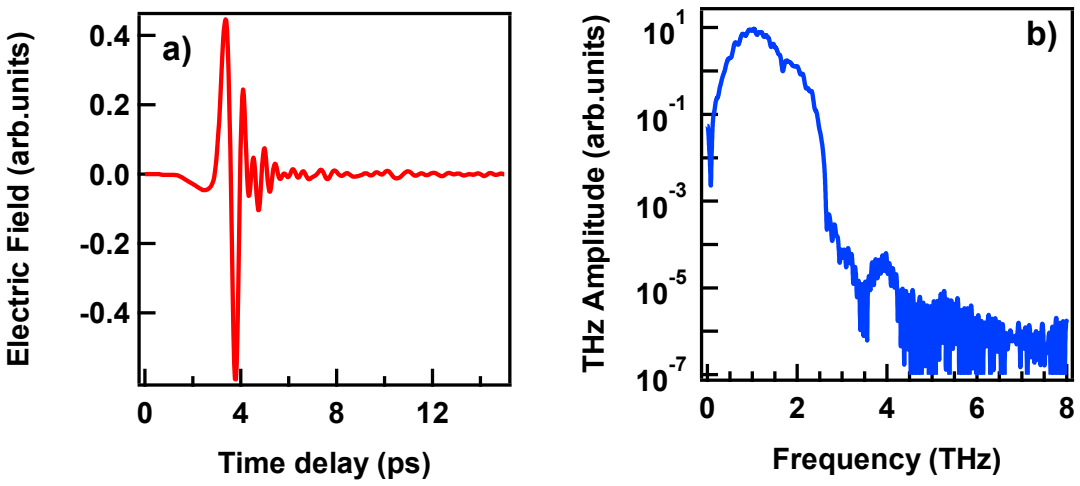

Figure 3.2: a) THz waveforms generated and detected by ZnTe crystals. b) Corresponding THz spectra from 0.3 THz to 2.5 THz obtained by fast Fourier transformation (FFT).

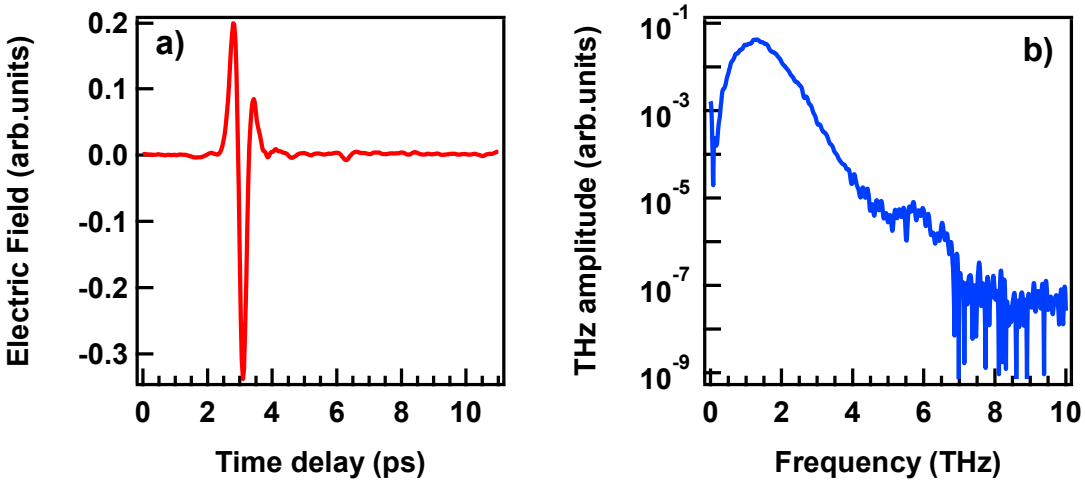

Figure 3.3: a) THz waveforms generated and detected by GaP crystals. b) Corresponding THz spectra from 0.3 THz to 7 THz obtained by FFT.

Fig. 3.3 shows the THz waveform generated and detected by GaP crystals, in which the spectrum emitted in the frequency region from 0.3 to 7 THz obtained by the fast Fourier transform (FFT) technique. The bandwidth is extended to 7 THz due to using GaP crystal. The S/N of the spectrum around 1 THz is approximately 5.5 order of magnitude . From 3 THz, the S/N decreases significantly due to the absorption of GaP phonon and phase matching condition.

In TRTS setup, there are two delay stages which allow the spectrometer to perform time domain scan, and pump scan in a pump-probe technique. However, in this study, we will not measure the dynamic of Re complexes by TRTR, thus the pump-probe technique will be presented in TR-ATR.

- **Time domain scan:**

Time domain scans are collected by scanning the delay stage 1 (in Fig. 3.1) with the chopper that chops the THz generation beam, while the pump beam is blocked. THz time-domain scan with and without the sample is shown in Fig 3.4. The sample delays, disperses, and attenuates the THz waveform. In measuring, the sample powder is sandwiched by two windows: a Z-cut quartz crystal and a Cu interference filter. The absorption and refractive index of the sample are usually measured by THz-TDS.

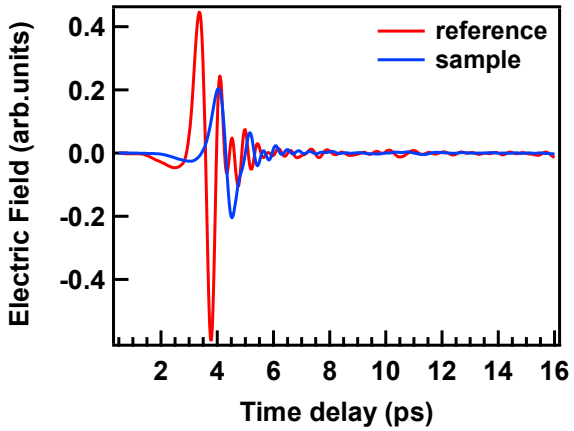

Figure 3.4: Time domain scan of a THz pulse with "sample" and without a sample "ref"- $[Re(CO)_2(bpy)\{P(OEt)_3\}_2](PF_6)$ + windows. The sample delays, disperses, and attenuates the pulse.

3.1.2 THz generated by air plasma, detected by nonlinear crystal

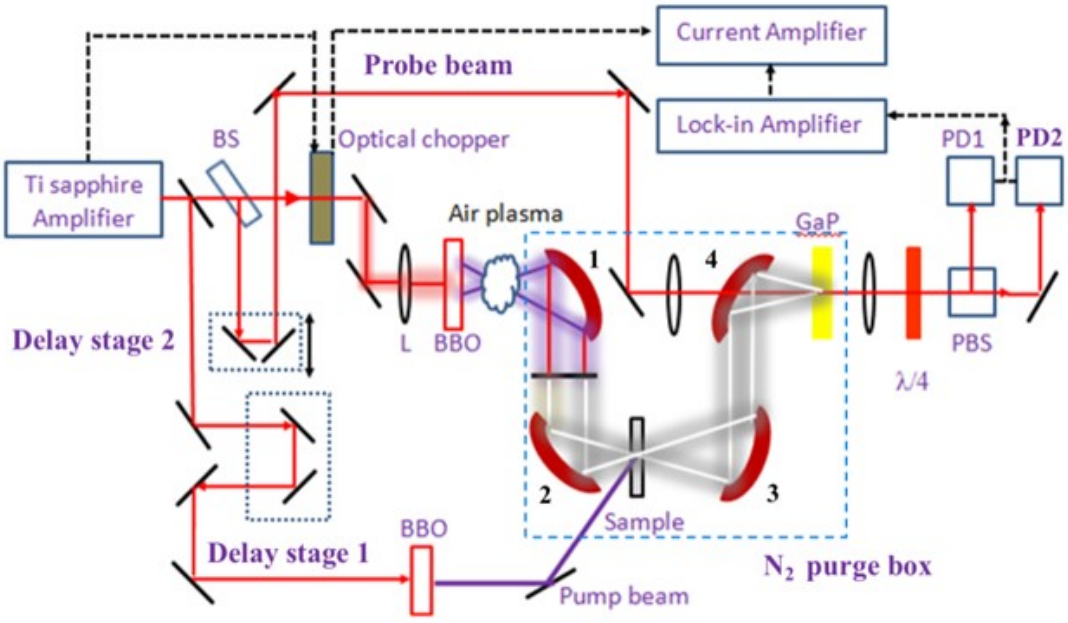

Figure 3.5: Schematic diagram of TRTS spectrometer generated by air plasma, detected by nonlinear crystal, GaP. BS: beam splitter; PD1, PD2: photodiode. 1,2,3,4, are a set of four off-axis parabolic mirrors.

Fig 3.5 shows TRTS setup using air plasma to generate THz radiation. THz emission is obtained by a four-wave-mixing nonlinear optical process induced by the air plasma[37], as discussed in section 2.1.2.1 in chapter II. In detail, focusing the intense 800 nm beam into BBO crystal to generate its second harmonic generation (400 nm) and the mixing of 400 nm

and the residual of 800 nm beams induce air plasma. As a result, THz pulses are emitted. In this method, the position of the BBO crystal plays the most crucial role. Only a few relative positions of BBO crystal and the lens L (see Fig. 3.5) can generate THz radiation. The lens L with the focal length of 250 mm and the distance between BBO crystal and this lens is 170 mm are found suitable to induce the intense THz pulse with high S/N ratio.

The air plasma is produced if the generated power overcomes the breakdown air molecules threshold (~150 mW). THz emission achieves the best-qualified S/N when the power reaches 220 mW. The THz intensity becomes saturation when the power of the generated THz beam is over 250 mW.

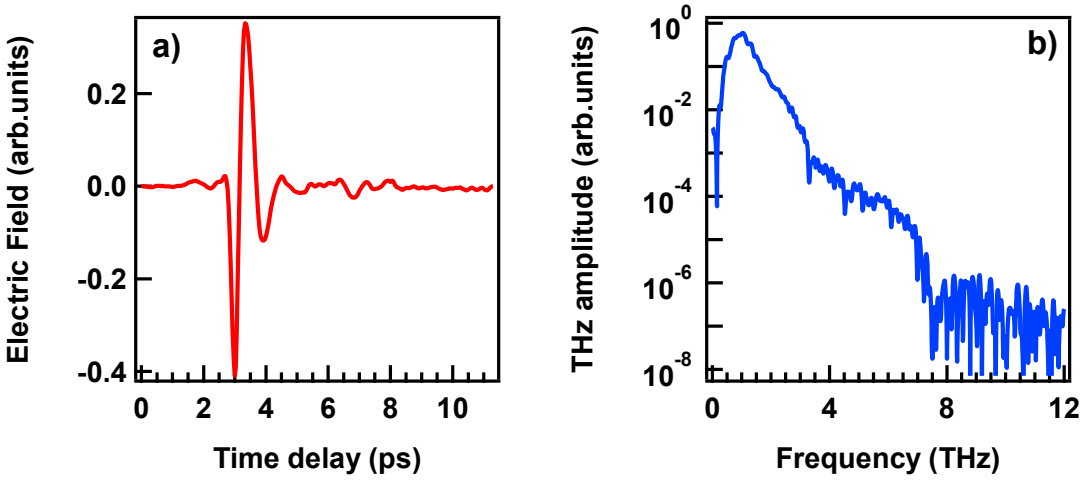

Figure 3.6: a) THz waveforms measured by THz-TDS transmission spectroscopy, in which air plasma and GaP cystal were used in generation and detection THz radiation, respectively. b) Corresponding THz spectra from 0.3 THz to 7 THz obtained by FFT.

Figure 3.6 shows the THz waveform generated by air plasma and detected by GaP crystal, and the corresponding THz frequency obtained by FFT. Although the bandwidth of THz generated by air plasma can span to a few ten of THz, the THz spectrum is broadened to 7 THz due to the detection by GaP crystal. The S/N ratio reaches 6 order of magnitude at 1 THz while from 4 to 7 THz, that is only 3.

Figure 3.7 shows the comparison of THz spectra generated by ZnTe crystal (green line), air plasma (blue line) and GaP crystal (red line). These spectra are offset (adjusted the noise level of all of the THz spectrum as equal to the noise level of the THz spectrum generated by GaP) in the purpose of comparing the noise level. The comparison shows air plasma method is the more efficient than GaP in generating intense and broadband THz radiation. In fact, the S/N ratio of the blue line is roughly 10 times higher than that of the red

line. The bandwidth of THz radiation generated by air plasma broadens to 7 THz, while that of GaP is 7 THz.

Obviously, the THz bandwidth generated by ZnTe is different from those by air plasma and GaP. Noticeably here, ZnTe-generated THz radiation has the highest S/N ratio than others in the frequency range of 0.5 to 2.5 THz. Therefore, ZnTe is the most suitable emitter for the THz generation in the range of 0.3 - 2.5 THz region and air plasma is the best source to generate broadband THz. Our spectrometer provides qualified THz pulse shape as well as THz bandwidth with a high S/N ratio and high intensity.

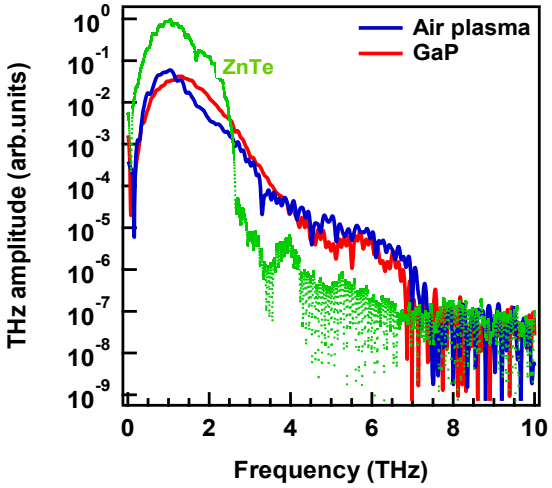

Figure 3.7: Comparison of THz spectra generated by ZnTe, GaP crystal and air plasma.

3.2 Time-resolved attenuated total reflection THz spectroscopy

3.2.1 Experimental setup

TR-ATR setup is based on the conventional TRTS' structure (Fig. 3.1), shown in Fig. 3.8. Importantly, the silicon prism is the core element in the spectrometer. TR-ATR measurement is supplied by an amplifier of femtosecond Ti: sapphire laser with 800 nm center wavelength, 1-kHz repetition, the pulse width of ~ 70 fs and 900-mW pulse power.

The laser beam is split into three arms which are used to generated and probed THz field and as the excitation pulse. One of the three pulses is applied to generated THz pulse using ZnTe (110) 1 mm of thickness. THz radiation is focused by the serial of four parabolic mirrors.

The THz spot size of ~3 mm at the sample position. The spot size is calculated by the following equation:

r= THz spot size (measured by a knife edge method ~1.8mm)/cos(37.5) (see Fig. 3.9).

The Si prism (refractive index $n_{Si} = 3.41$, base angle $\alpha = 37.5^{\circ}$, critical angle $\theta_i = 26^{\circ}$, incident angle $\theta_1 = 52.5^{\circ}$) is inserted into the THz path. The THz wave propagates inside the prism and induces the evanescent wave at the interfaces between the denser medium (Si prism) and the low-density medium ($n<n_{Si}$). This wave interacts with the sample and causes the change in the transmitted THz wave.

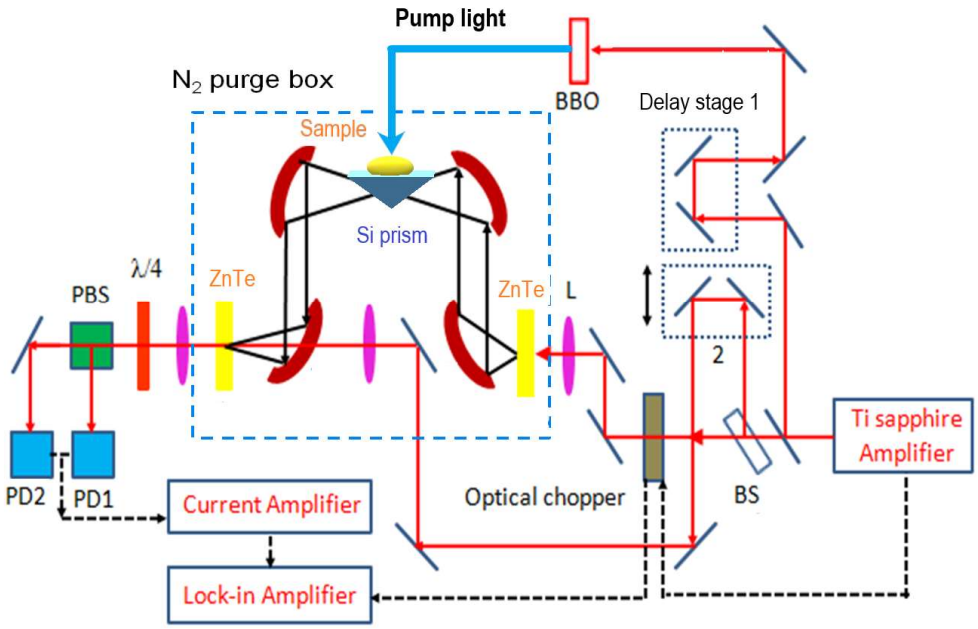

Figure 3.8: Schematic diagram of TR-ATR generated and detected by the nonlinear crystal.

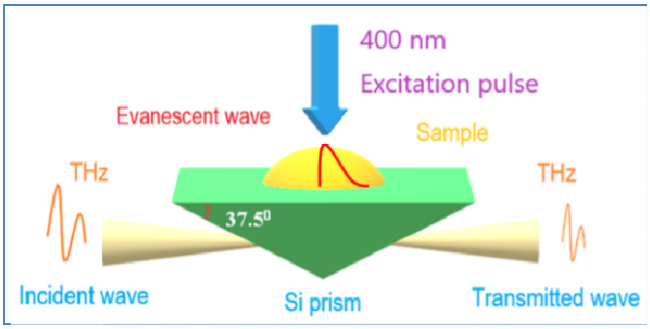

Figure 3.9: Diagram of the side view of Si prism in TR-ATR.

In the measurement, the sample is placed on the surface of the prism. THz propagating in free space is detected by electro-optical sampling on ZnTe (110) with the thickness of 1 mm. Nitrogen air was purged into the THz beam path in order to remove absorption of water vapor. The second harmonic of 800 nm using as pump pulse was generated by BBO crystal (400-μm thickness) with the pulse intensity of ~ 6 μJ. The spot

size (FWHM ~4 mm) of the pump beam is larger than the THz spot size to ensure the photo-induced phenomena. Photoexcitation beam's direction of TR-ATR setup is illustrated in Fig. 3.9.

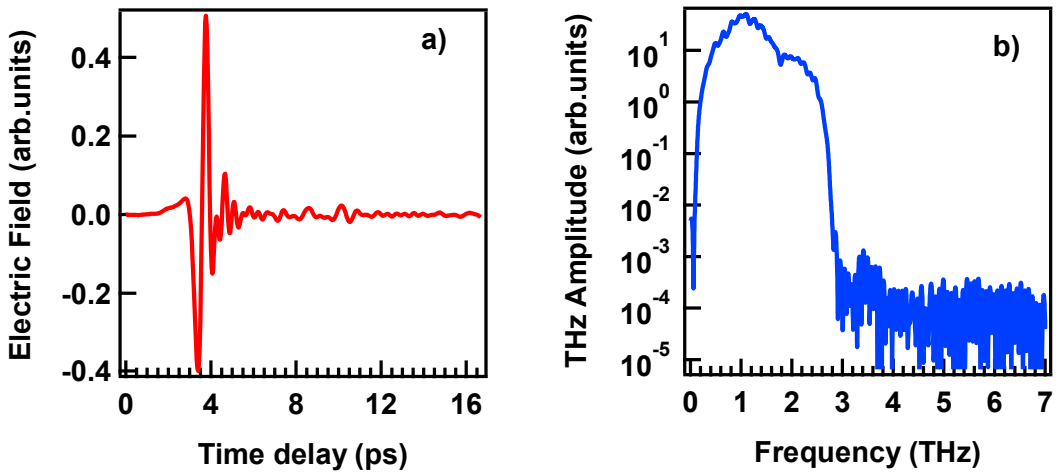

Figure 3.10: a) THz waveform measured by THz-ATR, generated and detected by ZnTe crystals. b) Corresponding THz spectra in the frequency from 0.3 to 2.5 THz obtained by FFT.

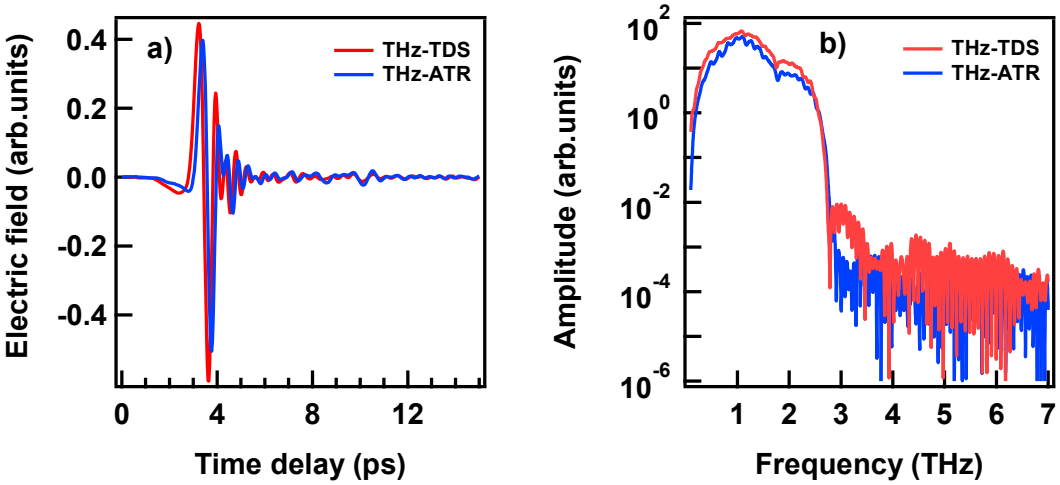

Figure 3.11: a) Comparison of THz waveforms obtained by THz-TDS and THz-ATR and b) corresponding THz spectra in the range from 0.3 to 2.5 THz obtained by FFT.

Fig. 3.10 shows the THz waveform measured by THz-ATR spectroscopy, generated and detected by ZnTe crystals, and the corresponding THz spectrum obtained by FFT. The THz bandwidth achieves 2.5 THz and the S/N ratio almost reach 5.5 order of magnitude at around 1 THz. The weak absorption around 1.65 THz is owned to water absorption, as shown in Fig. 3.10 b).

Fig. 3.11 shows the comparison of THz waveform measuredby THz-TDS (red line) and THz-ATR (blue line), and the corresponding THz spectra obtained by FFT. The THz spectra measured by both spectroscopies are similar in the S/N ratio. However, the bandwidth of blue line is wider than that of the red line, that originates from the different pulse duration, shorter pulse duration can generate broader THz bandwidth (100 fs for the red spectrum and ~70 fs for the blue spectrum).

Pump-probe measurment:

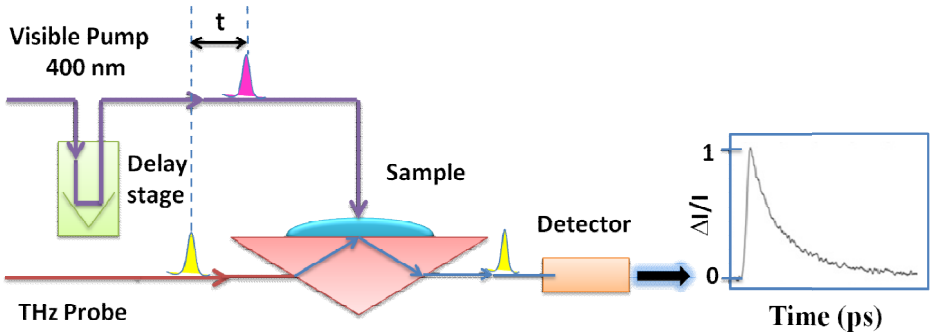

Figure 3.12: Pump-probe technique

Pump-probe measurement is the simplest experimental technique used to study ultrafast electronic dynamics. In this technique, a pump beam (400 nm) is used to excite the sample, generating a excited state, and a probe beam (THz beam) is used to monitor the pump-induced changes in the optical constants (such as reflectivity or transmission) of the sample, as shown in Fig. 3.12. Measuring the changes in the optical constants as a function of time delay between the arrival of the pump and probe pulses yields information about the relaxation of electronic states in the sample.

3.2.2 Evanescent wave in absorbing materials

The Si prism with the base angles of $\alpha = 37.5°$, $\theta_{atr} = 51°$, and $n_{Si} = 3.41$ used here is shown in Fig. 3.13. The incident angle $\theta_{atr} = 51°$ at the interface of Si-material or Si-air is calculated by the Snell's law.

The critical angle at the interface between Si and air by the Snell's law is $\theta_c = \arcsin(n_{Si}/n_{air}) = 26°$.

$$n_{Si} = 3.41, \alpha = 37.5^o, \theta_i = 52.5^o$$

$$\theta_{atr} = 51^o > \theta_c = \sin^{-1}\left(\frac{1.5}{3.41}\right) = 26^o$$

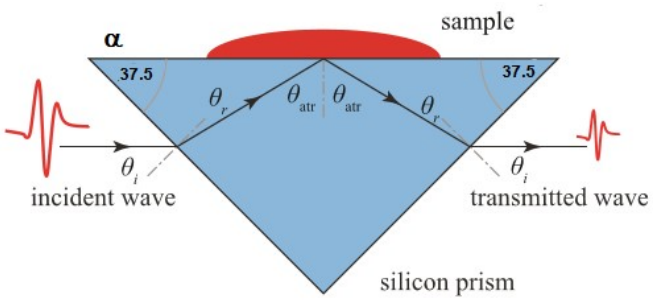

Figure 3.13: Detail parameters of Si prism.

The incident THz wave with an angle θ_i = 52.5° propagates into Si prism, at the interface between two different mediums, in which refractive index of Si (n_{Si}= 3.41) is greater than that of air (n≈ 1) and usual materials (~1.5). The incident wave with θ_{atr}=51° > θ_c= 26° to ensure that total internal reflection can be achieved. When the incident angle is larger than the critical angle, only the incident and the reflected waves are present. In another side of the interface, there is a wave propagating along the interface and amplitude decays exponentially. It is called an evanescent wave, its amplitude or energy density is largest at the interface and is exponentially damped into the weaker density medium with the distance away from the interface.

The energy density of evanescent wave falls off as

$$e^{-\frac{2z}{d_p}} \tag{3-1}$$

The penetration depth of the evanescent wave

$$d_p = \frac{\lambda}{2\pi\sqrt{n_1^2 \sin^2\theta - n_2^2}} \tag{3-2}$$

n_1: the refractive index of the denser medium

n_2: the refractive index of the rarer medium

θ: the incident angle at the interface ($\theta = \theta_{atr}$) in Fig.3.13)

From Eq. (3.2) the penetration depth of the evanescent wave is a function of refractive indices of two medium and incident angle at the interface. The penetrate depth is same for both of s and p polarization of the incident wave.

Moreover, the penetration depth is only defined when the incident angle is greater than the critical angle at the interface (supercritical internal reflection). If in the case of subcritical internal reflection, the penetration depth is imaginary.

The evanescent wave propagates parallel to the interface with the velocity c_e given by:

$$c_e = \frac{c}{n_1 \sin\theta} \qquad (3\text{-}3)$$

At the interface between the Si prism and the sample, THz energy leaks through the interface and penetrates into the sample (absorbing medium). The interface itself does not absorb any energy, it is likely transparent. The sample absorbs the energy and causes the evanescent wave no longer propagates parallel to the interface, now it makes an angle to the interface. The energy that evanescent wave lost is supplied by the amount of energy that THz energy leaking through the interface. That causes the totally reflected wave at the interface no long carrying all the incident energy, it now is attenuated. This wave carries information from the sample.

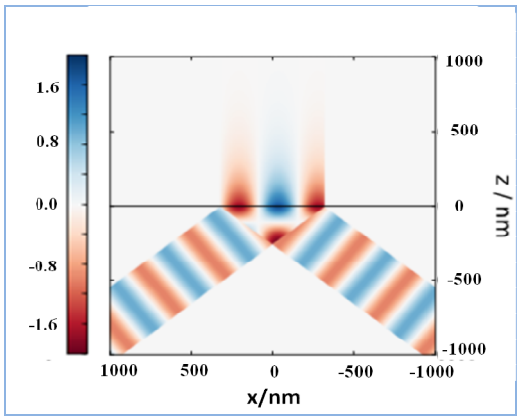

Figure 3.14: Schematic diagram represents how the energy flow in THz- ATR[92].

Figure 3.14 shows how the energy of the incident wave leaks into the other side of the interface. The electric field of the evanescent wave is related to the electric field of the incident wave by the Fresnel amplitude transmission coefficient.

3.3 Data collection and extraction optical constants of materials from experiments

3.3.1 THz time domain spectroscopy

When light travels through an absorbing medium, it is absorbed by the medium. The absorption of materials can be extracted by Beer-Lamber law.

$$A = -\log\left(\frac{I}{I_0}\right) \qquad (3\text{-}4)$$

Where: I is the light intensity passing through the sample and I_0 is the initial light intensity.

The experimental data for TRTS and THz-TDS are treated in the same way. Here, for the benefit of simplicity, the reflected and scattered lights by the sample are neglected.

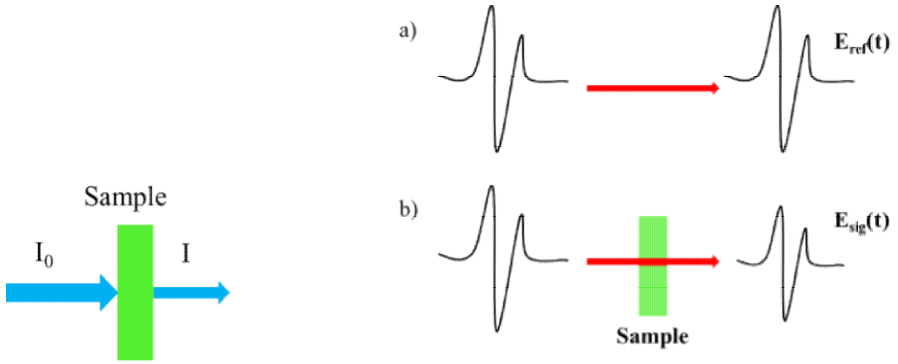

Figure 3.15: The principle of the differential time-domain measurement.

For a data collection, the reference waveform $E_{ref}(t)$ transmitted in the air and the signal waveform $E_{sig}(t)$ penetrating through the sample are recorded as a function of the time delay t, shown in Fig. 3.15 a,b.

The amplitude of $E_{sig}(t)$ is decreased due to loss of Fresnel reflection at each interface, absorption from the sample, and scattering in the medium. The signal, in addition, is delayed since the refractive index of the medium is generally greater than air.

The absorption A (optical density) of material calculated in Eq. (3-4) now is become:

$$A = -\log\left(\frac{E_{sig}(\omega)}{E_{ref}(\omega)}\right)^2 \qquad (3\text{-}5)$$

Here, $E_{ref}(\omega)$ and $E_{sig}(\omega)$ is obtained by FFT.

3.3.2 THz time domain attenuated total reflection and time-resolved attenuated total reflection spectroscopy

The optical constants of a material reflect the interaction of light with the material. In the TR-ATR measurement, the response of the material is basically described by the complex refractive index of the material which is extracted directly by the Fresnel formula. Data collection for THz-ATR and TR-ATR illustrated in Fig. 3.16 and 3.12 in section 3.3.1.

Fresnel equation for reflected wave with p- polarization:

$$\tilde{r}(\omega) = \frac{\tilde{n}_2^2(\omega)\cos\theta - {}_1\sqrt{\tilde{n}_2^2(\omega) - n_1^2\sin^2\theta}}{\tilde{n}_2^2(\omega)\cos\theta + n_1\sqrt{\tilde{n}_2^2(\omega) - n_1^2\sin^2\theta}} \qquad (3\text{-}6)$$

Where $\tilde{r}(\omega)$: complex reflectance coefficient

n_1: complex refractive index of the medium 1 (n_{air}=1)

$\tilde{n}_2(\omega)$: complex refractive index of the medium 2

θ: the incident angle at the interface of two mediums shown in Fig. 3.11.

ω: angular frequency

In THz-ATR measurement, $\mathbf{E}_{ref}(t)$ and $\mathbf{E}_{sig}(t)$ are the magnitude of complex reflectance at THz-ATR surface of reference and that of sample obtained by Fourier transform of the collected THz waveform

The complex reflectance coefficient is shown in following equation:

$$\tilde{r}(\omega) = \frac{\tilde{E}_{sig}(\omega)}{\tilde{E}_{ref}(\omega)} = \sqrt{R(\omega)}\exp\,[i\Delta\phi] \qquad (3\text{-}7)$$

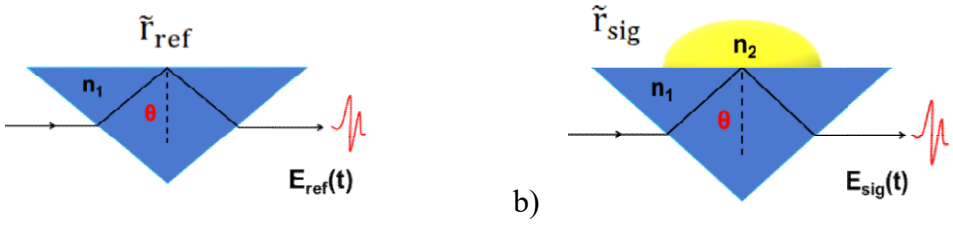

a) b)

Figure 3.16: Schematic diagrams of reference and signal measurements on a Si prim of THz-ATR.

With $\sqrt{R(\omega)}$ and $\Delta\phi$ is an attenuated reflectance and phase change comparing ϕ_{ref} and ϕ_{sig}, respectively.

$$R(\omega) = \left|\frac{E_{sig}(\omega)}{E_{ref}(\omega)}\right|^2 \qquad (3\text{-}8)$$

$$\Delta\phi = \phi_{sig}(\omega) - \phi_{ref}(\omega) \qquad (3\text{-}9)$$

Both of R(ω) and $\Delta\phi$ are obtained from FFT.

The complex reflectance coefficient is also calculated by:

$$\tilde{r}(\omega) = \frac{A\tilde{r}_{sig}(\omega)}{A\tilde{r}_{ref}(\omega)} = \frac{\tilde{r}_{sig}(\omega)}{\tilde{r}_{ref}(\omega)} = \frac{\tilde{E}_{sig}(\omega)}{\tilde{E}_{ref}(\omega)} \qquad (3\text{-}10)$$

$$\tilde{r}_{sig}(\omega) = \frac{\tilde{E}_{sig}(\omega)}{\tilde{E}_{ref}(\omega)} \tilde{r}_{ref} \quad (3\text{-}11)$$

Where, A is an added function due to equipment, $\tilde{r}_{sig}(\omega)$ and $\tilde{r}_{ref}(\omega)$ are the Fresnel reflectance coefficient at the interfaces of Si-air and Si-sample, respectively.

Fresnel reflectance coefficient $\tilde{r}_{ref}=\tilde{r}_{air}$ at the interface of Si prism - air is ($n_1=n_{Si}=3.41$, $n_2=n_{air}=1$, $\theta= 51°$):

$$\tilde{r}_{air}(\omega) = \frac{\cos\theta - n_1\sqrt{1-n_1^2\sin^2\theta}}{\cos\theta + {}_1\sqrt{1-n_1^2\sin^2\theta}} \quad (3\text{-}12)$$

$$\tilde{r}_{air} = -0.988-0.155i \quad (3\text{-}13)$$

Fresnel reflectance coefficient $\tilde{r}_{sig}$ at the interface of Si-sample

$$\tilde{r}_{sig}(\omega) = \frac{\tilde{n}_2^2\cos\theta - n_1\sqrt{\tilde{n}_2^2-n_1^2\sin^2\theta}}{\tilde{n}_2^2\cos\theta + {}_1\sqrt{\tilde{n}_2^2-n_1^2\sin^2\theta}} \quad (3\text{-}14)$$

$$\tilde{r}_{sig} = \frac{\tilde{n}_2\cos\theta - {}_1\sqrt{1-\frac{n_1^2}{\tilde{n}_2^2}sin^2\theta}}{\tilde{n}_2\cos\theta + {}_1\sqrt{1-\frac{n_1^2}{\tilde{n}_2^2}sin^2\theta}} \quad (3\text{-}15)$$

$$\tilde{n}_2(\omega) = n_2 + i\kappa \quad (3\text{-}16)$$

With n_2: the real part of refractive index

κ: the imaginary part of refractive index

Now A and B are derived as:

$$A = \left(1+\tilde{r}_{sig}\right)^2 = \left(\frac{\tilde{n}_2(\omega)\cos\theta}{\tilde{n}_2(\omega)\cos\theta + n_1\sqrt{1-\frac{n_1^2}{\tilde{n}_2^2}sin^2\theta}}\right)^2 \quad (3\text{-}17)$$

$$B = \left(1-\tilde{r}_{sig}\right)^2 = \left(\frac{-n_1\sqrt{1-\frac{n_1^2}{\tilde{n}_2^2}sin^2\theta}}{\tilde{n}_2(\omega)\cos\theta + n_1\sqrt{1-\frac{n_1^2}{\tilde{n}_2^2}sin^2\theta}}\right)^2 \quad (3\text{-}18)$$

$$\frac{A}{B} = \frac{\tilde{n}_2^2(\omega)\cos^2\theta}{n_1^2\left(1-\frac{n_1^2}{\tilde{n}_2^2}sin^2\theta\right)} \quad (3\text{-}19)$$

We are going to solve Eq (3-19) to find $\tilde{n}_2(\omega)$

$$\tilde{n}_2^4 - \frac{A}{B}\frac{n_1^2\tilde{n}_2^2}{cos^2\theta} + \frac{A}{B}n_1^4 tan^2\theta = 0 \qquad (3\text{-}20)$$

$$\tilde{n}_2^2(\omega) = \frac{A}{2B}\frac{n_1^2}{cos^2\theta} \pm \frac{1}{2}n_1^2\sqrt{\frac{A^2}{B^2}\frac{1}{cos^4\theta} - \frac{4A}{B}\tan^2\theta} \qquad (3\text{-}21)$$

The complex refractive index is obtained from eq (3-20), the sign of eq (3-21) is chosen so that n_2 and κ are real number

The complex dielectric constant is related to the complex refractive index by:

$$\tilde{n}_2(\omega) = \sqrt{\tilde{\varepsilon}_2(\omega)} \qquad (3\text{-}22)$$

The absorption coefficient is calculated by: $\alpha = \frac{2\kappa\omega}{c}$ (Hz.m^{-1}) (3-23)

3. 4 Evaluation of THz and visible pump beam spot size

3.4.1 The knife edge method:

The knife-edge technique, which is widely used due to its simplicity and possibility to apply for a wide range of wavelengths, was used to measure the waist of THz beam and visibly excited pump beam at the position that the sample is located. In this method, the intensity of the beam is detected as the function of the position of the knife edge on a motorized stage. A step-like intensity shape as a function of the position of the knife edge appears. The recorded intensity can be explained as an integral of Gaussian function.

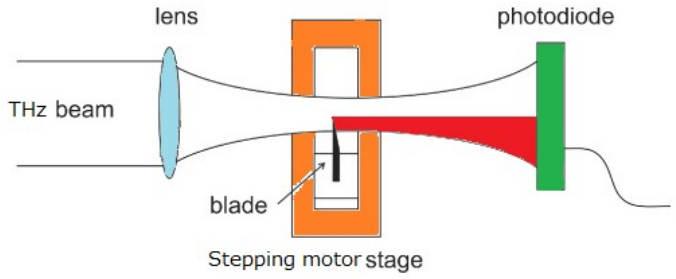

Figure 3.17: Schematic diagram of knife edge technique to measure THz beam waist. The red area shows the region cut by the knife edge.

Figure 3.17 illustrates the knife-edge experiment, this method requires a sharp razor blade which is placed on the stepping motor stage with total length 2 mm, the power of the beam is recorded by a photodiode for visible light.

A beam propagating in z direction with Gaussian intensity is followed by:

$$I(x,y) = I_0 \exp\left[-2\frac{(x-x_0)^2}{\omega_x^2}\right] \exp\left[-2\frac{(y-y_0)^2}{\omega_y^2}\right] \qquad (3\text{-}23)$$

Where :

I_0: peak intensity at the center of the beam

x_0 and y_0 are peak position in x and y Cartesian coordinates

ω_x and ω_y are the beam radii at the position where the intensity is equal $1/e^2$ times of I_0

Now, the total power of the beam is

$$P = I_0 \int_{-\infty}^{\infty} \exp\left\{-2\frac{(x-x_0)^2}{\omega_x^2}\right\} dx \int_{-\infty}^{\infty} \exp\left\{-2\frac{(y-y_0)^2}{\omega_y^2}\right\} dy = \frac{\pi}{2} I_0 \omega_x \omega_y \qquad (3\text{-}24)$$

Assume that the knife edge is moving along x direction, thus the transmitted power is:

$$P(X) = P - I_0 \int_{-\infty}^{X} \exp\left\{-2\frac{(x-x_0)^2}{\omega_x^2}\right\} dx \int_{-\infty}^{\infty} \exp\left\{-2\frac{(y-y_0)^2}{\omega_y^2}\right\} dy$$

$$= P - \sqrt{\frac{\pi}{2}} I_0 \omega_y \left[\int_{-\infty}^{0} \exp\left\{-2\frac{(x-x_0)^2}{\omega_x^2}\right\} dx + \int_{0}^{X} \exp\left\{-2\frac{(x-x_0)^2}{\omega_x^2}\right\} dx\right]$$

$$= P - \sqrt{\frac{\pi}{2}} I_0 \omega_y \left[\sqrt{\frac{\pi}{8}} \omega_x + \int_{0}^{X} \exp\left\{-2\frac{(x-x_0)^2}{\omega_x^2}\right\} dx\right]$$

$$= \frac{P}{2} - \sqrt{\frac{\pi}{2}} I_0 \omega_y \int_{0}^{X} \exp\left\{-2\frac{(x-x_0)^2}{\omega_x^2}\right\} dx \qquad (3\text{-}25)$$

Substitute $u = \sqrt{2}\dfrac{x-x_0}{\omega_x}$ so that $du = \dfrac{\sqrt{2}}{\omega_x} dx$ to change the limits of the integral, that leads to:

$$P(X) = \frac{P}{2} - \frac{\pi}{4} I_0 \omega_y \omega_x \frac{2}{\sqrt{\pi}} \int_{-\sqrt{2}\frac{x_0}{\omega_x}}^{\sqrt{2}\left(\frac{X-x_0}{\omega_x}\right)} e^{-u^2} du \qquad (3\text{-}26)$$

Finally, $$P(X) = P_0 + \frac{P}{2}\left(1 - \operatorname{erf}\left(\sqrt{2}\left(\frac{X-x_0}{\omega_x}\right)\right)\right) \qquad (3\text{-}27)$$

Here, P_0 is a background power or power shift, P is a maximal power, x_0 is a position shift with the half of real power, and erf is a standard error function. Eq.(3-26) can be ± erf, it

depends on the moving direction of the knife. When the knife translates in the positive direction, the equation will be + erf, and – erf for the negative direction.

Equation (3-26) is used to fit experimental data. After fitting the peak position, the beam radius at the position where the intensity decrease $1/e^2$ and the power of the beam will be determined. With all of parameters we can build Gaussian curve as the equation below:

$$G(x) = \frac{P}{2}\exp\left(-\frac{2(x-x_0)^2}{\omega_x^2}\right) \quad (3\text{-}28)$$

The full width at half maximum (FHWM) is related to ω_x as the following function:

$$FHWM = \sqrt{2\ln 2}\,\omega_x = 1.1773\,\omega_x \quad (3\text{-}29)$$

3.4.2 Experimental results

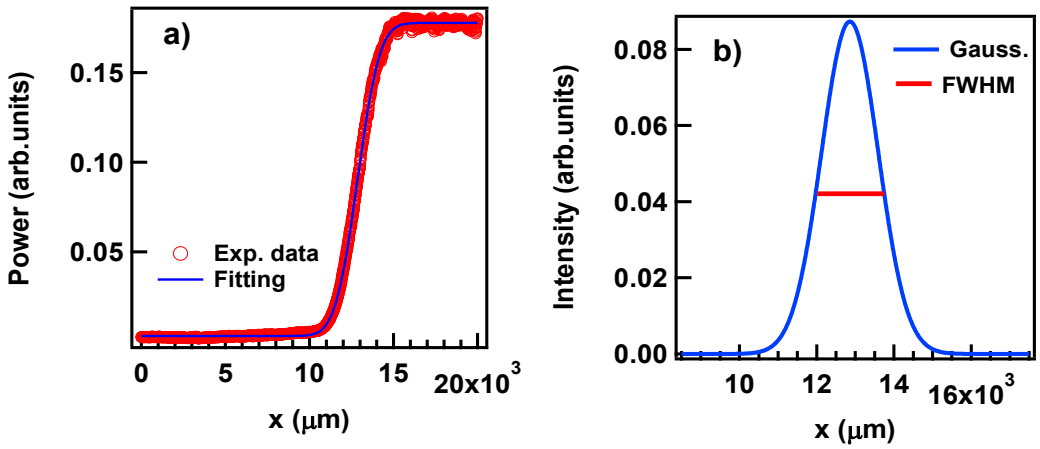

Figure 3.18: a) (Opened circle) the experimental data of measurement THz beam spot size and the fitting of the experimental data using the Eq. (3-27). b) The Gaussian shape of the THz beam is built from the data gotten from the fitting.

In order to measure the THz and visible pump beam waists, the razor blade is translated perpendicular to the propagation of the beam direction. The total transmitted power is collected as a function of the position of the knife. The blade is mounted on a translational stage that moves by a 10-μm step. The intensity of the translated beam was recorded by Si Bias photodiode for visible light.

The data set was fitted with Eq.(3-27) by using Igor program, after fitting we get all parameters for the THz beam: x_0=12860 μm, ω_x= 1470 μm, P =0.174 and P_0= 0.09. The result of fitting is shown in Fig. 3.18 a). The Gaussian shape of THz beam is graphed from all data of the fitting with FHWM= 1730 μm, displayed in Fig. 3.18 b).

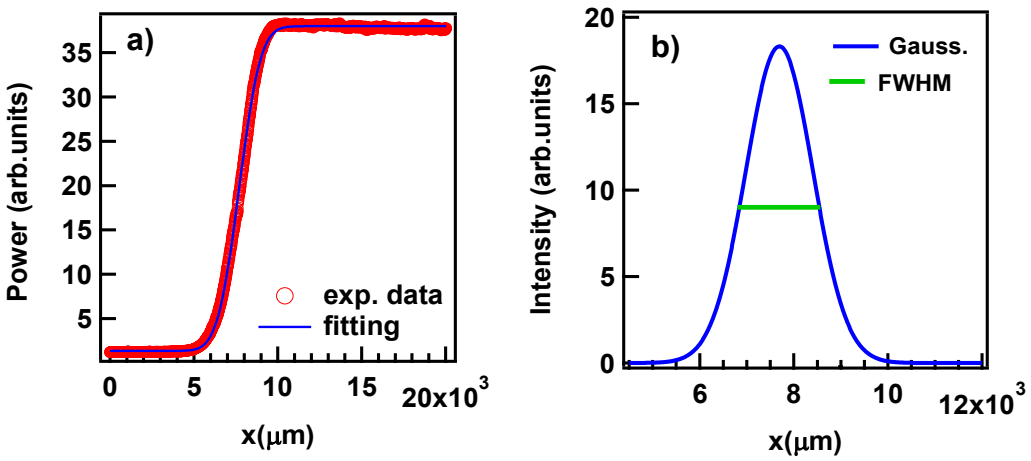

Figure 3.19: a) (Opened circle) the experimental data of measurement the pump beam spot size and the fitting of the experimental data using the Eq. (3-27). b) The Gaussian shape of pump beam is built from the data gotten from the fitting.

Fig. 3.19 a) shows the experimental data of visible pump beam spot size and fitting curve with parameters x_0=7693 μm, ω_x= 1426 μm, P =36.6 and P_0= 19.7, respectively. The Gaussian shape of the pump beam with FWHM= 1679 μm is shown in Fig. 3.19 b). We can easily adjust the spot size of the pump beam by moving the lens focusing the pump beam.

3.5 Sample preparation

$Re(CO)_2(bpy)\{P(OEt)_3\}_2](PF_6)$ powder was synthesized by Ishitani Lab. using the same method as previous reports[29], by photolysis (>360 nm long-pass filter) of (2,2'-bipyridyl) tricarbonyl rhenium trifluoromethanesulfonate in MeCN in the presence of $P(OEt)_3$. Reaction with NH_4PF_6 in MeOH yielded the title salt, which was subjected to column chromatography on silica with $MeCN/CH_2Cl_2$ (1:5 v/v) as eluant.

- Sample preparation for measurement:

THz-TDS: the sample is sandwiched between two windows, shown in Fig. 3.20.

THz-*ATR and TR-ATR*: $[Re(CO)_2(bpy)\{P(OEt)_3\}_2](PF_6)$ powder is mixed into TEOA solution. The solution is placed on the Si surface where the pump beam and THz beam overlap.

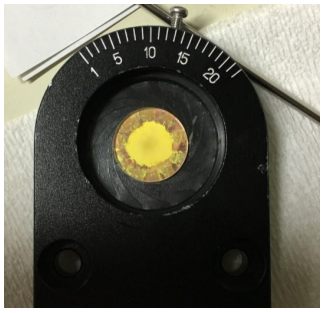

Figure 3.20: a) The sample powder is sandwiched between two windows and kept by the pin hole.

Conclusion

We have constructed the experimental setup of THz-TDS as well as THz-ATR, and TR-ATR in detail. We have also shown the obtained THz spectra measured by our spectrometers. The THz spectra generated and detected by ZnTe has the bandwidth of 0.3 to 2.5 THz with the highest intensity and best S/N ratio (~7 order of magnitude in maximum) in comparison to GaP and air plasma.

Besides that, we have discussed data collection and extraction of optical constants from experimentally obtained data as well as show an evaluation method of the THz and pump beams' waist size by a knife edge method.

Chapter IV

Absorption spectra of $[Re(CO)_2(bpy)\{P(OEt)_3\}_2](PF_6)$ complex

In this chapter, the absorption spectra of a photocatalyst $[Re(CO)_2(bpy)\{P(OEt)_3\}_2](PF_6)$ in TEOA solvent and in a solid form measured by using THz-ATR spectroscopy and THz-TDS, respectively, are reported. Some peaks are observed both in the solid form and in the TEOA solvent, but some new peaks appear only in the solvent. The origin of these absorption peaks is identified by comparing the vibrational modes existing in TEOA solvent and in the solid form.

$[Re(CO)_2(bpy)\{P(OEt)_3\}_2](PF_6)$ complex (Re complex) is the crucial photocatalyst for reduction of CO_2 with high quantum yield. Unlike other types of the photocatalysts, the complex itself acts as the catalyst and photosensitizer without combining to another catalyst. The excited state kinetics and structural spectra of these complexes in the THz region have not been reported. THz spectroscopy allows us to access intermolecular interactions of solute-solvent molecules, which is critical for understanding molecular dynamics in the photocatalytic system.

To identify the origin of vibrational modes of Re complex in TEOA solvent, the combination of THz-TDS and THz-ATR were used to study absorption spectra in both of media.

Due to the interest in absorptions in the wide range THz, the absorption spectra of Re complex were measured by the transmittance technique of THz-TDS in the range of 0.3 to 7 THz. Because of the low S/N ratio from 3 THz, an air plasma method is applied to generate the intense THz radiation. However, absorption spectrum of Re complex powder has a primary absorption structure below the frequency of 2.5 THz. Due to the main interested area of this study from 0.3 to 2.5 THz, THz radiation in this region is generated and detected by ZnTe crystals to acquire higher S/N ratio than using GaP crystal or air plasma generation.

THz-ATR is a good tool to measure Re complex in high absorbing solvent in the THz region (such as TEOA solvent). Otherwise, THz-ATRis not appropriate for conducting absorption of Re complex in solid form because this material cannot be pressed (for powder studied by THz-ATR spectroscopy, the sample is pressed or shaped into a tablet). Then we used the transmittance technique of THz –TDS to study the absorption of Re complex in solid form.

All of experimental data are discussed in the following sections.

4.1 Absorption spectra of $[Re(CO)_2(bpy)\{P(OEt)_3\}_2](PF_6)$ complex in solid form studied by THz-TDS

In this section, the absorption spectrum of Re complex in solid form is investigated by THz-TDS in the region of 0.3 to 7 THz and 0.3 to 2.5 THz. As we mentioned in the experimental method (chapter 3), THz-TDS measurement, the Re complex powder is sandwiched between two windows (Z-cut quartz and Cu filter). Hence, we have to measure the absorption of the windows.

4.1.1 THz-TDS spectra in the range of 0.3 - 7 THz

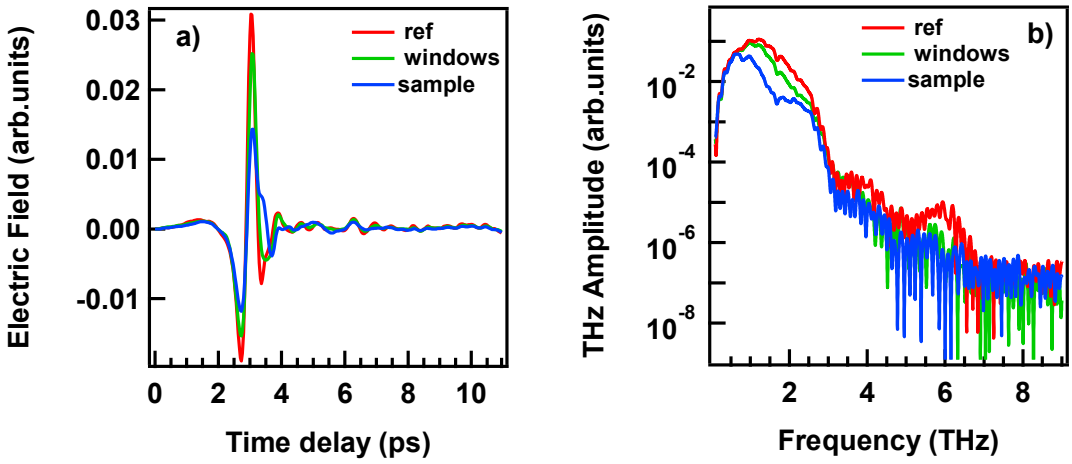

Figure 4.1: a) THz waveforms of referrence “ref”, “windows” and “sample” (see the explanation in text) measured by transmission of THz-TDS. b) Corresponding spectra from 0.3 to 7 THz obtained by FFT. THz radiation generated and detected by GaP crystals.

The THz waveforms of reference “ref” (without sample), two windows “windows”, which are used to sandwich Re complex powder, and Re complex powder + windows “sample” were obtained by THz-TDS (its setup is presented in section 3.1 of chapter III) and corresponding THz spectra in the range of 0.3 to 7 THz, shown in Fig. 4.1. The color denotes

for both of THz waveform and its corresponding spectrum after FFT following by: ref as red, sample as blue, and windows as green.

To acquire the absorption spectrum of Re complex in solid form, we separately measure the absorption of "windows" and that of "windows + Re complex powder". The absorption intensity is described by optical density (OD), in which the relation of OD to the transmission intensity is described by Eqs. 3.4 and 3.5 in section 3.4 of chapter III. Hereafter, OD spectrum is described by absorption spectrum.

The OD of Re complex powder "sample" can be derived from the subtraction of OD of "windows" from OD of "windows+Re complex powder".

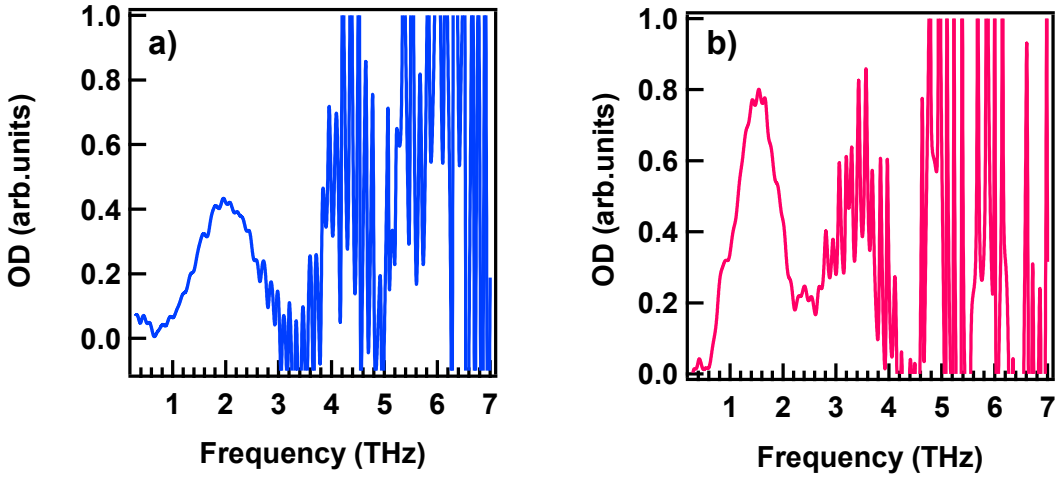

Figure 4.2: a) Absorption spectrum of "windows" measured by THz-TDS in the range from 0.3 to 7 THz. b) Absorption spectrum of Re complex powder "sample" measured by THz-TDS in the range from 0.3 to 7 THz.

The absorption spectra of "windows" and "sample" in the region from 0.3 to 7 THz are displayed in Fig. 4.2. Figure 4.2 a) shows a broadband absorption of "windows" starts at 1 THz and the absorption has a peak at 2 THz. In the frequency range above 3 THz, the noise level is higher than the THz intensity. Furthermore, the absorption of "sample" mainly appears in the frequency range below 2.5 THz, as shown in Fig. 4.6 b). Thus the absorption spectrum of "sample" in Fig. 4.2 b) is expanded in the range from 0.3 to 2.5 THz, as shown in Fig. 4.3.

These broadband absorptions in Fig. 4.3 are assigned to fit by Gaussian functions because peak positions of each molecules are fluctuated and the distribution should originate from the statistical probability even though the shape of an absorption peak might be

Lorentian. Therefore, it can be assumpted as a Gaussian fuction. Each Gaussian function is following by:

$$G(x) = A * \exp\left(-\frac{2(x-x_0)^2}{\omega_x^2}\right) \quad (4.1)$$

Here, x_0: peak position

$\omega_x = \sigma\sqrt{2}$: σ variation (is a measure that is used to quantify the amount of variation or dispersion of a set of data values), and A: peak intensity or optical density.

The peak width Γ (full width at half maximum (FHWM)) is related to ω_x as the following function:

$$\Gamma = \sqrt{2\ln 2}\ \omega_x = 1.1773\ \omega_x \quad (4.2)$$

The absorption spectrum of Re complex powder is fitted by three Gaussian functions corresponding to three peaks at 1, 1.5 and 2 THz, shown in Fig. 4.3. Tab. 4.1 lists all of the parameters of each absorption shown in Fig 4.3.

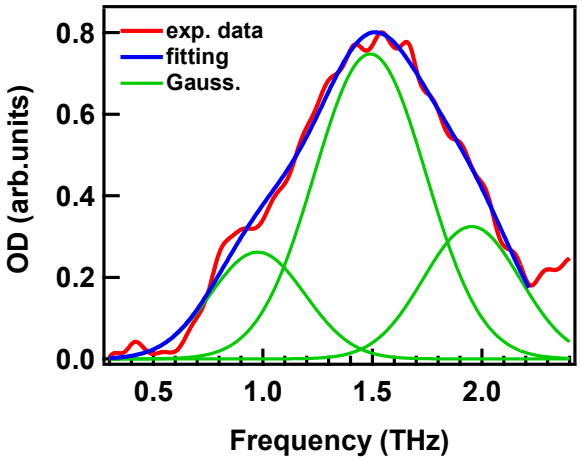

Figure 4.3: The expansion of the absorption spectrum in Fig. 4.2 b in the region of 0.3 to 2.5 THz. Gaussian analysis of the absorption spectrum of Re complex powder is shown in blue, individual Gaussian peak in green, and the experimental data in red.

Peak parameters	Position (THz)	Intensity (OD)	FHWM (THz)
1-THz peak	0.98 ± 0.03	0.26 ± 0.04	0.50 ± 0.02
1.5-THz peak	1.49 ± 0.02	0.75 ± 0.05	0.60 ± 0.06
2-THz peak	1.95 ± 0.05	0.32 ± 0.07	0.52 ± 0.04

Table 4.1: Obtained parameters of three absorptions of Re complex in solid form by using a non-linear least square method using three Gaussian functions.

4.1.2 THz-TDS spectra in the range of 0.3 - 2.5 THz

In this section, we use THz-TDS, in which THz radiation is generated and detected by ZnTe crystals, with the obtained bandwidth from 0.3 to 2.5 THz (the spectroscopy setup is presented in section 3.1) to confirm the absorption spectrum of Re complex powder due to the highest S/N ratio in comparison with THz radiations generated by GaP or air plasma.

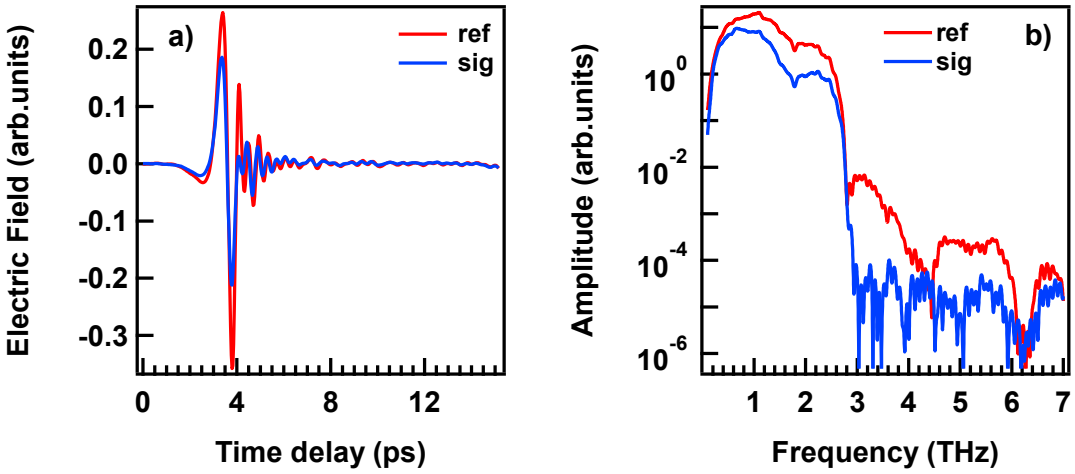

Figure 4.4: a) THz waveforms of the reference "ref" (without sample) and the Re complex powder+windows "sig" measured by THz-TDS. b) Corresponding THz spectra in the range of 0.3-2.5 THz obtained by FFT.

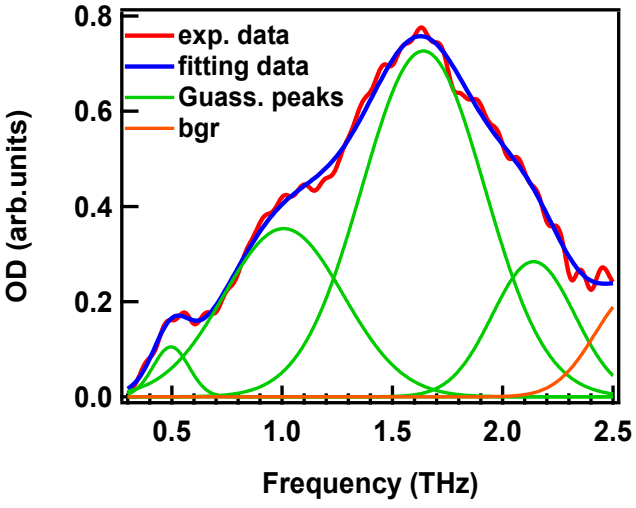

Figure 4.5: Gaussian fitting results of the absorption spectrum of Re complex in solid form measured in the range from 0.3 to 2.5 THz. The experimental data is shown in red, individual Gaussian functions in green, their sum in blue, and the background in orange.

Figure 4.4 shows the THz waveforms of reference "ref" and sample (Re complex powder+windows) "sig" measured by THz-TDS and the corresponding THz spectra obtained by FFT in the frequency range of 0.3-2.5 THz. In Figure 4.5, the absorption spectrum of Re complex powder (the absorption from windows have already removed) is displayed in red, individual Gaussian functions in green, the background (Gaussian peak which is fitted parameters (shown in Tab. 4.2, is determined by the absorption spectrum in Fig. 4.2b) in orange, and their sum in blue.

Absorption spectrum and fitted Gaussian functions corresponding to four vibrational modes at 0.5, 1.1, 1.6, and 2.2 THz are shown in Fig. 4.5. Table 4.2 shows all of the parameter of individual vibrational modes.

Peak parameter	Position (THz)	Intensity (OD)	FWHM (THz)
0.5-THz peak	0.500 ± 0.003	0.100 ± 0.004	0.130 ± 0.005
1-THz peak	1.000± 0.009	0.35 ± 0.01	0.45 ± 0.01
1.6-THz peak	1.640± 0.007	0.730 ± 0.014	0.460 ± 0.018
2.2-THz peak	2.140 ± 0.015	0.28 ± 0.02	0.310 ± 0.009
Background	2.6	0.22	0.3

Table 4.2: Parameters of four absorption peaks of Re complex solid form and the background obtained by a nonlinear least square method using four Gaussian functions and a constant background.

Comparing the spectrum in Fig. 4.5 with that in Fig. 4.3, the spectra shape is similar with three absorption found around 1, 1.6 and 2 THz. However, a peak at 0.5 THz only appears in Fig. 4.5 because of the lower S/N ratio of THz spectrum in low frequency range (0.3-0.7 THz) in Fig. 4.3 (THz pulse generated by GaP).

4.2 Vibrational modes of $[Re(CO)_2(bpy)\{P(OEt)_3\}_2](PF_6)$ in TEOA studied by THz-ATR

To identify the origin of the vibration peaks appearing in absorption spectra such as the vibrations only in TEOA molecules or between Re complex and TEOA molecules, we

measured the absorption spectra of pure TEOA solvent and the mixed Re complex with TEOA solvent.

Figure 4.6 shows THz-ATR waveforms of the reference "ref" and pure TEOA solvent, and the corresponding THz spectra obtained by FFT in the frequency range of 0.3 to 2.5 THz. The absorption spectrum of TEOA solvent shown in Fig. 4.7 has two strong, sharp absorptions at 0.4 and 0.7 THz which are assigned to be intermolecular vibrational modes between TEOA molecules. From 0.9 to 2.4 THz there is no strong absorption.

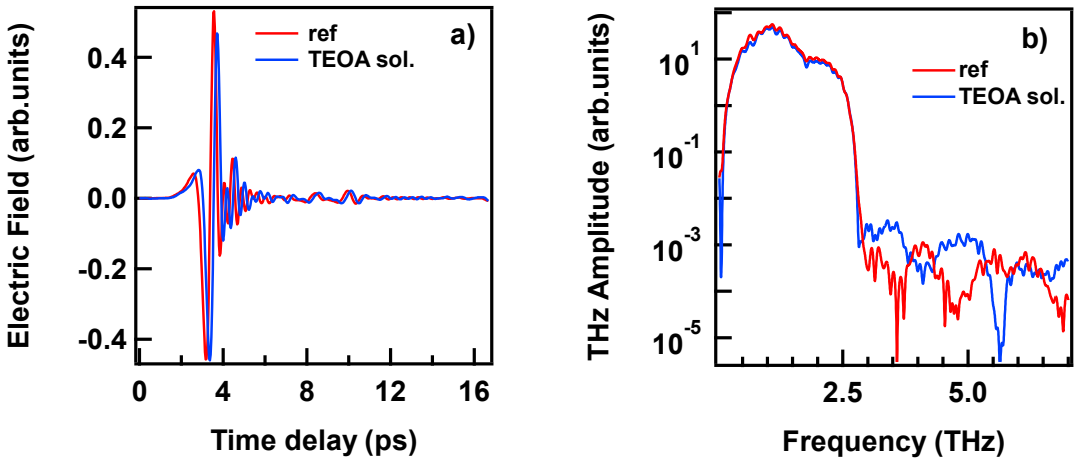

Figure 4.6: a) THz waveforms of the reference "ref" (without sample) and pure TEOA solvent by THz-ATR are shown in red and blue, respectively. b) Corresponding THz spectra from 0.3 to 2.5 THz obtained by FFT.

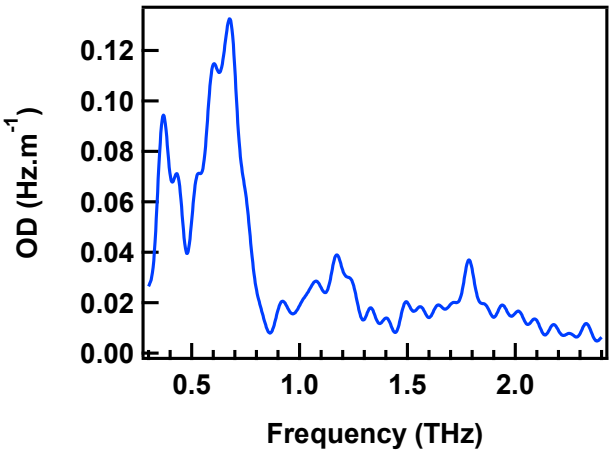

Figure 4.7: Absorption spectrum of TEOA solvent measured by ATR in the range of 0.3 to 2.5 THz.

Figure 4.8 shows the experimental data of the reference "ref" (without sample) and $[Re(CO)_2(bpy)\{P(OEt)_3\}_2](PF_6)$ in TEOA solvent "sample" measured by THz-ATR and the

corresponding THz spectra obtained by FFT in the frequency range of 0.3 to 2.5 THz. Figure 4.9 displays the absorption spectrum of Re complex in TEOA solvent, the absorption curve is shown in red, fitting data in blue, and all Gaussian fitting curves in green. The THz-ATR spectrum indicates the vibrational structure of Re complex in TEOA with three vibrational modes found at 1 THz, 1.35 THz and 1.7 THz.

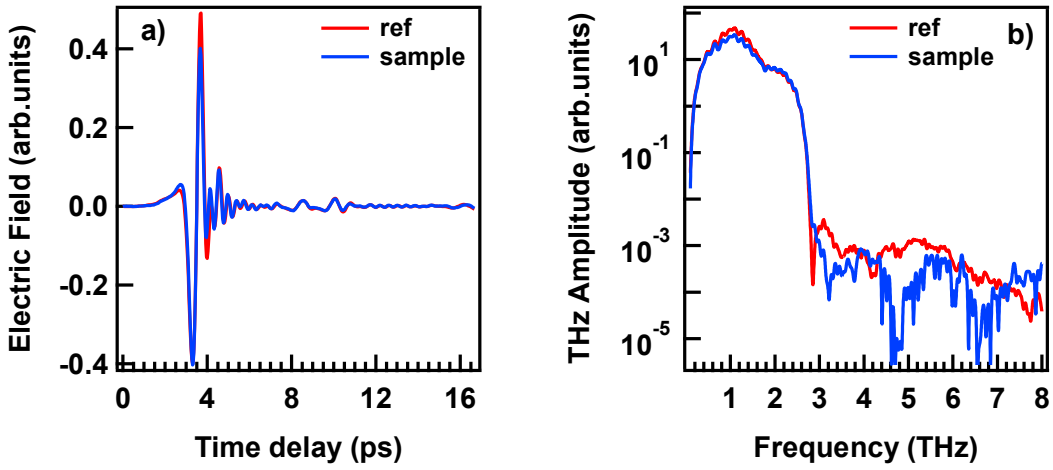

Figure 4.8: a) THz waveforms measured by THz-ATR spectroscopy: the reference ref measured in air and sample signal "sample" measured through the sample medium are shown in red and blue, respectively. b) Corresponding THz spectra from 0.3 to 2.5 THz obtained by FFT method.

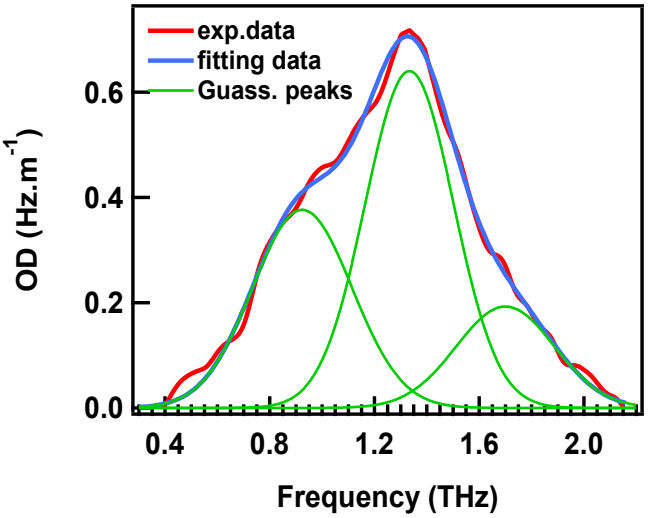

Figure 4.9: Absorption spectrum of Re complex in TEOA measured in the region from 0.4 to 2.5 THz and the fitting result by using a nonlinear least square method with three Gaussian functions. The experimental data is shown in red, individual Gaussian functions in green, and their sums in blue.

Among these vibrational modes, the 1.35-THz is predominant and the 1.7-THz is the weakest in the intensity. These peaks have the similar width of about 0.4 THz. Table 4.3 shows peak parameters of all peaks obtained by Gaussian fitting. The candidates for the origin of these vibrations in the THz region are low energy intramolecular vibrations or intermolecular vibrations.

Peak parameters	Position (THz)	Intensity (OD)	FWHM (THz)
1-THz peak	0.95 ± 0.01	0.35 ± 0.01	0.41 ± 0.01
1.35-THz peak	1.34 ± 0.005	0.63 ± 0.02	0.40 ± 0.02
1.7-THz peak	1.70 ± 0.04	0.14 ± 0.02	0.40 ± 0.04

Table 4.3: Parameters of three absorptions of Re complex in TEOA solvent obtained by Gaussian fitting.

Comparing the absorption spectrum in solvent shown in Fig. 4.9 with that of powder shown in Fig. 4.7, we can know that absorption peaks at 0.4 and 0.7 THz do not appear in solvent (Fig. 4.9). Therefore, all of the absorption peaks in Fig. 4.9 do not consist the mutual intermolecular interaction of in TEOA molecules.

In order to identify the origin of these vibrational modes, we are going to compare the ground state absorption spectrum of $[Re(CO)_2(bpy)\{P(OEt)_3\}_2](PF_6)$ in TEOA with that of in powder form. It should be noted that "ground state" shown in this thesis means the state without photo-excitation.

4.3 Origin of vibrational modes of $[Re(CO)_2(bpy)\{P(OEt)_3\}_2](PF_6)$ in TEOA and in solid form

To identify the origin of vibrational modes of Re complex in TEOA solvent and in powder form, the comparison between their absorption spectra is discussed.

Figures 4.10 (a), (b) (same as Figs. 4.5 and 4.9, respectively) show absorption spectra of Re complex in powder and in TEOA solvent obtained by THz-TDS and THz-ATR at room temperature, respectively. These broadband absorptions were fitted by Gaussian functions, as shown in Eq (4.1) and discussed above. These spectra indicate the change of vibrational structures of the powder material from those in the solution in the THz region.

The absorption spectrum of Re complex powder displays four broad absorption peaks at 0.5, 1, 1.68 and 2.2 THz. On the other hand, the absorption spectrum of Re complex in TEOA solvent shows three absorption peaks at 1, 1.35 and 1.7 THz and the peak at 1.35 THz is dominant. Interestingly, when Re complex powder dissolves in TEOA, the presence of TEOA molecules causes the emergence of the 1.35-THz peak, the significant decrease of the 1.7-THz peak, and the dissipation of the 0.5-, 2.2-THz peaks. However, the 1-THz peak remains in both media suggesting no effect of the solvent to this absorption.

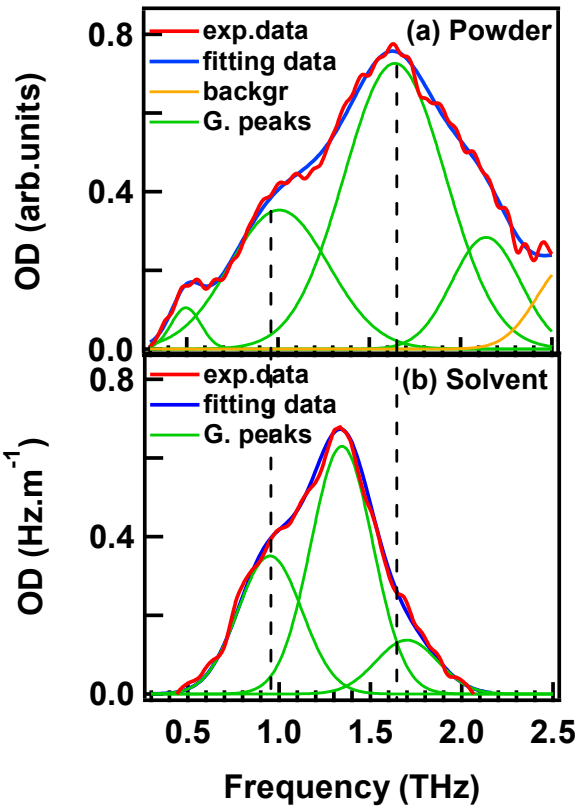

Figure 4.10: Absorption spectrum of Re complex in powder form (a) and in TEOA (b) in the frequency range from 0.3 to 2.5 THz. The experimental data is shown in red color, individual Gaussian in green, and their sums in blue. These spectra are the same as Figs. 4.5 and 4.9.

The origin of the vibrational modes of Re complex can be determined by the difference between the absorption spectra in TEOA solvent and solid form shown in Fig. 4.10. $[Re(CO)_2(bpy)\{P(OEt)_3\}_2]^+(PF_6)^-$ consists of the combination of one cation $[Re(CO)_2(bpy)\{P(OEt)_3\}_2]^+$ and one anion $(PF_6)^-$ and in the present of TEOA solvent, TEOA molecules diffuse into the complex and the anion $(PF_6)^-$ becomes detached from the parent molecule. In TEOA solvent, the nearest neighbor molecules of cation $[Re(CO)_2(bpy)\{P(OEt)_3\}_2]^+$ change from PF_6^- to TEOA in solvent.

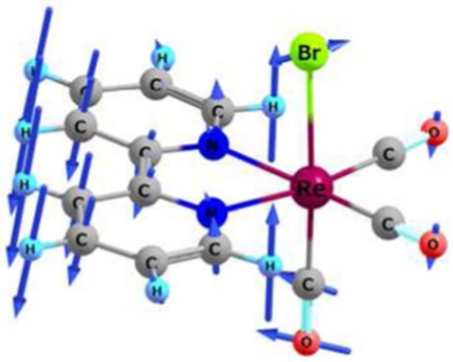

Figure 4.11: Theoretically expected normal vibrational modes of $[Re(Br)(CO)_3(bpy)]$ complex at the wavenumber of 43 cm^{-1} (1.3 THz) [93].

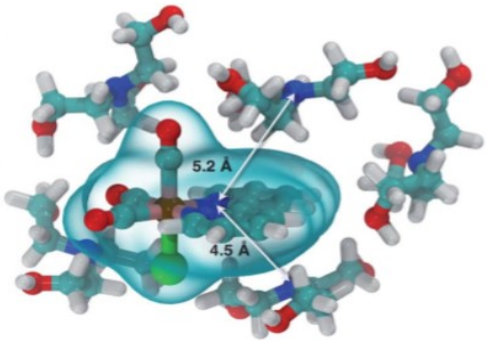

Figure 4.12: Schematic figure[36] of $[Re(bpy)(CO)_3Cl]$ with five TEOA molecules. The donor–acceptor distance is roughly 5 Å.

The vibrational mode at 1 THz is still observed and remains the high absorption intensity in both of mediums. This suggests that the origin of the 1-THz peak is the intramolecular vibration mode of Re complex ion, which is not affected by the existence of the solvent. Harabuchi et al. reported their vibrational analysis that the vibration mode related to bpy on $[Re(Br)(CO)_3(bpy)]$ complex exists at 43 cm^{-1} (1.3 THz)[93], which is same order with our study (1 THz ≈ 33 cm^{-1}), as shown in Fig.4.11.

The disappearance of the 0.5-, 2.2-THz peaks as well as the significant reduction of the 1.7-THz peak can be explained by the change of the neighbor molecule of Re cation from PF_6^- to TEOA in TEOA solvent. As a result, the 0.5-, 1.7- and 2.2-THz peaks originate from the intermolecular interaction of cation $[Re(CO)_2(bpy)\{P(OEt)_3\}_2]^+$ and anion $(PF_6)^-$.

The 1.35-THz peak only emerges in the TEOA solvent, this clearly implies that 1.35-THz peak originates from the intermolecular vibrational mode between cation $[Re(CO)_2(bpy)\{P(OEt)_3\}_2]^+$ and TEOA solvent molecules as explained in Fig. 4.12.

4.4 Absorption spectrum of [Re(CO)$_3$(dmb)Br] complex in solid form studied by THz-TDS

Herein, we report the absorption spectrum of [Re(CO)$_3$(dmb)Br] complex powder, which is a relative sample to [Re(CO)$_2$(bpy){P(OEt)$_3$}$_2$]PF$_6$, in the frequency range of 0.3 - 7 THz mearsured by the THz-TDS.

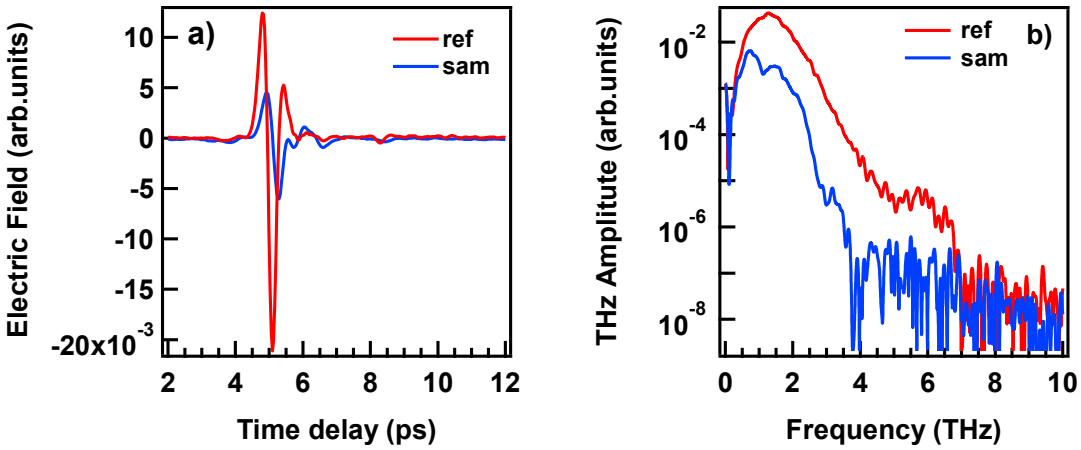

Figure 4.13: a) THz waveforms of the reference "ref" and the [Re(CO)$_3$(dmb)Br] complex in solid form "sam" measured by THz-TDS in the frequency range of 0.3 to 7 THz. b) Corresponding THz spectra obtained by FFT.

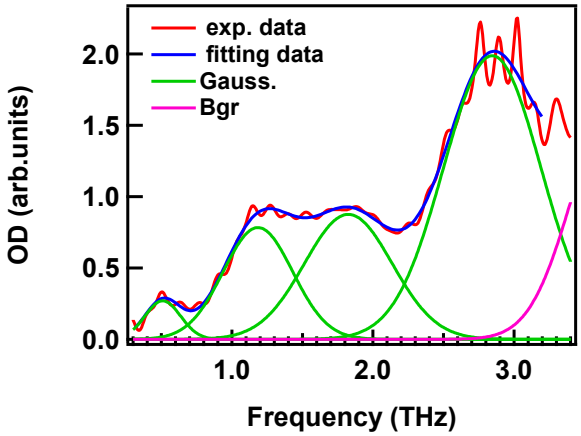

Figure 4.14: Absorption spectrum of [Re(CO)$_3$(dmb)Br] complex in solid form in the frequency range from 0.3 to 7 THz and the fitting results. The experimental data is shown in red, individual Gaussian functions in green, the background (Gaussian peak) in magenta, and the sum of fitted functions in blue.

THz waveforms of reference "ref" in air and sample + windows "sam" obtained by THz-TDS and their corresponding THz spectra after FFT in the frequency range of 0.3 - 7 THz are shown in Fig. 4.13. The collecting, extracting data and preparing sample for

experiment were performed as same as THz-TDS measurement of $[Re(CO)_2(bpy)\{P(OEt)_3\}_2]PF_6$ above. The spectrum was measured by THz-TDS, in which THz radiation generated and detected by GaP crystals.

The absorption spectrum has four peaks at 0.5, 1.2, 1.8, and 2.8 THz, as shown in Fig. 4.14. These peaks and the background are fitted by Gaussian functions described in Eq (4.1) and the parameters of all of vibrational modes are shown in Table 4.4. The background was identified by a small peak appeared at 3.7 THz (the spectrum in the range of 0.3 to 7 THz is not shown here).

The peak at 0.5 THz can not identify its orgin because we do not have enough information. To reveal the origin, we need more experiment or do more calculation.

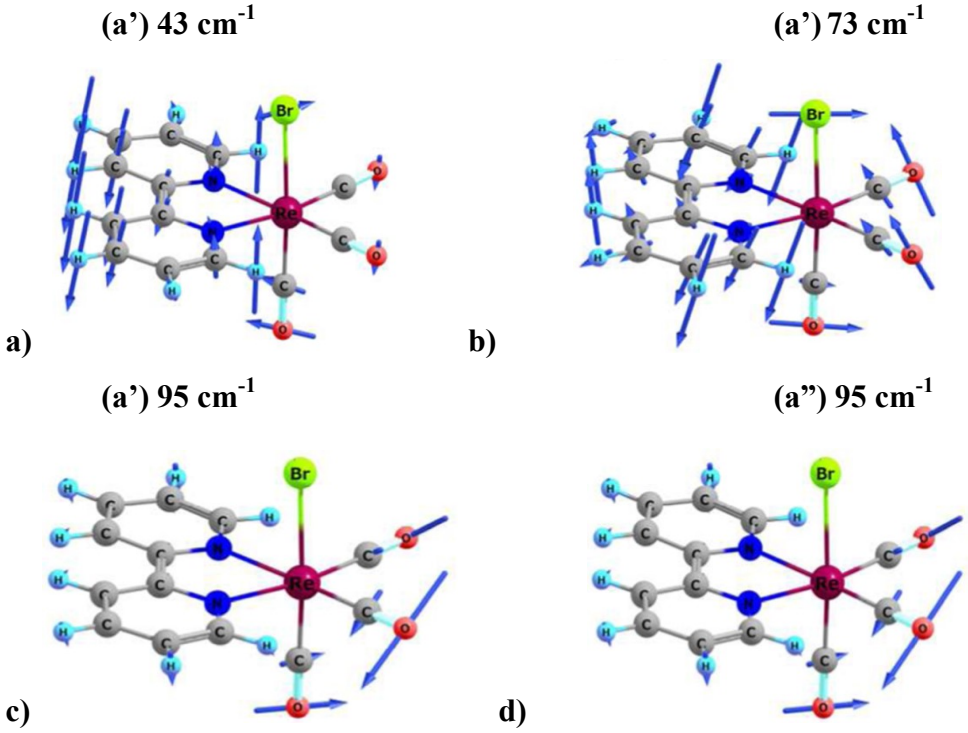

Figure 4.15: Normal vibrational modes of $[Re(Br)(CO)_3(bpy)]$ complex. (a'), (a"): totally and non-totally symmetric normal modes. (a"): the normal mode at 95 cm^{-1} that is degenerate with the relevant (a') modes is also shown.

These vibrational modes at 1.2, 1.8, and 2.8 THz have been already assigned as the intramolecular vibrations of $[Re(CO)_3(dmb)Br]$ complex by Y. Harabuchi et al.[93] as shown in the schematic figures in Fig. 4.15. They have reported that normal vibrational modes of $[Re(Br)(CO)_3(bpy)]$ complex exist at the wavenumbers of 43, 73, and 95 cm^{-1}, which are

similar to our observations of 40 cm^{-1} (1.2 THz), 61 cm^{-1} (2 THz), and 93 cm^{-1} (2.8 THz), respectively.

Particularly, the peaks at 1.2 THz and 1.8 THz have been assigned to contribute by the vibration of dmb ligand and the displacement of hydrogen atoms inside dmb ligand and other atoms, which are indicated with arrows, as illustrated in Figs. 4.15 a), b), respectively. Meanwhile, the peak at 2.8 THz is related to the vibration of pure carbonyl, as shown in Figs. 4.15 c), d).

Peak parameters	Position (THz)	Intensity (OD)	FWHM (THz)
0.5-THz	0.51 ± 0.01	0.270 ± 0.017	0.30 ± 0.03
1.2-THz	1.18 ± 0.02	0.78 ±0.05	0.58 ± 0.03
1.8-THz	1.82 ± 0.02	0.88 ± 0.02	0.73 ± 0.06
2.8-THz	2.85 ±0.01	1.99 ± 0.01	0.81 ± 0.02
Background	3.7	1.6	0.7

Table 4.4: Obtained parameters of four absorptions of Re complex solid form and the background using a nonlinear least square method with five Gaussian functions including one background.

Conclusion

The absorption spectra of the photocatalyst $[Re(CO)_2(bpy)\{P(OEt)_3\}_2](PF_6)$ in TEOA solvent and in the solid form have been investigated by the combination of ATR and THz-TDS in the frequency range of 0.3 - 2.5 THz.

The absorption spectrum of Re complex in TEOA solvent has three peaks at the frequencies of 1, 1.35, and 1.7 THz. Meanwhile, that of Re complex in the solid form displayed four peaks at the frequencies of 0.5, 1, 1.6, and 2.2 THz. The predominant 1.35-THz peak only appeared in the presence of TEOA solvent is assigned as the intermolecular vibration of the cation $[Re(CO)_2(bpy)\{P(OEt)_3\}_2]^+$ and TEOA molecules.

The disapperence of the 0.5-THz and 2.2-THz peaks, as well as the significant reduction of the 1.7-THz peak, can be explained by the replacement of the nearest neighbor anion PF_6^- by TEOA molecules. Moreover, this is the evidence that these absorptions are the

intermolecular vibrational modes between the cation $[Re(CO)_2(bpy)\{P(OEt)_3\}_2]^+$ and the anion $(PF_6)^-$. Comparing the calculation by Harabuchi et al. to our observation, the 1-THz peak can be assigned to originate from intramolecular mode of bpy.

The absorption spectrum of $[Re(CO)_3(dmb)Br]$ complex has been investigated by THz-TDS in the frequency range of 0.3 to 7 THz. Four peaks of $[Re(CO)_3(dmb)Br]$ complex have been observed at 0.5, 1.2, 1.8 and 2.8 THz. Based on the report of Harabuchi et al., the 1.2-THz and 1.8-THz peaks can be assigned as the vibrational modes of dmb ligand and the displacement of hydrogen atoms inside dmb ligand and other atoms, and 2.8-THz peak originates from the vibration of pure carbonyl.

Chapter V

Relaxation dynamics of $[Re(CO)_2(bpy)\{P(OEt)_3\}_2](PF_6)$ in TEOA solvent

In this chapter, the photo-induced dynamics of $[Re(CO)_2(bpy)\{P(OEt)_3\}_2](PF_6)$ in TEOA investigated by TR-ATR will be presented. The mixed solution of $[Re(CO)_2(bpy)\{P(OEt)_3\}_2](PF_6)$ and TEOA is irradiated by optical excitation at 400 nm wavelength with the power of 6 mW. The time delay between THz probe pulse and pump pulse were scanned at each one picosecond to map out the kinetics of the relaxation process. The temporal development of spectra in each picosecond was analyzed and discussed. TR-ATR results indicated the complex relaxation dynamics of the intermolecular vibration 1.35-THz peak with the lifetime in picoseconds timescale.

5.1 Experimental results

In TR-ATR measurement, the sample solution was photoexcited by 400 nm laser pulse, thus neither photochemical isomerization nor ligand substitution was induced by the excitation[95]. TEOA is the polar solvent with high viscosity (~130 cp at room temperature) and also the irreversibly sacrificial electron donor.

When $[Re(CO)_2(bpy)\{P(OEt)_3\}_2](PF_6)$ dissolves into TEOA solvent, the anion $(PF_6)^-$ is detached apart and move away far from the cation $[Re(CO)_2(bpy)\{P(OEt)_3\}_2]^+$. TEOA molecules distribute around $[Re(CO)_2(bpy)\{P(OEt)_3\}_2]^+$, thus the role of anion $(PF_6)^-$ is minor and we do not have to concern.

TR-ATR experiments were employed to carry out the excited state dynamics in the THz region of $[Re(CO)_2(bpy)\{P(OEt)_3\}_2](PF_6)$ in TEOA by the excitation of 400-nm pulses. The spectral evolution from -1 ps to 9 ps and from 9 ps to 24 ps are shown in Figs. 5.1a and 5.1b, respectively. The spectrum changes clearly after photoexcitation, which is redshifted (show a decrease in frequency) in 1 ps and returns slowly back to the initial position in 9 ps,

as shown in Fig. 5.1a. From 10 to 14 ps, the spectral changes in shape and intensity are observed in Fig. 5.1b.

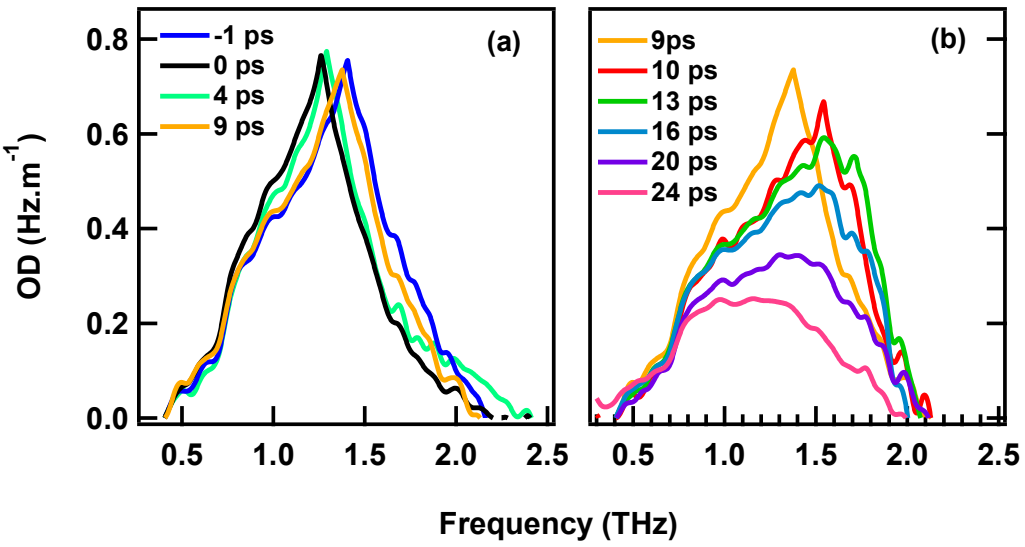

Figure 5.1: TR-ATR spectra of $[Re(CO)_2(bpy)\{P(OEt)_3\}_2](PF_6)$ in TEOA recorded at selected time: -1, 0, 4, and 9 ps (a); 9, 10, 13, 16, 20, 24 ps (d) after the photoexcitation with wavelength of 400 nm, pulse length of ~70 fs (FHWM), and power of 6 mW.

5.2 Data analysis

To analysis the experimental data, we have considered two possible ways applied for tracing the peak development of the intermolecular vibrational mode at 1.35 THz. Two fitting options follows:

1. The experimental data is fitted by two Gaussian peaks corresponding to the 1-THz and 1.35-THz peaks. The 1.7-THz peak is considered as an unchanged Gaussian peak with fixed parameters (peak position: 1.7 THz, intensity 0.13 and FWHM 0.4).

2. The experimental data is fitted by three Gaussian peakscorresponding to three vibrational modes at 1, 1.35, and 1.7 THz.

5.2.1 The experimental data fitted by two Gaussian peaks

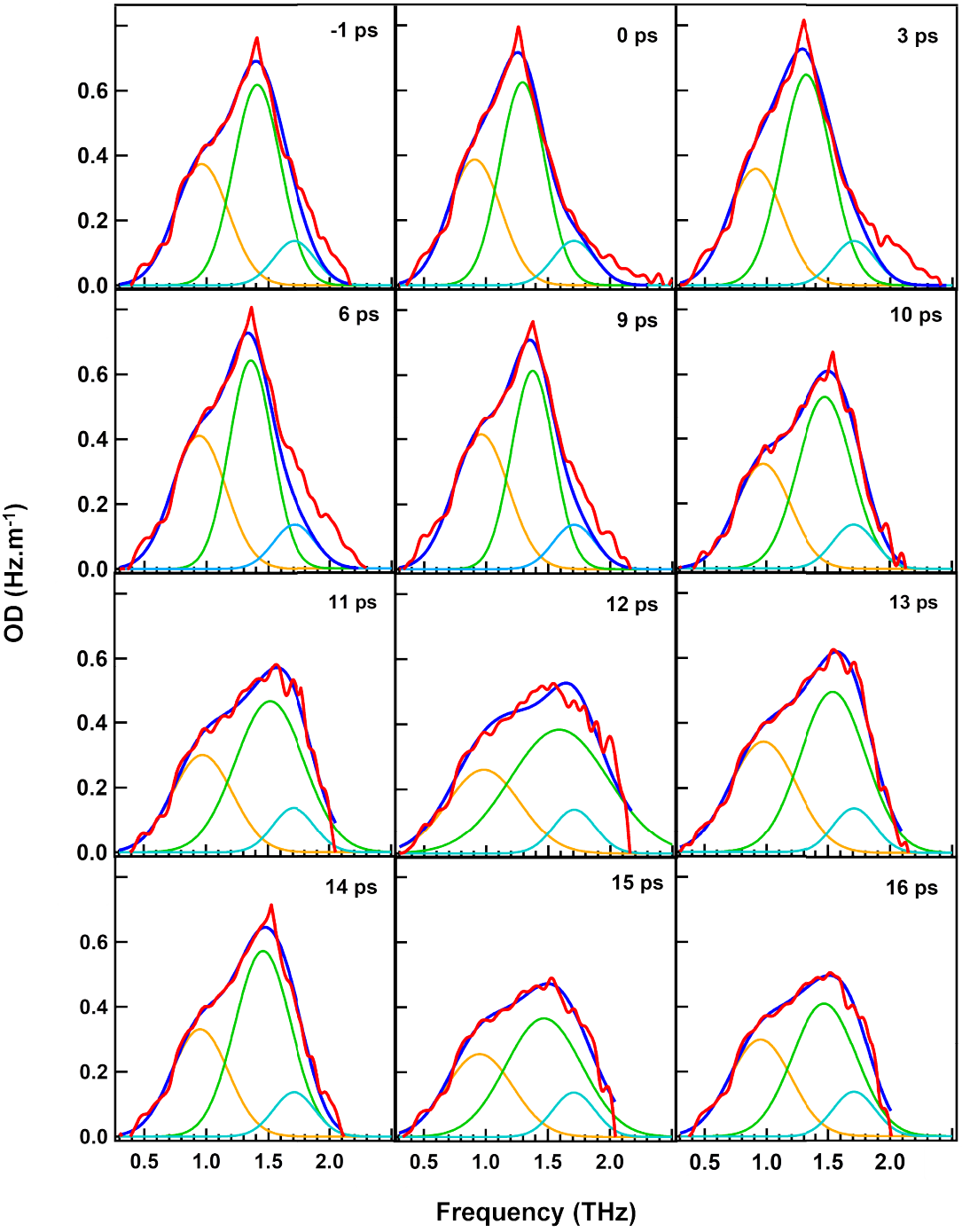

Figure 5.2: The fitting results of THz-ATR spectra at selected time: -1, 0, 1, 5, 9 and 10 ps. The experimental data is shown in red, the sum in blue, the 1-, 1.35, and 1.7-THz peaks in orange, green and skyblue, respectively.

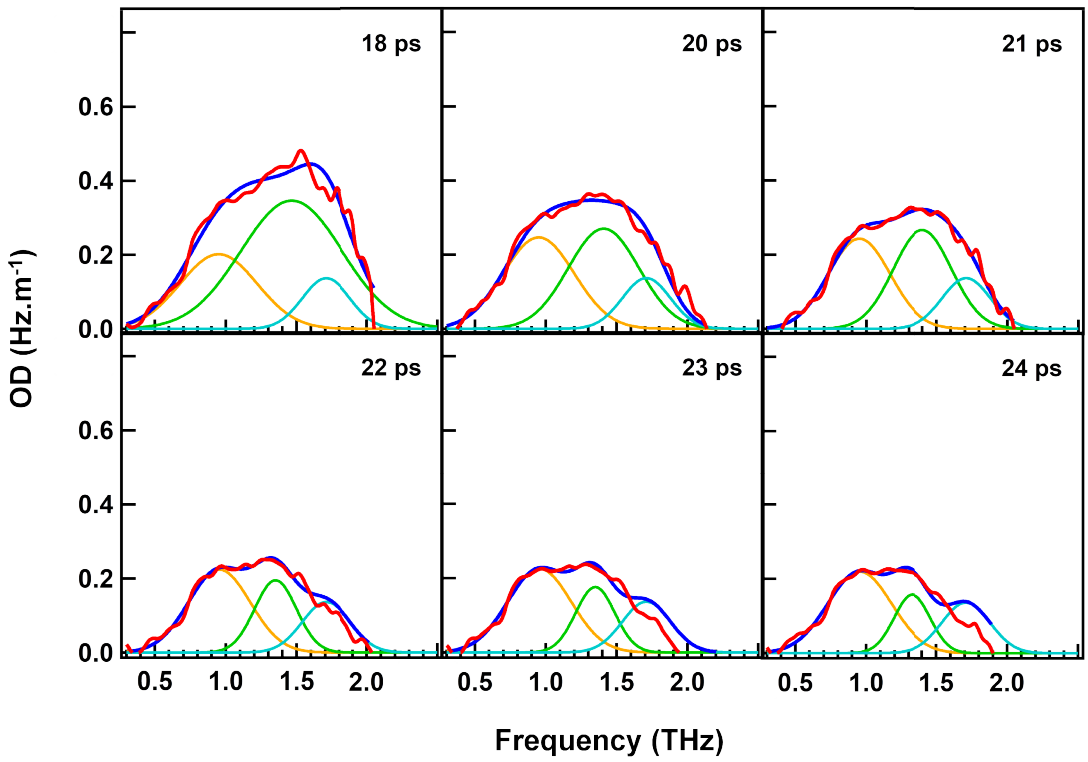

Figure 5.3: The fitting results of THz-ATR spectra at selected time: 14, 16, 18, 19, 20 and 22 ps. The experimental data is shown in red, the sum in blue, the 1-, 1.35, and 1.7-THz peaks in orange, green and skyblue, respectively.

Figures 5.2 and 5.3 show the fitting results using Gaussian functions. The fitting curves are well-fitted with the experimental data.

Just after photoexcitation, 1-THz and 1.35-THz peaks are immediately redshifted and the peak (position, intensity, width and area) evolution experiences three steps relaxation, as displayed in Figs. 5.4 and 5.5.

In the first step from 0 to 9 ps, the 1-THz, 1.35-THz peaks are blueshifted (show an increase in frequency) from 0.9, 1.28 THz to 0.96, 1.37 THz, respectively (Fig. 5.4a). The peak areas of two peak remain the same over the time, as shown in Fig. 5.4b. In the second step, the peak areas of 1-THz and 1.35-THz peak are still unchanged between 9 and 13 ps, the 1.35-THz peak shifts rapidly from 1.37 THz to 1.55 THz. The third step starts from 14 ps, in which the peak area of the 1-THz decreases slowly and the peak area of 1.35-THz peak is supressed dramatically. In addition, the 1.35-THz peak shifts back to 1.38 THz, as shown in Fig. 5.4a. It is noticed that the 1-THz peak position in the second and the third steps remains unchanged.

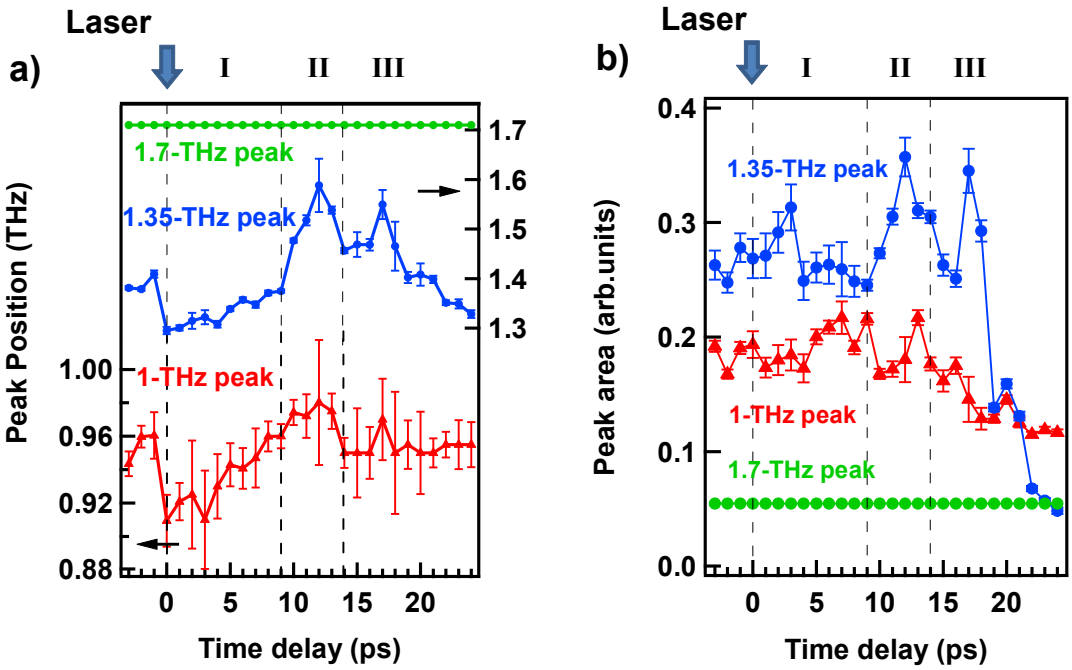

Figure 5.4: The peak position (a) and peak area (b) of the individual peak of Re complex in TEOA solvent plotted as a function of time from the photo-excitation.

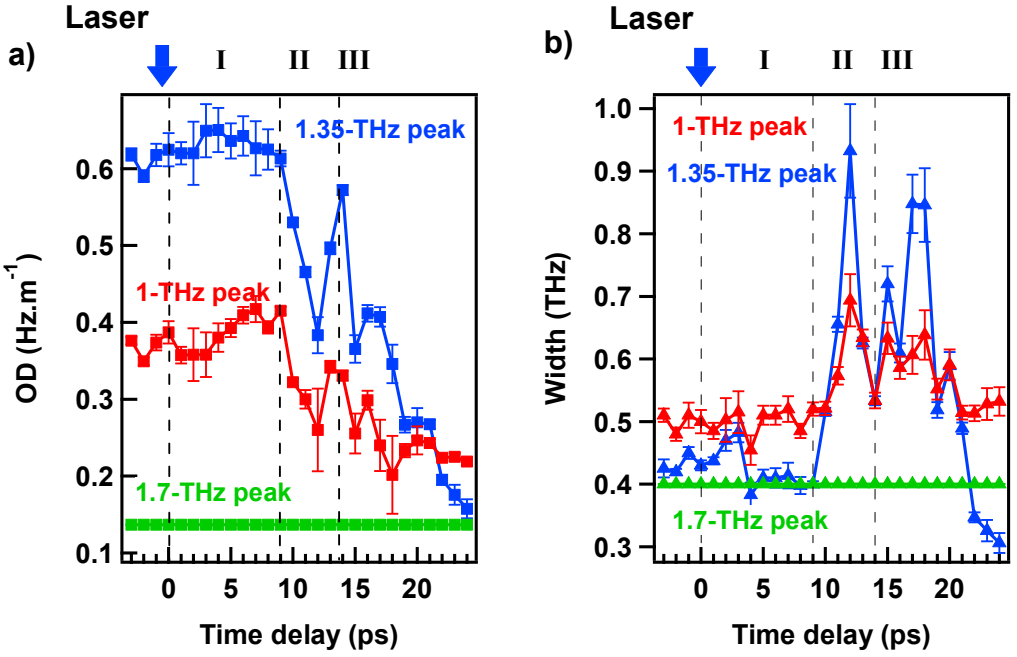

Figure 5.5: The peak intensity (a) and peak width (b) of the individual peak of Re complex in TEOA solvent plotted as a function of time from the photo-excitation.

The intensities of the 1-THz and 1.35-THz peaks decrease from 9 ps, while their widths increase from 9 to 13 ps and finally become narrow, as shown in Fig. 5.5. From 9 to 13 ps, the width of the 1.35-THz peak increases rapidly from 0.4 to 0.9 THz and its rapid jump to 1.55 THz indicate a new peak component appears in the high-frequency area (~1.7

THz). Therefore, the 1.35-THz peak (FWHM ~ 0.9 THz) is suggested to divide into two peaks at 1.35 and 1.7 THz (FWHM ~ 0.4 THz).

5.2.2 The experimental data fitted by three Gaussian peaks

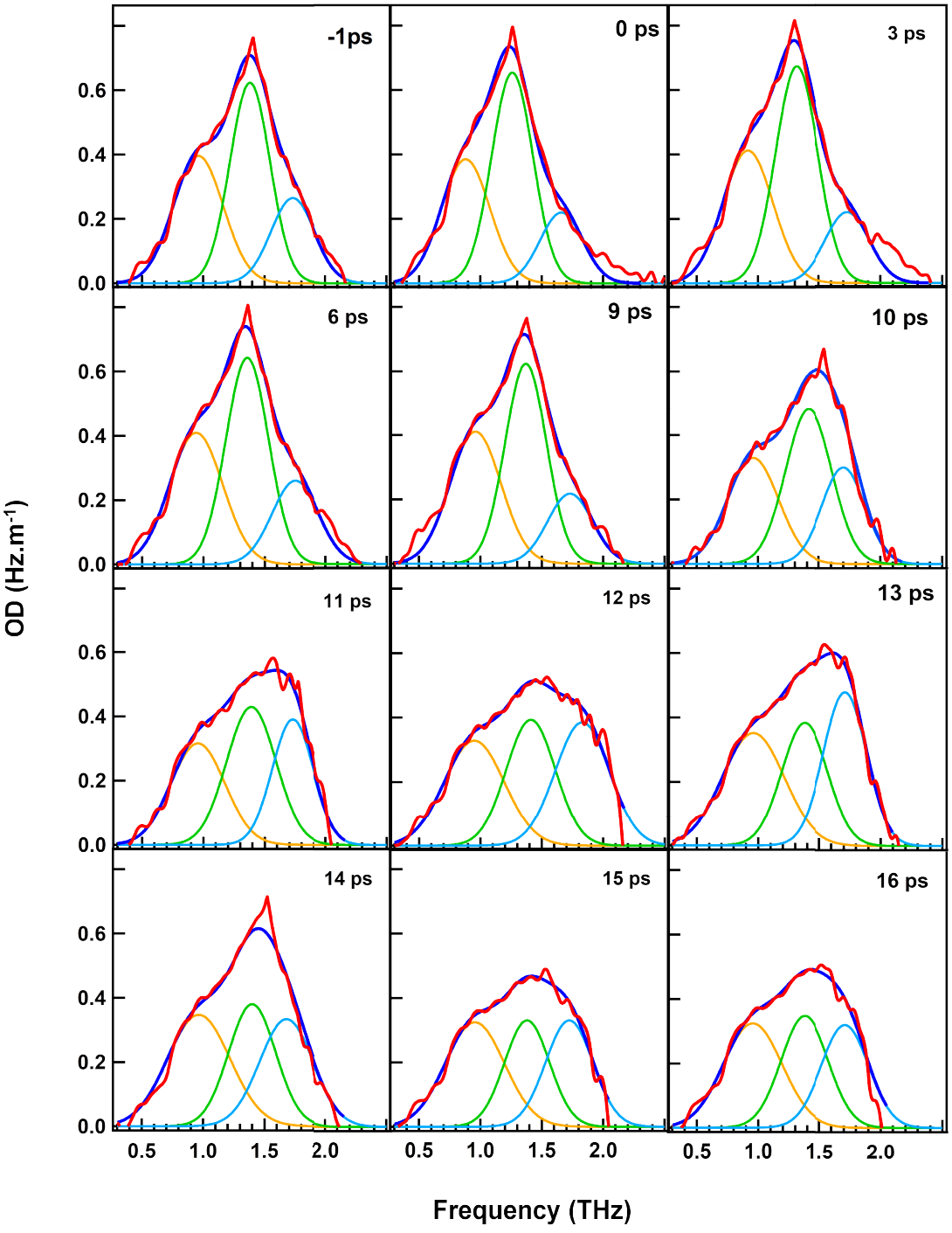

Figure 5.6: The fitting results of THz-ATR spectra at selected time: -1, 0, 1, 5, 9 and 10 ps. The experimental data is shown in red, the sum in blue, the 1-, 1.35, and 1.7-THz peaks in orange, green and skyblue, respectively.

Next, I tried to fit the time-dependent absorption spectra using the combination of indivisual three Gaussian functions corresponding to 1-THz,1.35-THz and 1.7-THz peaks, which relate to the peaks shown in the absorption spectrum (Fig. 4.4). Figs. 5.6 and 5.7 show the fitting results of each spectum at selected time delay. The fitting curves are well-fitted with the experimental data. Just after photoexcitation, 1-THz and 1.35-THz peaks are immediately redshifted from 0.96 to 0.88 THz and from 1.38 to 1.26 THz, respectively. Following that, the peak (position, intensity, FHWM and area) evolution experiences three-step relaxation, as displayed in Figs. 5.8 and 5.9.

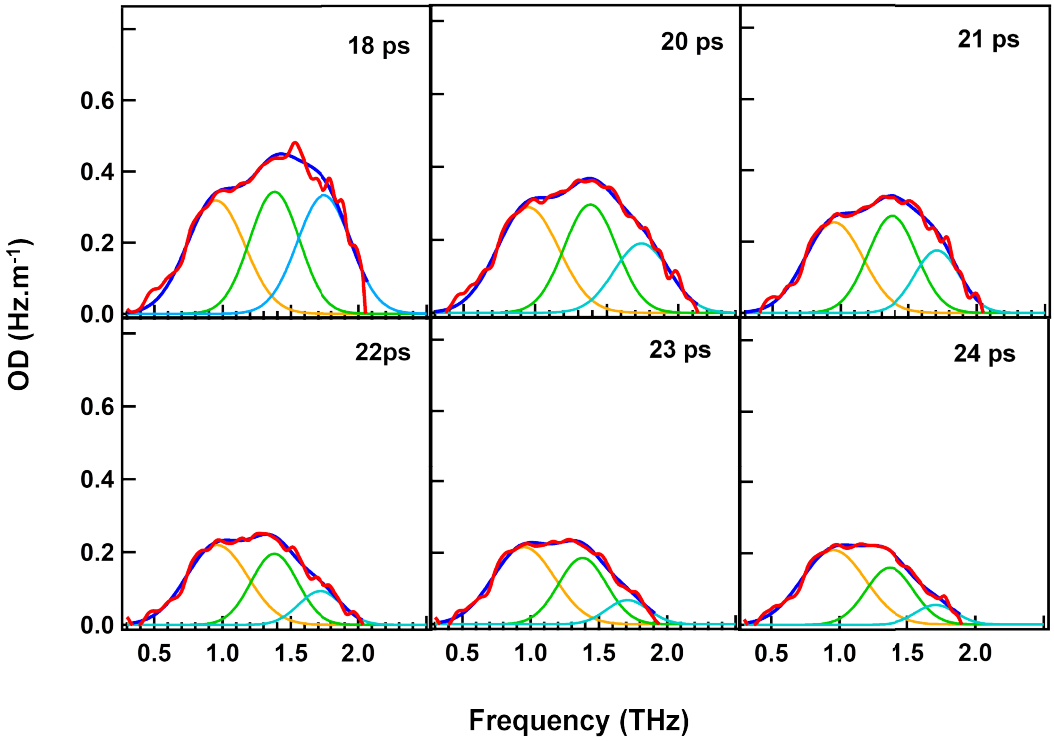

Figure 5.7: The fitting results of THz-ATR spectra at selected time: 11, 13, 16, 18, 20 and 22 ps. The experimental data is shown in red, the sum in blue, the 1-, 1.35, and 1.7-THz peaks in orange, green and skyblue, respectively.

Comparing between results of the assumed two fitting models shown in Figs. 5.4, 5.5, 5.8 and 5.9, the evolution of all peaks in the first and the third transitional steps are similar to each other. The second transitional step has significant difference between them, where the decrease of the 1.35-THz peak area seems to be compensated by the increase of the 1.7-THz peak area, as shown by the unchange of the sum of peak area (Fig. 5.9). In addition, the second transition in the two Guassian fitting method shows the 1.35-THz peak shifts and widens rapidly to the higher frequency side, while the peak intensity drops down (the peak area persists unchanged). This manner indicates a part of 1.35-THz peak suddenly transform

to the new peak in the higher frequency side (around 1.7 THz). This dynamics is proposed the breaking and forming new interaction between molecules. Furthermore, the fitting result of 22, 23, and 24 ps showed in Fig. 5.7 do not reach the agreement with the experiment data.

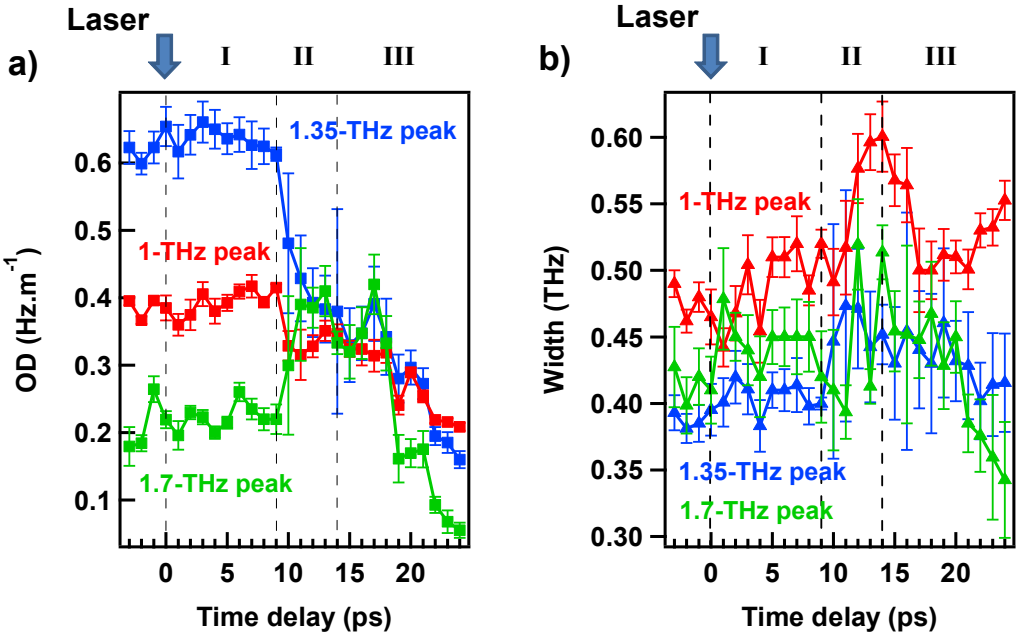

Figure 5.8: The peak intensity (a) and peak width (b) of the individual peak of Re complex in TEOA solvent plotted against time.

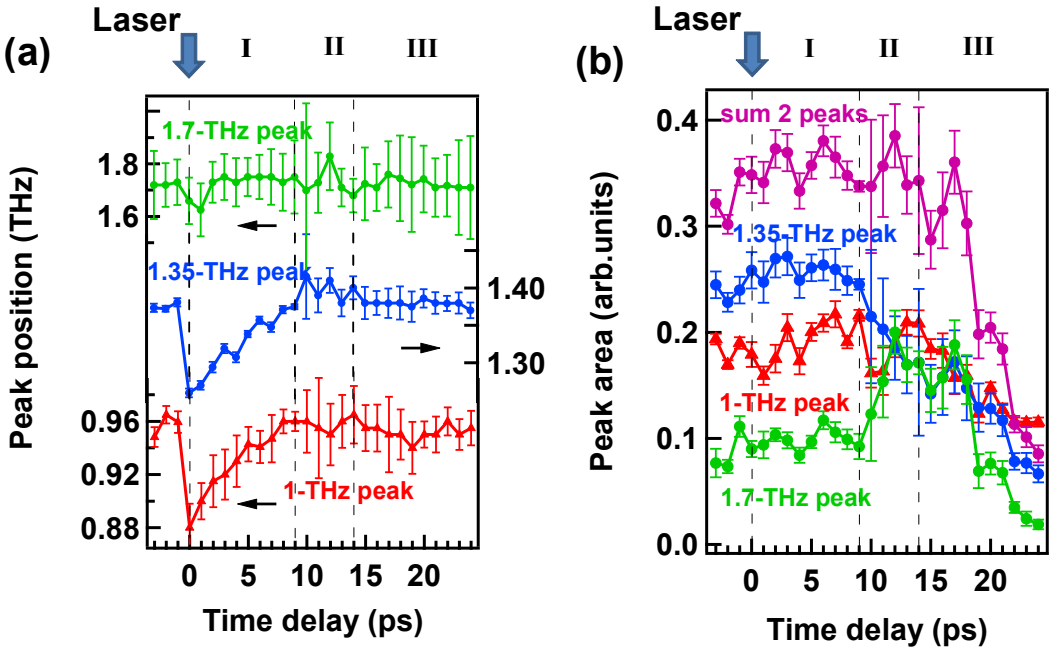

Figure 5.9: The peak position (a) and peak area (b) of the individual peak of Re complex in TEOA solvent plotted against time.

In the three Gaussian fitting method, the 1.7-THz peak represents well for the breaking (1.35-THz peak slumps in intensity) and forming (1.7-THz peak soars in intensity)

new interaction between molecules upon excited state dynamics of the intermolecular vibration from 10 to 14 ps. Therefore, we choose the three Gaussian fitting to explain our experimental results.

5.2.3 Three-step relaxation of the intermolecular vibrational mode:

Figure 5.8a shows the temporal evolution of peak intensity. From 0 to 9 ps (first step), the intensity of all peaks remains the same but the 1-THz, 1.35-THz peaks are gradually blueshifted from 0.88, 1.26 THz to 0.96, 1.38 THz, respectively, as shown in Fig. 5.9a. From 10 to 24 ps (second step), that of the 1-THz peak decreases gradually. Meanwhile, the intensity of the 1.35-THz decreases but oppositely the 1.7-THz peak increases from 10 to 14 ps, respectively, and the sum of these peaks is almost constant in time. After 14 ps (third step), their intensities are suppressed dramatically. Figure 5.8b shows the fluctuation in the width of these peaks. Noticeably, the peak position of the 1-THz and 1.7-THz peaks are unchanged from 10 ps and in 24 ps, respectively.

5.3 Discussion

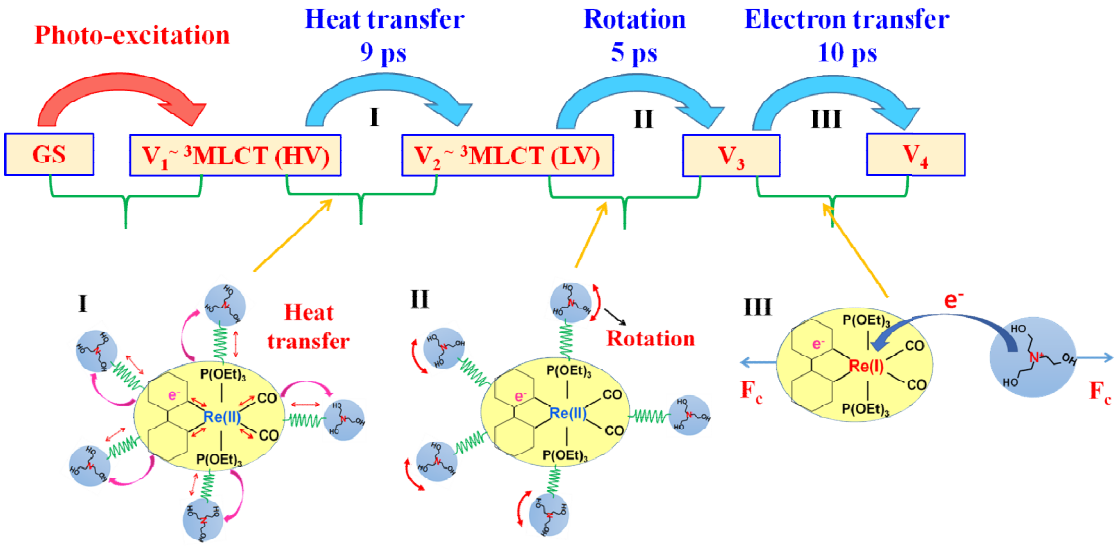

Figure 5.10: Schematic diagram and molecular forms after photexcitation. The top diagram shows the three-step dynamic from the highest excited state V_1 through the lowest excited state V_4 of $[Re(CO)_2(bpy)\{P(OEt)_3\}_2](PF_6)$ in TEOA solvent in the range of 0.3-2.5 THz. The bottom diagram illustrates the interaction between Re complex and TEOA molecules corresponding to each dynamical step I-III.

The observed temporal structure suggests the electronic and vibrational relaxation with three minor steps, where four electronic excited states, namely V_1, V_2, V_3, and V_4, exists

and are related to the dynamics of the intermolecular vibrations as shown in Fig. 5.10a. The lifetimes of V_1 to V_3 are in picoseconds to several ten picoseconds. Optical pulse of 400-nm (3.1 eV) photons excites electrons from the ground state to the singlet metal-to-ligand charge transfer state (^{1}MLCT), in which one electron of Re atoms transfers to bpy ligands, forming $[Re(II)(CO)_2(bpy^-)\{P(OEt)_3\}_2]^+$ [94,95].

The electronic decay to the hot triplet excited states (^{3}MLCT(HV)) from ^{1}MLCT[13-17] simultaneously occurs by ultrafast intersystem crossing (ISC) with a lifetime of a few hundred femtoseconds. Since ISC is much faster than our time resolution (>1 ps), our observation can be assigned to the decay processes after the ^{3}MLCT state, thus the V_1 state can be assigned as the ^{3}MLCT(HV) state.

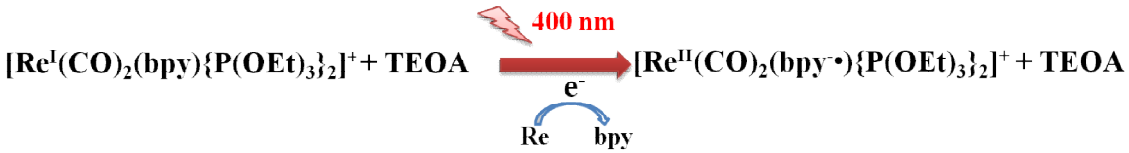

Scheme 5.1: The formation of the excites state of $[Re^I(CO)_2(bpy)\{P(OEt)_3\}_2]^+$ after photo-excitation.

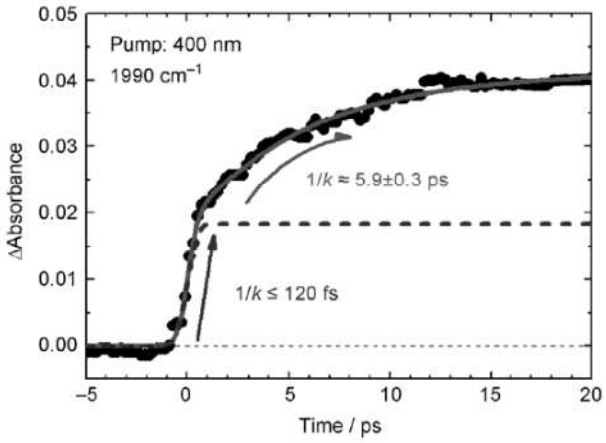

Figure 5.11: Time profile of the absorbance change of fac-$[Re(bpy)(CO)_3Cl]$ at 1990 cm^{-1} attributable to CO stretching band of ^{3}MLCT(LV) in THF following excitation with a 400 nm laser pulse. The solid line is the curve calculated from a single-exponential and step function convoluted with a laser function. [34]

Just after the photo-excitation, all peaks shift to the lower frequency side and then gradually come back to the initial position in 9 ps. This relaxation time scale agrees with the lifetime of the vibrational cooling from the ^{3}MLCT(HV) to the lowest vibrational

^{3}MLCT(LV) excited state (4-10 ps) observed by the υ(CO) stretching bands in IR region[15], as shown in Fig. 5.11. This can be assigned as the first step from V_1 to V_2 of the decay process as shown in Fig. 5.10a, i.e., it is concluded that the relaxation dynamics from V_1 to V_2 is the vibrational cooling of the ^{3}MLCT band, and the V_2 level corresponds to be the ^{3}MLCT(LV) state.

The 1-THz peak shifts in the same behavior as the stretching[34] of bpy ligand mode in the vibration mode between $[Re(CO)_2(bpy)\{P(OEt)_3\}_2]^+$ and TEOA molecules as shown in Fig 5.10b-1. The stretching of bpy ligand also manifests the relaxation of the ^{3}MLCT band.

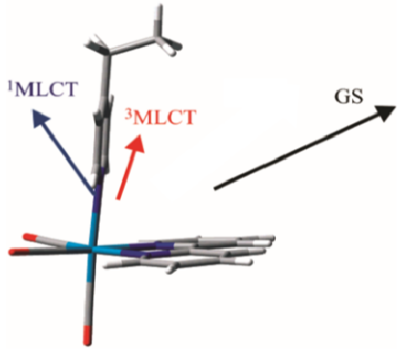

Figure 5.12: Relative size and orientation of dipole moment vectors of the ground-state (black) and excited-state ^{1}MLCT (purple), and ^{3}MLCT (red) of $[Re(Etpy)(CO)_3(bpy)]^+$, projected onto the optimized ground-state molecular structure. Dipole moment vectors originate in the center of charge. They lie in the molecular symmetry plane. [96]

In the V_2-V_3 transitional step (second step) from 10 to 14 ps, the time-independent sum of intensities of the 1.7-THz and 1.35-THz peaks suggests that the 1.35-THz peak is suddenly shifted to the higher frequency of 1.7 THz. This phenomenon can be explained as that TEOA molecules become closer to $[Re^{II}(CO)_2(bpy^-)\{P(OEt)_3\}_2]^+$ ions as shown in Fig. 5.10b-2. TEOA molecules are supposed to rotate because of the dipole-dipole interaction between TEOA molecules and $[Re^{II}(CO)_2(bpy)((P(OEt)_3)_2]^+$ ions[28]. Indeed, before the photo-excitation, the dipole moments of $[Re^{I}(CO)_2(bpy)\{P(OEt)_3\}_2]^+$ ions and TEOA molecules are parallel to each other. The dipole direction of $[Re^{II}(CO)_2(bpy)\{P(OEt)_3\}_2]^+$ ions is changed by the photo-excitation, as shown in Fig. 5.12. Hence, just after the photo-excitation, TEOA molecules tend to rotate to reach the stabilization with the $[Re^{II}(CO)_2(bpy)\{P(OEt)_3\}_2]^+$ (equilibrium solvation) (Fig.5.13). The rotation of TEOA molecules is disturbed by other molecules, thus, as shown in Fig. 5.9b the peak area is constant in region 1.

In this region, the heat transfer occurs from $[Re^{II}(CO)_2(bpy)\{P(OEt)_3\}_2]^+$ ions to TEOA molecules and then the temperature of the vibrational modes of TEOA increases. However, the increase of the temperature of TEOA molecules accelerates the rotation but not enough. When the vibrational cooling finishes, the temperature of TEOA molecules may be high enough to rotate. Then, the sudden jump of the 1.35-THz peak to 1.7 THz occurs by the heat assist effect. Figure 5.10b-2 displays a schematic figure of the rotation of TEOA molecules in the second step.

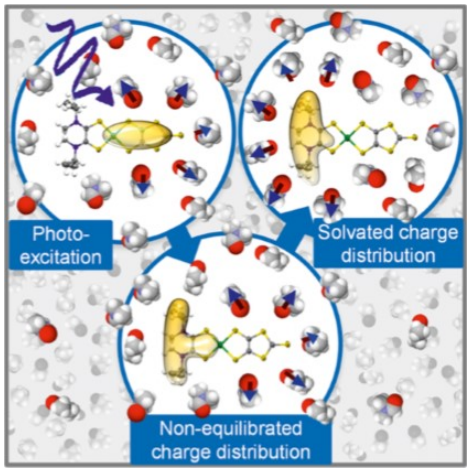

Figure 5.13: Schematic diagram illustrates the solvent molecules reacting to the electronic change of the solute molecule. [97]

In the V_3-V_4 transition (third step), the steep decrease of all the peak area can be assigned as the electron transfer process from nitrogen atoms to Re atoms. Indeed, the minimal relative distance between the nitrogen atom of TEOA molecule and Re atom causes the overlap of their wave function. That positively allows the electron transfer from TEOA molecules to Re atoms. As a result, the reduced species $[Re^{I}(CO)_2(bpy^{\bullet -})\{P(OEt)_3\}_2]^+$ and $TEOA^+$ are formed, as shown in scheme 5.2 and Fig. 5.10b-3.

The repulsive Coulomb force between Re(I) and $TEOA^+$ causes the significant reduction of the peak areas of the 1.35-THz and 1.7-THz peaks. Due to the electron transfer, there is a change in electronic density of $[Re(CO)_2(bpy^{-\bullet})\{P(OEt)_3\}_2]^+$ ions, which might cause the slight decrease of the intensity as well as the peak area of the 1-THz peak.

According to the report of L. M. Kiefer *et al.*, the electron transfer from TEOA molecules to $[Re(Br)(CO)_3(bpy)]$ complex in TEOA(20%)/THF(80%) solvent occurs in a few hundred picoseconds[36]. Comparing their experimental conditions with ours, where we use pure TEOA solvent, the electron transfer is supposed to occur faster (probably in a few

ten picoseconds). Therefore, the third transitional step in our observation assigned as electron transfer process is reasonable.

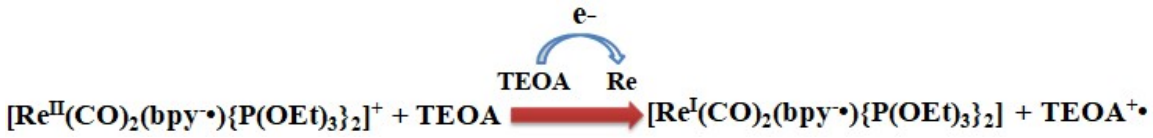

Scheme 5.2: The formation of the reduced species [Re^{I}(CO)$_2$(bpy-){P(OEt)$_3$}$_2$] after electron transfer from TEOA. [88,98]

Conclusion

The relaxation dynamics of a photocatalyst [Re(CO)$_2$(bpy){P(OEt)$_3$}$_2$](PF$_6$) in 2,2',2'' Nitrilotriethanol (TEOA) solvent has been studied by TR-ATR.

TR-ATR study shows three-step relaxation of the intermolecular vibrational mode at 1.35 THz corresponding to four excited states with the lifetime in picoseconds. Just after photoexcitation, 1-THz and 1.35-THz peaks are redshifted in 1 ps. In the first transitional step from V_1 to V_2, these peaks gradually return back to the initial position in 9 ps. This relaxation was determined as the vibrational cooling of the ^{3}MLCT state.

In the second transitional step from V_2 to V_3, the increase of the 1.7-THz peak intensity is compensated with the decrease of the 1.35-THz peak intensity, which is identified by the unchanged total intensity from 10 to 14 ps. The sudden jump of the 1.35-THz peak to the higher frequency at 1.7 THz could be explained by the effect of the heat transfer on the rotation of TEOA molecules.

In the final transitional step from V_3 to V_4, the sum of peak area decreases from 14 ps was interpreted by the repulsive Coulomb force causing by the electron transfer process from nitrogen atoms to Re atoms.

Chapter VI

Conclusions and Prospective Research

6.1 Generation and detection of THz radiation

We have constructed THz-TDS, THz-ATR and TR-ATR setups, in which THz radiation is generated by various methods using optical rectification (ZnTe and GaP crystals) and air plasma, and is detected by electro-optical sampling method. THz-ATR and TR-ATR used the THz-TDS and TRTS technique. The generated THz bandwidth obtained from the frequency range of 0.3 to 2.5 THz (ZnTe crystals), 0.3 to 7 THz (GaP crystals and air plasma) with the qualified S/N ratio, as shown in Fig. 6.1.

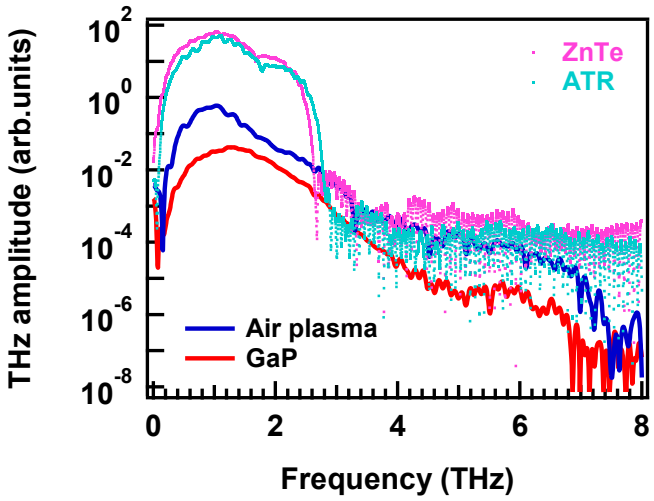

Figure 6.1: Comparison of THz spectra generated by the normal THz-TDS and the THz-ATR based on the THz-TDS constructed in this work.

6.2 Absorption spectra of $[Re(CO)_2(bpy)\{P(OEt)_3\}_2](PF_6)$ complex

The absorption spectra of $[Re(CO)_2(bpy)\{P(OEt)_3\}_2](PF_6)$ in solid form (powder) and in TEOA solvent were investigated using the combination of THz-TDS and THz-ATR. The THz-ATR spectrum showed three vibrational peaks at 1, 1.35 and 1.7 THz (Fig. 6.2b). Meanwhile, THz-TDS spectrum in the solid form displayed four absorption peaks at 0.5, 1, 1.65 and 2.2 THz (Fig. 6.2a).

Comparing between absorption spectra of Re complex in TEOA solvent and in solid form, we concluded that: the 1.35-THz peak is the intermolecular vibrational mode between $[Re(CO)_2(bpy)\{P(OEt)_3\}_2]^+$ cation and TEOA molecules, the 0.5-, 1.65-, and 2.2-THz peaks are intermolecular vibrational modes of $[Re(CO)_2(bpy)\{P(OEt)_3\}_2]^+$ cation and $(PF_6)^-$ anion and the 1-THz peak is the intramolecular vibrational mode contributing from bpy ligand.

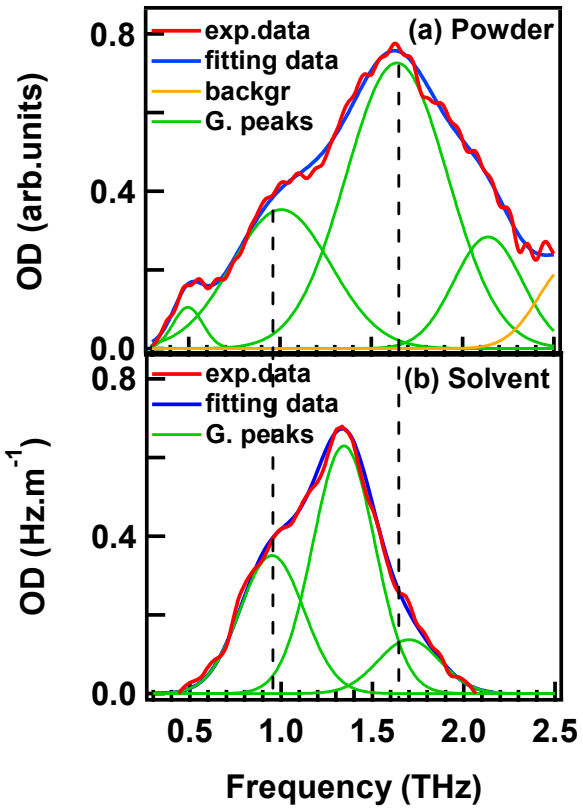

Figure 6.2: Absorption spectra of Re complex in solid form (a) and in TEOA (b) in the frequency range from 0.3 to 2.5 THz. The experimental data is shown in red color, individual Gaussian functions in green, and the sum in blue.

6.3 Relaxation dynamics of $[Re(CO)_2(bpy)\{P(OEt)_3\}_2](PF_6)$ in TEOA solvent

Relaxation dynamics on Re complex in TEOA solvent have been studied by TR-ATR. TR-ATR spectra showed the positional displacement from -1 ps to 9 ps and spectral change in shape and intensity from 10 to 24 ps, as shown in Fig. 6.3.

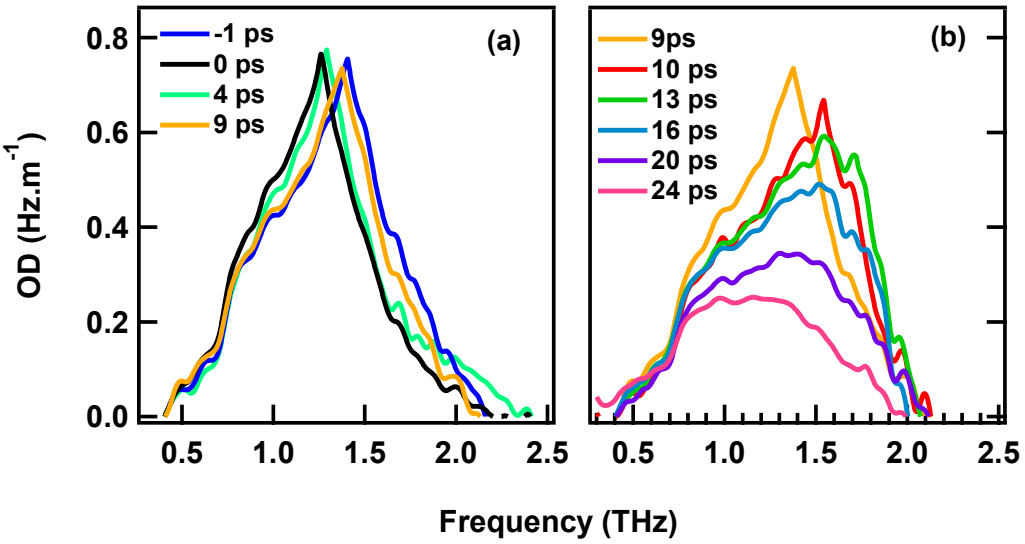

Figure 6.3: TR-ATR spectra of Re complex in TEOA recorded at selected time: -1, 0, 4, and 9 ps (a); 9, 10, 13, 16, 20, 24 ps (d) after after the photoexcitation of 400 nm, ~70 fs (FWHM), and the power of 6 mW.

The result indicated three transitional steps of the intermolecular vibration corresponding to four excited states (ES) with the lifetime in picoseconds: V_1 (the highest excited state), V_2, V_3, and V_4 (the lowest ES).

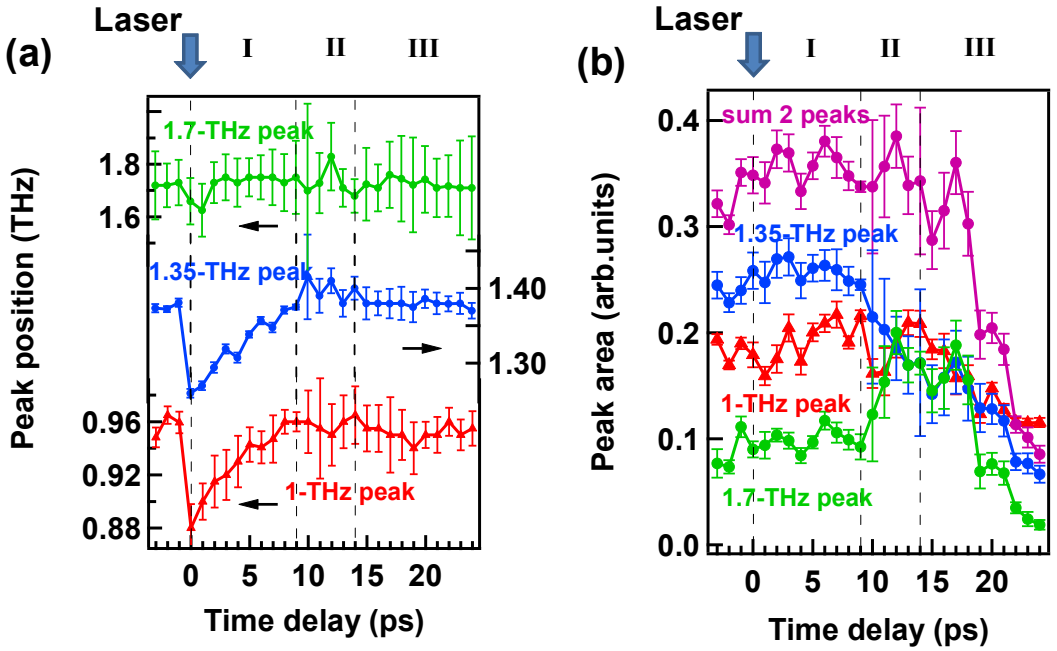

Figure 6.3: The peak position (a) and peak area (b) of the individual peak of Re complex in TEOA solvent plotted against time.

In the first transitional step from V_1 to V_2, the 1-THz and 1.35-THz peaks were blueshifted from 0 to 9 ps (Fig. 6.3a), this relaxation was determined as the vibrational cooling of the ^{3}MLCT state.

In the second transitional step from V_2 to V_3, the increase of the peak area of the 1.7-THz peak is as the same amount as the decrease of that of the 1.35-THz peak, identified by the unchanged sum peak area from 10 to 14 ps (Fig.6.3b). As a result, the 1.35-THz peak suddenly jumps to the higher frequency at 1.7 THz. This behavior could be explained by the effect of the heat transfer on the rotation of TEOA molecules.

In the final transitional step from V_3 to V_4, the sum of peak area decreases from 14 ps (Fig. 6.3b) was interpreted by the repulsive Coulomb force causing by the electron transfer process from nitrogen atoms to Re atoms.

Figure 6.3 summaries the whole dynamics of $[Re(CO)_2(bpy)\{P(OEt)_3\}_2](PF_6)$ in TEOA solvent from V_1 to V_4 and it also illustrates the interaction between $[Re(CO)_2(bpy)\{P(OEt)_3\}_2]^+$ and TEOA molecules corresponding to each dynamical step.

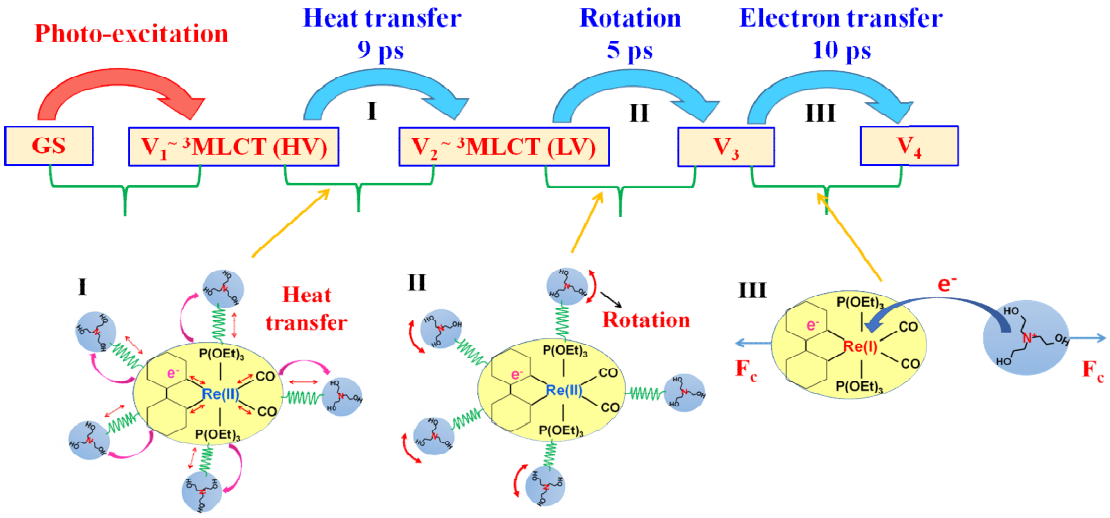

Figure 6.4 Schematic diagram and molecular forms after photexcitation. The top diagram shows the three-step dynamic from the highest excited state V_1 through the lowest excited state V_4 of $[Re(CO)_2(bpy)\{P(OEt)_3\}_2](PF_6)$ in TEOA solvent in the range of 0.3-2.5 THz. The bottom diagram illustrates the interaction between Re complex and TEOA molecules corresponding to each dynamical step I-III.

The vibrational cooling of the ^{3}MLCT band and the intermolecular ET process have been observed by TR-ATR. Interestingly, the second decay process in our investigation is a novel dynamic process that can only be obtained by intermolecular vibrational dynamics in

the THz region. We successfully observed the first and second steps of the photocatalytic process and these findings help us to understand photocatalysis detailed.

This observation showing the first success of using TR-ATR in investigation photocatalytic dynamics contributes to open following successes in exploring more important dynamics of Re complexes in low frequency in the future.

6.4 Prospective research

In this thesis, I could measure the THz dynamics of the charge transfer in photo-synthesis materials for the first time. However, because of the limitation of THz bandwidth owing to the optical elements, we cannot observe in the frequency region above 2.5 THz. That limitation caused the uncertain explanation for the last dynamics step that observed by TR-ATR. In order to overcome that issue, we plan to use GaP crystals and air plasma to generate and detect THz radiation with the bandwidth expanding to 7 THz in TR-ATR setup. Moreover, the sample is irradiated by intense excitation pulse that could cause the degeneration of the sample. Hence, we suggest that the small closed-cycle system showing in Fig. 6.5 for flowing the liquid sample during photoexcitation would help to prevent the degeneration. The evaporation of solvent occurs, so the closed-cycle system can avoid that as well.

If we can make such the improvement, we suppose that we will be able to observe the intermolecular vibrational modes of other Re complexes and other kinds of materials in the ground state as well as the relaxation dynamics. This study would contribute to open new insights into the low-frequency region that cannot be easily accessed.

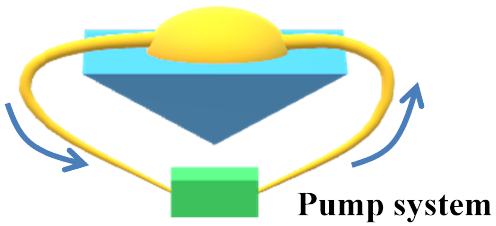

Figure 6.5: The closed-cycle system.

Acknowledgments

First of all, I would like to thank my supervisors, Prof. Shin-ichi Kimura who accepted me as his student and giving help, advice, discussion and being patient for the last number of years.

My big thanks go to Dr. Hiroshi Watanabe who directly mentors me during my whole study. Thanks for being enthusiastic, diligent, kind, and patient in helping me to gain knowledge and accomplish my doctoral course.

I would like to thank Prof. Osamu Ishitani for sighnificant value discussion and Dr. Yusuke Tamaki for supporting in synthesizing the material.

Nextly, I would thank Prof. Junji Watanabe and Dr. Yoshiyuki Ohtsubo for giving advice and comment on my work.

Special thanks to my family for their support over the years. My thanks also go to the laser group member, who is willing help me whenever I have any problem with the laser.

I really appreciate to Kamei san who helped me to do paperwork when I first came to Japan. I must thank all members of Kimura's Lab, who are very friendly, helpful and hospitable, that makes me feel like I am at home.

Finally, I would like to thank Monbukagakusho (MEXT) scholarship for financial support.

Reference

(1) http://www.bp.com/en/global/corporate/about-bp/energyeconomics/statistical-review-of world-energy.html.

(2) S. C. Roy, O. K. Varghese, M. Paulose, C. A. Grimes, ACS Nano. **4**, 1259 (2010).

(3) T. Morimoto, T. Nakajima, S. Sawa, R. Nakanishi, D. Imori, O. Ishitani. J. Am. Chem. Soc. **135**, 16825 (2013).

(4) N. S. Lewis, D. G. Nocera. Proc. Natl. Acad. Sci. U.S.A. **103**, 15729 (2006).

(5) T. R. Cook, D. K. Dogutan, S. Y. Reece, Y. Surendranath, T. S. Teets, D. G. Nocera. Chem. Rev. **110**, 6474 (2010).

(6) V. Balzani, A. Credi, M. Venturi. ChemSusChem. **1**, 26 (2008).

(7) D. G. Nocera, Acc. Chem. Res. **45**, 767 (2012).

(8) H. Takeda, O. Ishitani, Coord. Chem. Rev. **254**, 346 (2010).

(9) H. Takeda, K. Koike, T. Morimoto, H. Inumaru, O. Ishitani, Adv. Inorg. Chem. **63**, 137 (2011).

(10) T. Yui, Y. Tamaki, K. Sekizawa, O. Ishitani, Top. Curr. Chem. **303**, 151 (2011).

(11) S. Berardi, S. Drouet, L. Francàs, C. Gimbert-Suriñach, M. Guttentag, C. Richmond, T. Stoll, A. Llobet, Chem. Soc. Rev. **43**, 7501 (2014).

(12) G. Knör, Coord. Chem. Rev. **304**, 102 (2015).

(13) https://www.titech.ac.jp/english/research/stories/faces15_ishitani.html

(14) T. Inoue, A. Fujishima, S. Konishi, K. Honda, Nature **277**, 637 (1979).

(15) H.-K. Lim, H. Shin, W. A. Goddard, Y. J. Hwang, B. K. Min, H. J. Kim, Am. Chem. Soc. **136**, 11355 (2014).

(16) B. J. Fisher, R. J. Eisenberg, Am. Chem. Soc. **102**, 7361 (1980).

(17) M. D. Sampson, A. D. Nguyen, K. A. Grice, C. E. Moore, A. L. Rheingold, C. P. Kubiak, J. Am. Chem. Soc. **136**, 5460 (2014).

(18) J. Hawecker, J. M. Lehn, R. Ziessel, Helv. Chim. Acta. **69**, 1065 (1986).

(19) K. Kalyanasundaram, Coord. Chem. Rev. **46**, 159 (1982).

(20) C. Kutal, M. A. Weber, G. Ferraudi, D. Geiger, Organometallics. **4**, 2161 (1985).

(21) C. Kutal, A. J. Corbin, G. Ferraudi, Organometallics. **6**, 553 (1987).

(22) P. Kurz, B. Probst, B. Spingler, R. Alberto, Eur. J. Inorg. Chem. **15**, 2966 (2006).

(23) H. Takeda, K. Koike, H. Inoue, O. Ishitani, J. Am. Chem. Soc. **130**, 2023 (2008).

(24) B. Gholamkhass, H. Mametsuka, K. Koike, M. Furue, O. Ishitani, Inorg. Chem. **44**, 2326 (2005).

(25) K. Koike, S. Naito, S. Sato, Y. Tamaki, O. Ishitani, J. Photochem. Photobiol. A. **207**, 109 (2009).

(26) H. Takeda, O. Ishitani, Coord. Chem. Rev. **254**, 346 (2010).

(27) M. D. Doherty, D. C. Grills, J. T. Muckerman, D. E. Polyansky, E. Fujita, Coord. Chem. Rev. **254**, 2472 (2010).

(28) R. E. Blankenship, D. M. Tiede, J. Barber, G. W. Brudvig, G. Fleming, Science **332**, 805 (2011).

(29) S. Sato, O. Ishitani, Coord. Chem. Rev. **282**, 50 (2015).

(30) G. Sahara, O. Ishitani, Inorg. Chem. **54**, 5096 (2014).

(31) Y. Yamayaki, H. Takeda, O. Ishitani, Photochem. Rev. **25**, 106 (2015).

(32) A. E. Nahhas, C. Consani, A. M. Blanco-Rodriguez, K. M. Lancaster, Inorg. Chem. **50**, 2932 (2011).

(33) D. J. Liard, M. Busby, P. Matousek, M. Towrie, A. Vlček, J. Phys. Chem. A. **108**, 2363 (2004).

(34) S. Sato *et al.*, Chem. A. Eur. J. **18**, 15722 (2012).

(35) T. Morimoto, T. Miyamoto, H. Okamoto, Crystals **7**, 132 (2017).

(36) L. M. Kiefer, K. J. Kubarych, Chem. Sci. **9**, 1527 (2018).

(37) R. Appleby, J. M. Chamberlain, Physics and Applications of Terahertz Radiation, Chapter 9. 173, 0342 (2014).

(38) R. Ulbricht, E. Hendry, J. Shan, T. F. Heinz, M. Bonn, Rev. M. Phys. **83**, 543 (2011).

(39) M. C. Beard, G. M. Turner, C. A. Schmuttenmaer, Phys. Rev. B. **62**, 15764 (2000).

(40) W. Zouaghi *et al.*, Eur. J. Phys. **34**, S179 (2013).

(41) D. D. Arnone, C. M. Ciesla, A. Corchia, S. Egusa, M. Pepper. Proc. 3828, 209 (**1999)**.

(42) R. M. Woodward, V. P. Wallace, D. D. Arnone, E. H. Linfield, M. Pepper, J. Bio. Phys. **29**, 257 (2003).

(43) http://photonicswiki.org/index.php?title=File:THz_OR.png#file

(44) H. Hamster, A. Sullivan, S. Gordon, W. White, R. W. Falcone, Phys. Rev. Lett. **71**, 2725 (1993).

(45) H. Hamster, A. Sullivan, S. Gordon, R. W. Falcone, Phys. Rev. E. **49**, 671 (1994).

(46) D. J. Cook, R. M. Hochstrasser, Opt. Lett. **25**, 1210 (2000).

(47) M. D. Thomson, M. Kreb. T. loffler, H. G. Roskos, Laser & Photon. Rev. **1**. 349 (2007).

(48) D. T. Emerson, IEEE Trans. Microwave Theory Tech. **45**, 2267 (1997).

(49) K.H. Yang, P.L. Richards, T.R. Shen, Appl. Phys. Lett. **19**, 320 (1971).

(50) D.H. Auston, Appl. Phys. Lett. **26**, 101 (1975).

(51) N. Nagai, R. Kumazawa, R. Fukasawa, Chem. Phys. Lett. **413**, 495 (2005).

(52) M. Takahashi, Crystal **4**, 74 (2014).

(53) J. Fahrenfort, J. Spectrochim. Acta. **17**, 698 (1962).

(54) N. J. Hanrick, Internal Reflection Spectroscopy, John Wiley & Sons Inc, New York (1967).

(55) H. Hiroki, K. Yamashita, M. Nagai, K. Tanaka, Jpn. J. Appl. Phys. **43**, L1287 (2004).

(56) R. Schiwon, G. Schwaab, E. Brundermanm, M. Havenith, Appl. Phys. Lett. **86**, 201116 (2005).

(57) H. Hiroki, M. Nagai, K. Tanaka, Opt. Express. **13**, 10801 (2005).

(58) M. Nagai, H. Yada, T. Arikawa, K. Tanaka, Int. J. Infrared Millimeter Wave. **27**, 505 (2006).

(59) N. Nagai, R. Kumazawa, R. Fukasawa, Chem. Phys. Lett. **413**, 495 (2005).

(60) Joo-Hiuk Son, Terahertz Biomedical Science and Technology, CRC Press (2014).

(61) K. Müller-Dethlefs, P. Hobza, Chem. Rev. **100**, 143 (2000).

(62) M. Wrighton, D. L. Morse, J. Am. Chem. Soc. **96**, 4 (1974).

(63) A. M. Blanco-Rodriguez, M. Busby, C. Gradinaru, B. R. Crane, Di Bilio, Am. Chem. Soc. **128**, 4365 (2006).

(64) K. K.-W. Lo, Top. Organomet. Chem. **29**, 115 (2010).

(65) K. K.-W. Lo, K.-S. Sze, K. H.-K. Tsang, N. Zhu, Organometallics **26**, 3440 (2007).

(66) K. K.-W. Lo, M.-W. Louie, K. Y. Zhang, Coord. Chem. Rev. **254**, 2603 (2010).

(67) D. J. Stufkens, A. Jr. Vlcek, Coord. Chem. Rev. **177**, 127 (1998).

(68) A. Jr. Vlcek, Top. Organomet. Chem. **29**, 73 (2010).

(69) A. Kumar, S.-S. Sun, A. J. Lees, Top. Organomet. Chem. **29**, 1 (2010).

(70) A. F. A. Peacock, H. D. Batey, C. Raendler, A. C. Whitwood, R. N. Perutz, A.-K. A. Duhme-Klair, Chem., Int. Ed. **44**, 1712 (2005).

(71) J. D. Lewis, J. N. Moore, Dalton Trans. **9**, 1376 (2004).

(72) R. C. Evans, P. Douglas, C. J. Winscom, Coord. Chem. Rev. **250**, 2093 (2006).

(73) H. Yersin, Transition Metal and Rare Earth Compound, Springer. New York. **241**, pp 1-26 (2004).

(74) A. Kumar *et al.*, J. Ind. Eng. Chem. **56**, 2873 (2018).

(75) D. J. Stufkens, A. Jr. Vlček, Coord. Chem. Rev. **177**, 127 (1998).

(76) D. J. Stufkens, Comments Inorg. Chem. **359**, 13 (1992).

(77) D. J. Stufkens, Coord. Chem Rev. **104**, 39 (1990).

(78) A. J. Lees, Chem Rev. **87**, 711 (1987).

(79) K. J. Kalyanasundaram, J. Chem. Soc., Faraday Trans. 2: Mol. Chem. Phys. **82**, 2401 (1986).

(80) J. K. Hino, L. Della Ciana, W. J. Dressick, B. P. Sullivan, Inorg. Chem. **31**, 1072 (1992).

(81) A. Cannizzo, O. Bram, G. Zgrablic, A. Tortschanoff, O. A. Ajdaradeh, F. van Mourik, M. Chergui, Opt. Lett. **32**, 3555 (2007).

(82) R. Hage, R. Prins, J.G. Haasnoot, J. Reedijk, J.G. Vos, J. Chem. Soc., Dalton Trans. **0**, 1389 (1987).

(83) W.R. Browne, PhD. Thesis, Dublin City University (2001).

(84) R.P. Thummel, D. Williamson, C. Hery, Inorg. Chem. **32**, 158 (1993).

(85) D. J. Stufkens, A. Jr. Vlcek, Coord. Chem. Rev. **177**, 127 (1998).

(86) L. A. Worl, R. Duesing, P. Chen, C. L. Della, T. J. Meyer, J. Chem. Soc., Dalton Trans. **0**, 849 (1991).

(87) A. Cannizzo, A. M. Blanco-Rodriguez, A. Nahhas, J. Šebera, S. Zališ, A. Jr. Vlček, M. Chergui, J. Am. Chem. Soc. **130**, 8967 (2008).

(88) O. Ishitani, M. W. George, T. Ibusuki, F. P. A. Johnson, K. Koike, Inorg. Chem. **33**, 4712 (1994).

(89) J. Hawecker, J.-M. Lehn, R. Ziessel, Helv. Chim. Acta. **69**, 1990 (1986).

(90) B. P. Sullivan, C. M. Bolinger, D. Conrad, W. J. Vining, T. J. Meyer, J. Chem. Soc. Chem. Commun. **0**, 1414 (1985).

(91) C. Kutal, A. J. Corbin, G. Ferraudi, Organometallics **6**, 553 (1987).

(92) M. Milosevic, App. Spectrosc. Rev. **39**, 365 (2004).

(93) Y. Harabuchi *et al*, J. Chem. Theory Comput. **12**, 2335 (2016).

(94) D. J. Liard, M. Busby, P. Matousek, M. Towrie, A. Jr. Vlček, J. Phys. Chem. A. **108**, 2363 (2004).

(95) A. J. Vlcek, Coord. Chem. Rev. **230**, 225 (2002).

(96) A. Maria *et al*., J. Phys. Chem. A **112**, 3506 (2008).

(97) A. Rondi *et al.*, Acc. Chem. Res. **48**, 1432 (2015).

(98) H. Hori, F. P. A. Johnson, K. Koike, O. Ishitani, T. Ibusuki, J. Photochem. Photobiology A. Chem. **96**, 171 (1996).